Dynamic Contact Interactions of Rough Fractal Surfaces

Thesis submitted in partial fulfillment of
the requirements for the degree of
Master of Mechanical Engineering

By

TAMONASH JANA
Examination Roll No.: M4MEC1614
Registration No.: 129391 of 2014 - 2015

Under the guidance of

Prof. Prasanta Sahoo
and
Dr. Anirban Mitra

DEPARTMENT OF MECHANICAL ENGINEERING
FACULTY OF ENGINEERING & TECHNOLOGY
JADAVPUR UNIVERSITY
KOLKATA – 700032
MAY 2016

FACULTY OF ENGINEERING AND TECHNOLOGY

JADAVPUR UNIVERSITY

CERTIFICATE OF APPROVAL*

This foregoing thesis is hereby approved as a credible study of an engineering subject carried out and presented in a manner satisfactory to warrant its acceptance as a prerequisite to the degree for which it has been submitted. It is understood that by this approval the undersigned do not endorse or approve any statement made, opinion expressed or conclusion drawn therein but approve the thesis only for the purpose for which it has been submitted.

Committee
On Final Examination for
Evaluation of the Thesis

**Only in case the thesis is approved.*

FACULTY OF ENGINEERING AND TECHNOLOGY

JADAVPUR UNIVERSITY

We hereby recommend that the thesis presented under our supervision by Mr. Tamonash Jana entitled "Dynamic Contact Interactions of Rough Fractal Surfaces" be accepted in partial fulfillment of the requirements for the degree of Master of Mechanical Engineering.

Countersigned

Thesis Advisors

Head of the Department
Mechanical Engineering
Jadavpur University

Dean of Faculty of
Engineering and Technology
Jadavpur University

ACKNOWLEDGEMENT

At the very outset, I acknowledge, with sincere appreciation and gratitude, the generous and arduous guidance and inspiration provided to me by my honorable guides, Prof. Prasanta Sahoo and Dr. Anirban Mitra for the guidance, support, encouragement, freedom, technical inputs, forcing me to my limits, discussions, teaching the intricacies in research and a lot they provided during the course of this research and preparation of this manuscript.

I would also like to convey my thanks to the Head of the Department, all academic and technical staffs of Mechanical Engineering Department, Jadavpur University, especially faculty members and laboratory-in-charge of Machine Elements Laboratory who helped me to complete the thesis work.

I would like to express my heartfelt gratitude to Dr. Biplab Chatterjee who helped me a lot to understand contact analysis in ANSYS and gave his helping hand whenever I faced any problem regarding ANSYS in spite of his busy schedule.

I would also like to express my sincere gratitude to my seniors of Machine Elements Lab viz. Dr. Ajay K. Waghmare, Amit Banerjee, Abhijit Biswas, Arkadeb Mukhopaddhay, Brajesh Panigrahi, Dr. Bikash Panja, Hareram Lohar, Dr. Prasanna Gadhari, Priyambada Nayak, Sanjib Kundu, Santanu Duari, Smrutiranjan Pradhan, and Vijay Barethiye whose support, technical inputs and helping attitudes helped my way out to the timely completion of the thesis. Special mention to my classmates, Jayanta Sarkar and Sushanta Ghuku for stimulating discussions, support and fun which were always constructive and refreshing.

In this respect, I would also like to grab this opportunity to express my heart-felt gratitude to my friends and room-mates for their consistent support without which it could have been very difficult to carry out the project work and complete the thesis.

I dedicate this work to my parents whose endless love and blessings give me strength in every single moment of my life.

Date: *(Tamonash Jana)*

Contents

Page No.

Certificate of approval iii

Certificate of supervisor v

Acknowledgement vii

Contents ix

Nomenclatures xiii

List of Figures xv

List of Tables xxi

Abstract xxiii

Chapter 1. Introduction **1-14**

- 1.1. Introduction to Contact of Rough Surfaces 3
- 1.2. Literature Review 4
  - 1.2.1. Literatures on Contact Analysis 4
  - 1.2.2. Literatures on Fractal Contact Analysis 9
  - 1.2.3. Literatures on Contact Vibration 12
- 1.3. Summary 13
- 1.4. Present Work 14
- 1.5. Present Thesis 14

Chapter 2. Finite Element Modelling and Analysis 15-35

2.1. Introduction 17

2.2. Fractal Surface Characterization 18

2.3. Fractal Surface Generation 19

2.4. Finite Element Modelling 22

    2.4.1. Generation of Rough Surface in ANSYS 22

    2.4.2. Modelling and Meshing 24

        2.4.2.1. SOLID187 24

        2.4.2.2. SOLID185 25

        2.4.2.3. CONTA174 25

        2.4.2.4. TARGE170 26

2.5. Finite Element Analysis and Solution 28

    2.5.1. Solution procedure in Finite Element Analysis 28

    2.5.2. Validation Study 29

    2.5.3. Results of Finite Element Analysis 31

2.6. Summary 35

Chapter 3. Dynamic Analysis of Rough Fractal Surface: Model I 37-60

3.1. Introduction 39

3.2. Dynamic Model 39

3.3. Numerical Solution methods 42

3.3.1. Runge-Kutta Method 42

3.3.2. Adaptive Simpson's Method 44

3.4. Undamped Free Vibration 46

3.5. Forced Damped Vibration 51

3.5.1. Superharmonic Response 57

3.5.2. Phase and Time-Displacement Plot Analysis 58

3.6. Summary 60

Chapter 4. Dynamic Analysis of Rough Fractal Surface: Model II 61-76

4.1. Introduction 63

4.2. Dynamic Model 64

4.3. Dynamic Analysis and Results 66

4.3.1. Superharmonic Response 69

4.3.2. Phase and Time-Displacement Plot Analysis 72

4.4. Summary 76

Chapter 5. Conclusions 77-80

5.1. Conclusions 79

5.2 Future scope of work 80

References 81-88

Nomenclatures

A_0	nominal contact area
c	damping coefficient
D	fractal dimension
E	elastic modulus of deformable surface
E'	composite elastic modulus of equivalent rough surface
F	amplitude of harmonic excitation force
F_s	restoring force of spring
f	frequency index
$f_{\max}$	maximum frequency index
G	fractal roughness
g	gravitational acceleration
k	nonlinear stiffness of spring/deformable surface
L	sample length of fractal surface
L_s	cut off length of fractal surface
M	number of superimposed ridges to construct the fractal surface
m	mass of the block
n	nonlinearity exponent. Exponent value in the power law force-displacement relationship equation $P^* = k\left(\delta^*\right)^n$
P	applied normal load on rough surface
P^*	normalized applied normal load, $P^* = \dfrac{P}{A_0 E'}$

t	time
u	normalized vertical displacement
$u(\max)$	maximum normalized vertical displacement (above which contact loss occurs)
y	vertical displacement of the base, the spring-mass-damper is resting on
Y	base excitation amplitude
Z	normalized base excitation amplitude $(Z = Y/z_s)$
z	vertical displacement of block
z_s	static vertical displacement of block due to its own weight
γ	frequency density
δ	displacement of contacting rough surface
δ^*	normalized displacement of contacting rough surface, $\delta^* = \delta / L$
ϕ	random phase angle of Weierstrass-Mandelbrot function
ν	Poisson's ratio
ζ	damping ratio
τ	normalized time, $\tau = t\omega_s$
ω	harmonic excitation frequency
ω_s	natural frequency of system at the static equilibrium position
ω_n	natural frequency in the non-dimensional equation of motion
Ω	normalized harmonic excitation frequency

List of Figures

Page No.

1. **Figure 1.1.** Rough surface contact in magnified view. 3

2. **Figure 2.1.** Self-affine property of a rough surface profile. 17

3. **Figure 2.2.** MATLAB generated fractal surface with D = 2.3, G = 1.36×10^{-11} m in 50×50 grid. 20

4. **Figure 2.3.** MATLAB generated fractal surface with D = 2.4, G = 1.36×10^{-11} m in 50×50 grid. 20

5. **Figure 2.4.** MATLAB generated fractal surface with D = 2.5, G = 1.36×10^{-11} m in 50×50 grid. 20

6. **Figure 2.5.** MATLAB generated fractal surface with D = 2.4, G = 1.36×10^{-10} m in 50×50 grid. 21

7. **Figure 2.6.** MATLAB generated fractal surface with D = 2.4, G = 1.36×10^{-12} m in 50×50 grid. 21

8. **Figure 2.7.** Fractal surface with D = 2.3, G = 1.36×10^{-10} m modelled in ANSYS. 23

9. **Figure 2.8.** Fractal surface with D = 2.3, G = 1.36×10^{-11} m modelled in ANSYS. 23

10. **Figure 2.9.** Fractal surface with D = 2.4, G = 1.36×10^{-11} m modelled in ANSYS. 23

11. **Figure 2.10.** Geometry of structural solid element SOLID187. 24

12. **Figure 2.11.** Geometry of structural solid element SOLID185 25

13. **Figure 2.12.** Geometry of CONTA174 and interaction with target surface. 26

14. **Figure 2.13.** Geometry of TARGE170 and interaction with contact element. 26

15. **Figure 2.14.** Fractal surface with $D = 2.3$, $G = 1.36\times10^{-10}$ m after meshing. 27

16. **Figure 2.15.** Fractal surface with $D = 2.3$, $G = 1.36\times10^{-11}$ m after meshing. 27

17. **Figure 2.16.** Meshed model of rough surface in contact with rigid flat surface. (The point with * sign indicates the pilot node). 28

18. **Figure 2.17.** Comparison with the results of Chatterjee and Sahoo and Buzio et al. 30

19. **Figure 2.18.** Plots of non-dimensional force versus non-dimensional displacement of rough surfaces for varying fractal dimension (D). 31

20. **Figure 2.19.** Plots of non-dimensional force versus non-dimensional displacement of rough surfaces for varying fractal roughness parameter (G). 32

21. **Figure 2.20.** Plots of non-dimensional force versus non-dimensional displacement of rough surface for varying tangent modulus (E_t)□ 33

22. **Figure 2.21.** Plots of non-dimensional force versus non-dimensional displacement of rough surface for varying yield strength(Y). 34

23. **Figure 3.1.** Model of the deformable surface coming in contact with rigid flat surface. 39

24. **Figure 3.2.** SDOF model representation of the dynamic contact model. 40

25. **Figure 3.3.** Initial solution point, trial midpoints, trial endpoint and final endpoint for fourth order Runge-Kutta method. 43

26. **Figure 3.4.** Plots of non-dimensional natural frequency vs. non-dimensional initial displacement of rough surfaces for varying fractal dimension (*D*). 48

27. **Figure 3.5.** Plots of non-dimensional natural frequency vs. non-dimensional initial displacement of rough surfaces for varying fractal roughness (*G*). 48

28. **Figure 3.6.** Plots of non-dimensional natural frequency vs. non-dimensional initial displacement of rough surfaces for varying tangent modulus (*Et*). 49

29. **Figure 3.7.** Plots of non-dimensional natural frequency vs. non-dimensional initial displacement of rough surfaces for varying yield strength (*Y*). 49

30. **Figure 3.8.** Non-dimensional natural frequency vs. non-dimensional initial displacement plot for linearly behaving contact system. 50

31. **Figure 3.9.** Frequency response curve for rough fractal surface with D=2.3, G=1.36×10^{-11} m. 51

32. **Figure 3.10.** Frequency response curve for rough fractal surface with D=2.4, G=1.36×10^{-11} m. 52

33. **Figure 3.11.** Frequency response curve for rough fractal surface with D=2.5, G=1.36×10^{-11} m. 52

34. **Figure 3.12.** Frequency response curve for rough fractal surface with D=2.6, G=1.36×10^{-11} m. 52

35. **Figure 3.13.** Frequency response curve for rough fractal surface with D=2.4, G=1.36×10^{-13} m. 53

36. **Figure 3.14.** Frequency response curve for rough fractal surface with D=2.4, G=1.36×10^{-12} m. 53

37. **Figure 3.15.** Frequency response curve for rough fractal surface with D=2.4, G=1.36×10^{-10} m. 53

38. **Figure 3.16.** Frequency response curve for rough surface material with yield stress 250 MPa and tangent modulus 10 GPa. 54

39. **Figure 3.17.** Frequency response curve for rough surface material with yield stress 250 MPa and tangent modulus 60 GPa. 55

40. **Figure 3.18.** Frequency response curve for rough surface material with yield stress 250 MPa and tangent modulus 100 GPa. 55

41. **Figure 3.19.** Frequency response curve for rough surface material with tangent modulus 10 GPa and yield stress 560.8 MPa. 56

42. **Figure 3.20.** Frequency response curve for rough surface material with tangent modulus 10 GPa and yield stress 911.5 MPa. 56

43. **Figure 3.21.** Frequency response curve for rough surface material with tangent modulus 10 GPa and yield stress 1265.3 MPa. 56

44. **Figure 3.22.** Frequency response curve for rough surface material with tangent modulus 10 GPa and yield stress 1619 MPa. 57

45. **Figure 3.23.** Superharmonic response for the system corresponding to n = 2.0. 58

46. **Figure 3.24.** (a) Phase plot and (b) time-displacement plot of vibrating rough surface with n = 0.6 for normalized initial displacement as 0.5. 58

47. **Figure 3.25.** (a) Phase plot and (b) time-displacement plot of vibrating rough surface with n = 1.0 for normalized initial displacement as 0.5. 59

48. **Figure 3.26.** (a) Phase plot and (b) time-displacement plot of vibrating rough surface with n = 1.5 for normalized initial displacement as 0.5. 59

49. **Figure 3.27.** (a) Phase plot and (b) time-displacement plot of vibrating rough surface with n = 2.0 for normalized initial displacement as 0.5. 60

50. **Figure 4.1.** (a) Deformable rough surface in contact with rigid flat surface and (b) SDOF dynamic model representation. 63

51. **Figure 4.2.** Comparison between frequency response curves for surfaces having D values 2.4, 2.5 and 2.6 for $Z = 0.0198$. 66

52. **Figure 4.3.** Comparison between frequency response curves for surfaces having D values 2.4 and 2.3 for $Z = 0.036$. 67

53. **Figure 4.4.** Comparison between frequency response curves for surfaces having G values varying from 1.36×10^{-11} m to 1.36×10^{-13} m for $Z = 0.0192$. 67

54. **Figure 4.5.** Frequency response curves for rough surface material with yield stress 250 MPa and varying tangent modulus 10, 60 and 100 GPa for $Z = 0.02$. 68

55. **Figure 4.6.** Frequency response curves for rough surface material with tangent modulus 10 GPa and varying yield strength 560.8 MPa, 911.5 MPa, 1265.3 MPa and 1619 MPa for Z=0.000295. 68

56. **Figure 4.7.** Comparison of frequency response curves with n values 0.98 and 1.02 for $Z = 0.028$. 69

57. **Figure 4.8.** Superharmonic response for nonlinearity exponent value 1.2. 70

58. **Figure 4.9.** Superharmonic response for nonlinearity exponent value 1.4. 70

59. **Figure 4.10.** Superharmonic response for nonlinearity exponent value 1.6. 71

60. **Figure 4.11.** Superharmonic response for nonlinearity exponent value 1.8. 71

61. **Figure 4.12.** Superharmonic response for nonlinearity exponent value 2.0. 71

62. **Figure 4.13.** Superharmonic response for nonlinearity exponent value 2.1. 72

63. **Figure 4.14.** Magnified view of the superharmonic responses for nonlinearity exponent (*n*) 1.6. 72

64. **Figure 4.15.** (a) Phase plot and (b) time-displacement plot of vibrating rough surface with *n* = 0.6 for normalized initial displacement as 0.5. 73

65. **Figure 4.16.** (a) Phase plot and (b) time-displacement plot of vibrating rough surface with *n* = 1.0 for normalized initial displacement as 0.5. 73

66. **Figure 4.17.** (a) Phase plot and (b) time-displacement plot of vibrating rough surface with *n* = 1.5 for normalized initial displacement as 0.5. 74

67. **Figure 4.18.** (a) Phase plot and (b) time-displacement plot of vibrating rough surface with *n* = 2.0 for normalized initial displacement as 0.5. 74

68. **Figure 4.19.** (a) Phase plot and (b) time-displacement plot of vibrating rough surface with *n* = 0.6 for normalized initial displacement as -0.5. 75

69. **Figure 4.20.** (a) Phase plot and (b) time-displacement plot of vibrating rough surface with *n* = 2.0 for normalized initial displacement as -0.5. 75

List of Tables

Page No.

1. **Table 2.1.** Values of nonlinear stiffness (k) and nonlinearity exponent (n) for different fractal dimension (D) and fractal roughness (G) values. 32
2. **Table 2.2.** Values of nonlinear stiffness (k) and nonlinearity exponent (n) for different tangent modulus (E_t) and yield strength (Y) values 34
3. **Table 3.1.**Values of maximum initial displacement before contact loss and corresponding nonlinearity exponent (n) for different combinations of fractal dimension (D) and fractal roughness (G) values. 47

Abstract

In the present thesis the dynamic characteristics of rough deformable fractal surface in contact with a rigid flat surface is analyzed. Coordinate points constructing fractal surface are generated using the modified Weierstrass-Mandelbrot function in MATLAB which are imported to commercial finite element software ANSYS 14.5 as keypoints to construct the finite element model of the rough surface. A rigid flat surface capable of vertical motion is considered to come in contact with and any downward motion of the rigid flat causes deformation of the rough surface. A finite element analysis is implemented using ANSYS to obtain the static force-displacement relationship at the contact between deformable rough surface and rigid flat. A power law curve is fitted through the obtained force-displacement result points and nonlinear contact bulk stiffness and a parameter called 'nonlinearity exponent' are found out which provides the measure of nonlinearity of the contact system. These parameters are subsequently used to find out the dynamic properties of the contacting interface for free-undamped as well as for forced-damped vibration. It has been observed that, the nonlinearity of the system increases with the increase of surface roughness, tangent modulus and with the decrease of yield strength. For the sake of dynamic analysis, the physical dynamic contact system is modelled by single degree of freedom spring-mass-damper system. The external excitation on the dynamic system is imparted in two ways in the two models presented in the thesis. For free undamped vibration analysis, contact loss is taken into account and the variation of normalized natural frequency w.r.t. initial displacement is presented for different surface and material properties. In case of forced damped vibration, it is found that the system exhibits softening property for linear elastic surface and the softening nature increases with rougher topography. The softening nature of the system increases with increase in tangent modulus value. Above a certain value of yield strength the nature of the frequency response curve is observed to change its nature from softening to hardening. Superharmonic response is also observed for the vibrating contact system. In the second model, the contact system is represented by a spring-mass-damper system with base excitation. It is found that, for higher surface roughness, tangent modulus and lower yield strength value, the response amplitude decreases. For higher nonlinearity the response amplitude decreases but above certain value of nonlinearity exponent the peak amplitude becomes fixed. For both the models, in frequency response curves multiple solution zones jump up and jump down are observed. From phase plot and time-

displacement plot it is noted that higher nonlinearity causes higher asymmetricity of the phase plot w.r.t. the vertical axis.

Chapter 1

Introduction

The chapter provides a general introduction to the entire work. It gives a brief idea of contact vibration in the context of the present work, literature review on the domain of the present work and the objective of the work.

1.1. Introduction to Contact of Rough Surfaces

Contact interaction of solid surfaces plays an important role in the working of machine elements like gear, cam-follower mechanism and rolling element bearing etc. as it has huge influence on friction, adhesion, wear and lubrication. Interactions between solid surfaces are dependent on the contacting materials and the shape of the surfaces. The shape of the surface of an engineering material is dependent upon its production process and the nature of the parent material. It is well known that all the engineering surfaces are inherently associated with roughness. Practically it is not possible to get ideally smooth surfaces. Hence, when any surface to surface contact occurs it is never a flat to flat surface contact, but it is rather asperity to asperity contact and the real area of contact is only a fraction of the apparent area of contact. In such conditions the pressure at the picks is extremely high and it undergoes high rate of deformation.

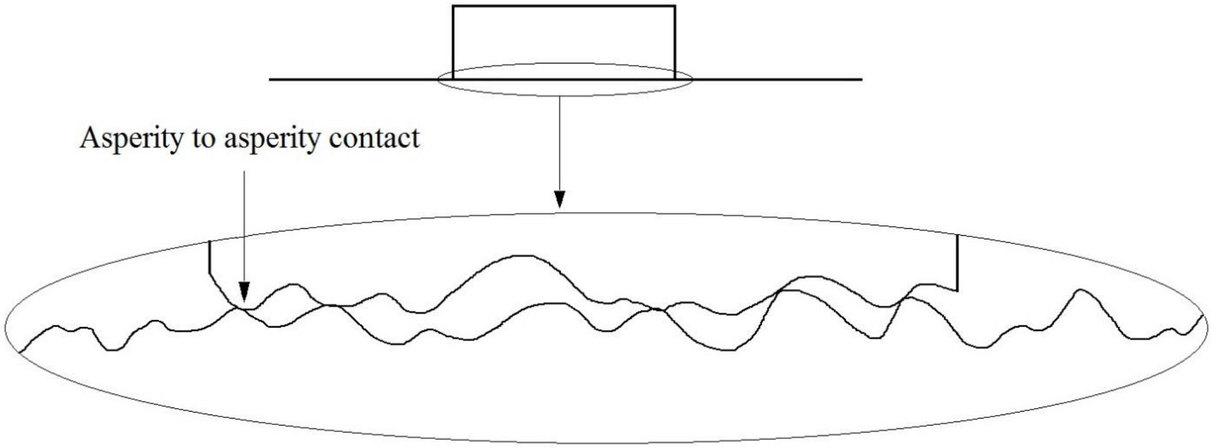

Figure 1.1. Rough surface contact in magnified view.

Besides on the static properties, the surface parameters have also significant impact on the dynamic properties of the interacting surfaces. The vibration of the contacting surface is mainly caused by external excitation, rolling or sliding of surfaces, surface roughness/waviness or combinations of all of these. It is obvious that vibration (or dynamics) at the contacting rough surface has major influence of the fatigue and wear performance of the components, which is associated with the damaging of the machine element. Static and dynamic properties of contacting solid surfaces are the topics of huge importance because of their presence in large number of engineering applications. Also these topics are closely interconnected with each other. The damaging effects on the machines are associated with production as well as economic loss of the corresponding industry. So designing the systems with the considerations for controlling these phenomenon will not only result in improvement in efficiency or performance but will also help to reduce economic losses. Hence the study of contact interactions of rough surfaces has always been an area of research interest.

1.2. Literature Review

It is necessary to present a brief discussion of the evolution of contact analysis in order to set a scene for the present analysis. Related literatures available on static and dynamic analysis of single asperity contact and rough surface contact are recapitulated here.

Starting from early years to current time different researchers have carried out many theoretical and experimental studies to investigate contact properties of surfaces. Initially the contact problems were analyzed by extremely simplified models which were very much different from real contact conditions. Later evolution of elastic to plastic contact with increase of load, and its effect on contact parameters was taken into consideration. Hence contact analysis at high load became realistic than before. Effect of variation of the material properties were also analyzed. Later Fractal analysis pioneered by Mandelbrot was applied to model rough surfaces and analyze their contact properties. Primarily detailed stress analysis was not possible due to the lack of proper tool to model significant geometric and material non-linearity encountered in elastic-plastic and plastic regimes. After the introduction of Finite Element Analysis it emerged as a logical solution of these shortcomings since it is robust enough to simulate almost every feature of contact problems encountered. Besides the static analysis, dynamic contact analysis has become an important area in recent days.

1.2.1. Literatures on Contact Analysis

The first significant single asperity contact model was provided by Hertz [1, 2]. Hertz also attempted to give a precise definition of hardness of solids. This attempt has proved to be unsatisfactory due to the difficulty of detecting the point of first yield under the action of contact stress. Hertz found the contact area of the quadratic surfaces to be elliptical due to elastic deformation. Abbot and Firestone [3] built a surface roughness-measuring device consisting of a stylus and introduced the most widely used model for a fully plastic contact. It was considered that if the contact stress in a solid crosses the hardness of the material it undergoes plastic deformation. In fact, this plastic truncation model given by Abbot and Firestone is more useful to describe a wear process rather than a deformation process. Greenwood and Williamson [4] presented one of the most basic and widely accepted model for elastic contact. It was shown how the number of contacting asperity, real contacting are and contact deformation depends on the topography of the surface. A new criterion called ‘plasticity index’ was provided which indicates whether contact will be elastic or plastic. But Greenwood Williamson model is considered to be over-simplified due to its assumptions. Greenwood and Tripp [5] gave a general theory of contact between two rough plane surfaces. It was showed that the load and the area of contact remain almost proportional, independently of the detailed mechanical and geometrical properties of the asperities and a single-rough-surface model can always be found which would predict the same laws as a given two-rough-surface model. Akyuz and Merwin [6] first studied the two-dimensional stresses beneath a cylindrical indenter using finite element method. Whitehouse and Archard [7] considered the random surface profile as an equivalent random signal characterized by height distribution and an auto correlation function taking care of the distribution for both asperity height and radii. Hardy et al. [8], Dumas and Baronet [9], and Lee et al. [10] provided more complete computations for the indentation of an elastic perfectly plastic half-space by a cylinder and sphere. Nayak [11] adopted a sophisticated statistical model which characterizes a random rough surface by three spectral moments of the profile which are equivalent to the variance of the distribution of profile heights, slopes and curvatures. Tallian [12] analyzed strongly anisotropic surfaces in which the surface is modelled as random process with surface heights in Gaussian distribution and found out that besides the surface roughness, the surface frequency plays an important role to determine the contact behaviour. Gupta and Cook [13] studied rough surface contact model having tip heights in Gaussian distribution and asperity radii in log-normal distribution. Williamson and Hunt [14] studied the plastic indentation experimentally and concluded that asperity persistence does not depend on the particular metal in contact and for local indentations, the degree of contact (the ratio of real to nominal area) is independent of the load. Onions and Archard [15] studied a model with a Gaussian distribution of both surface heights (instead of asperity heights) and asperity curvatures. Hisakado [16] pointed out that a Gaussian distribution of asperity heights and curvatures for a given asperity shape may lead to a non-Gaussian distribution of the surface height, which is unrealistic for most engineering surfaces. Bush et al. [17] followed the Nayak [11] microgeometry assumptions and modelled the asperities as paraboloids with two different radii of curvature as maximum and minimum curvature of the asperity and found that in the limiting case of large separations, the area of true contact is proportional to the applied load, and equal to just half of the bearing area. O'Callaghan and Cameron [18] and Francis [19] extended the Bush et al. [17] model for the case in which both surfaces are rough and surfaces need not contact and concluded that this type of contact is negligibly different from the GW model. McCool [20] investigated the limit of applicability of elastic contact models of rough surfaces, using a plane strain solution for a sinusoidally corrugated half-space. McCool [21] also considered a general anisotropic model and the results were found to be in very good agreement with those of the simpler GW model. Greenwood [22] approximated the contact pressure and approach with an equivalent radius of curvature using the circular contact formula. Johnson [23] showed that the pressure distribution for the solids of revolution rises to infinity without interfering outside contact area and adhesion. Excluding the term responsible for infinite pressure distribution, Boussinesq [24] appreciated that the pressure distribution between two elastic bodies, whose profiles are continuous through the boundary of the contact area, falls continuously to zero at the boundary. Chang, Etsion and Bogy [25] presented an elastic-plastic asperity model for analyzing the contact of rough surfaces based on volume conservation of an asperity control volume during plastic deformation showed the relationship between mean effective pressure and hardness in terms of Poisson's ratio. But this CEB model suffers from a discontinuity in the contact load as well as in the first derivative of both the contact load and the contact area at the transition from elastic to elastic-plastic region. Kucharski et al. [26] presented a finite elements analysis of contact between an elastoplastic sphere and a rigid plane. The relations obtained i.e. load-approach, and load-contact area, were combined with statistical description of the rough surface for modelling contact between the two surfaces and the results of numerical investigations were in good agreement with experimental results. Ju and Farris [27] applied spectral analysis methods and the Fast Fourier Transform (FFT) to characterize a surface in two-dimensional contact problems. Zhao, Maietta and Chang [28] presented a model for transition from elastic deformation to fully plastic flow of the contacting elastic-plastic asperities and the relation for the ratio of the elastoplastic contact area versus load was derived. It was shown that the elastoplastic contact of asperities plays an important part in the macrocontact behaviour of rough surfaces. Adams and Nosonovsky [29] reviewed single and multi-asperity contact models with an emphasis on the forces of contact and their relationship to the geometrical, material and mechanical properties of the contacting bodies. Zhao and Chang [30] showed that the contact interactions increase the mean separation of surfaces and reduce the real area of contact and on the asperity level it cause redistributions of the contact load among asperities of different heights. As a result, the load carried by asperities of larger heights would increase. And for plastic asperity contact the effect is opposite. Kogut and Etsion [31] first ever effectively utilized commercial finite element software ANSYS for the accurate calculation of contact parameters in elastic-plastic as well as plastic contact analysis of a deformable sphere against a rigid flat and found that the evolution of the elastic-plastic contact can be divided into three distinct stages – elastic, elastic-plastic and fully plastic for different ω/ω_c values. Again Kogut and Etsion [32] presented an improved elastic plastic model for the contact of rough surfaces based on an accurate Finite Element Analysis solution of a single asperity contact which predicted separation, real area of contact and real contact pressure as functions of the plasticity index and contact load. The contact stiffness was shown to be insensitive to the plasticity index and contact load for low value and sensitive at high value of critical load ratio. Jackson and Green [33] presented a 2D axisymmetric finite element model of an elastic-perfectly plastic hemisphere in contact with a rigid flat surface derived from the Hertzian solution and the von Mises yield criterion which discovered significant geometrical and material nonlinearities. It was found that the hardness depends upon the modulus of elasticity, Poisson's ratio, and the deformation itself.

Bahrami, Yovanovich and Culham [34] developed a new model that considered the effect of roughness on the elastic contact of spherical bodies in which the deformations of surface asperities were considered to be plastic and the bulk deformation was assumed to be within the elastic limit. A new parameter, non-dimensional maximum contact pressure, was introduced which was shown to be the key parameter that controls the contact. Cai and Bhushan [35] developed a numerical 3D model for the analysis of rough, two-layered elastic and elastic-perfectly plastic surfaces which was based on a variational principle. It was found that compliant top layers can minimize the maximum contact pressure, the surface and subsurface stresses and increase the real area of contact. And stiff top layer does the opposite. Jackson and Streator [36] described a non-statistical iterative multi-scale model of the normal contact between rough surfaces. It was found that only the lower roughness frequencies impact the real area of contact and the real area of contact is proportional to the load for both elastic and elasto-plastic contact. Jamari and Schipper [37] carried out experimental investigation of the contact between a deformable sphere and a rigid flat to explore its behavior in the fully plastic contact regime. It was found that the mean contact pressure was constant and the contact area is simply the truncation of the sphere by the hard flat for a fully plastic contact regime. Kadin et al. [38] developed and analyzed a statistical model for the unloading of elastic–plastic contact of rough surfaces for a single load–unload cycle in which the hystereses of load-separation and load real contact area behavior were analyzed for a range of surface roughness and loading conditions. . It was shown that the main parameters affecting the unloading are the original plasticity index and the maximum contact loading from which the unloading begins. Greenwood [39] presented a modified version of the Greenwood and Williamson is which closely follows the predictions of BGT model [17] in which unlike the GW model, curvature of the spheres do not have a constant height-independent curvature, but depends on the asperity height through a relation which depends on the surface statistics. It was found that the linear asymptotic relation between contact area and load is only a consequence of the change in asperity curvature with asperity height and not of treating asperity as randomly distributed paraboloids. Shankar & Mayuram [40] modelled an axisymmetric hemispherical asperity in contact with a rigid flat for an elastic perfectly plastic material in which they showed the critical values in the dimensionless interference ratios for the evolution of the elastic core and the plastic region within the asperity for different Yield Strength/Elastic Modulus ratios of the material. Ciavarella et al. [41] also formulated an improved version of the Greenwood and Williamson (GW) theory with the inclusion of interaction between asperities which was achieved by treating the contact pressures as uniformly distributed over the apparent contact area and the resulting deformation as uniform. Numerical contact simulations using Weierstrass–Mandelbrot surfaces were shown to agree with this improved theory.

Sepehri and Farhang [42] presented a three dimensional contact model of two rough surfaces in elastic-plastic contact considering asperity shoulder-shoulder contact, in which the volume conservation was assumed in the plastic flow regime. Sahoo et al. [43] showed that a generalized solution cannot be applicable for all kind of materials as the effect of strain hardening greatly influences the contact parameters especially in the high or fully plastic regime which increases with the increase in the value of hardening parameter. The increase in strain hardening makes the surface capable of carrying higher amount of load in a smaller contact area. Sahoo and Chatterjee [44] analyzed 2D axisymmetric finite element model of an elastic perfectly plastic hemisphere in contact with a rigid flat and found out that the maximum mean contact pressure ratio and the corresponding dimensionless interference are dependent on the E/Y ratio and the dimensionless contact load, contact area and mean contact pressure are independent of the radius of sphere. Brake [45] developed a new elastic–plastic contact model based on material properties and contact geometries for studying impact between two round surfaces which was divided into three phases for loading: an elastic regime with solution provided by Hertz, a mixed elastic–plastic regime with solution based on continuity, and a fully plastic regime that had a linear force–deflection constitutive relationship. Gandhi et al. [46] studied the effect of tangent modulus and strain hardness on the contact behaviour of a frictionless elastic-plastic contact for different materials by FE analysis and analytical method. It was found that when the tangent modulus is increased, the hardness increases and the projected area of the indentation is reduced, as a result straining action of the material increases and material can carry large load in smaller contact area. Peng et al. [47] studied a finite element model and showed that the yield stress to elasticity modulus ratio affects the contact behaviour in the early stage of contact but at high interference the boundary condition of hemisphere base has much influence on the contact behaviour. Peng et al. [48] found that for the rough surface contact under a given separation, the increase of surface topography plasticity index and material plasticity index was found to result in larger contact area and contact load. Wang and Xiang [49] analyzed the tangential contact characteristics of a single hemispherical asperity when the asperity deformed in the stages of normal elastic-plastic deformation by finite element method. Megalingam and Mayuram [50] generated Gaussian rough surfaces using FFT technique and carried out three-dimensional contact analyses using finite element method. It was found that for the surface having low surface roughness, the asperities deform mostly elastically whereas for medium and high surface roughness, the elasto-plastic and plastic deformation are significant.

1.2.2. Literatures on Fractal Contact Analysis

The concept of fractal geometry was first pioneered by Mandelbrot. Mandelbrot [51, 52, 53, 54] described the inherent symmetricity and self-similarity out of the chaotic phenomena of nature by fractal geometry like shape of cloud, hill, coastline etc. and explained its property of self-similarity and self-affinity. Mandelbrot introduced mathematical representation using fractal dimension and proposed extension of the Weierstrass function to express fractal mathematically. Berry and Lewis [55] and Ausloos and Berman [56] modified the Weierstrass –Mandelbrot equation later. Ling [57] presented the applicability of fractal geometry as a model of rough surface and analyzed the mathematical representation. Majumdar, Tien [58] used the W-M fractal function to obtain scale-independent fractal parameters to characterize rough surfaces and The power spectra of the stainless steel surface profiles was observed to coincide at high frequencies and at small length scales. Majumdar and Bhushan [59] used fractal geometry to characterize the multiscale self-affine topography by fractal dimension and the fractal representation of surfaces showed that the size-distribution of the multiscale contact spots follows a power law and is characterized by the fractal dimension (D) of the surface. Majumdar and Bhushan [60] predicted that all contact spots of area smaller than a critical area are in plastic contact and when the load is increased, these plastically deformed spots join to form elastic spots. Blackmore and Zhou [61] obtained a general distribution function for the heights of anisotropic engineering surfaces by extending earlier work on surface profiles. Yan and Komvopoulos [62] incorporated the modified W-M function generated fractal rough surface model into an elastic-plastic contact mechanics analysis of two approaching rough surfaces which yielded relationships for the contact force and real contact area and the condition of evolution of elastic and plastic deformation at the contact interface in terms of separation distance, fractal parameters, and material properties.

Zahouani et al. [63] used the fractal theory as a mathematical model for random surface topography, to be used as input data in contact modeling and analyzed through experiments, the contact between fractal random surfaces and a smooth plane. Komvopoulos and Ye [64] applied finite element model of a rigid sphere in normal contact with a semi-infinite elastic-plastic homogeneous 3D rough surface generated by the two-variable W-M function with fractal parameters determined from real surface images to obtain a constitutive relation between the mean contact pressure, real contact area, and corresponding representative strain. Palasantzas and Hosson [65] have calculated the real contact area between elastic bodies with self-affine rough surfaces, which were described in terms of analytical correlation models in Fourier space. Willner [66] investigated elasto-plastic normal contact of fractal surfaces by numerically generating the surfaces using a special form of the structure function and studied the influence of different surface parameters with respect to the load-area relationship and the load-gap relationship. Chung and Lin [67] derived two roughness parameters analytically as a function of the mean separation and derived the relationship among fractal dimension (D), fractal roughness parameter (G), and scaling coefficient from the equivalence of two structure function expressions. Kogut and Jackson [68] conducted a comparison between contact mechanics results obtained with statistical and fractal approaches to characterize surface topography and found that contact area versus contact load and separation versus contact load, predicted by the GW statistical model are largely dependent on the sampling resolution used to characterize the surfaces. Liou and Lin [69] showed that two invariants in the fractal analysis of surface asperities, fractal dimension and the topothesy can be varied by changing the mean separation of two contact surfaces. Sahoo and Ghosh [70] studied finite element analysis of non-adhesive elastic/elastic–plastic contact between a rigid flat and a self-affine fractal rough surface and showed that in the elastic regime, contact area is linearly proportional to the contact load at small loads, for small D values and at large G values. But at higher loads, for high D values and low G values the load area behaviour becomes nonlinear.

Jiang et al. [71] developed a general model based on fractal geometry to analyze the contact stiffness of the plane joint rough surfaces which shows that for a fixed load, decreasing the surface roughness increases the real contact area, and decreases the critical contact area, so those microcontacts yield elastic deformation, which increases the normal and tangential contact stiffness. Pohrt and Popov [72, 73] applied reduction method to solve the elastic contact problem of fractal rough surfaces having different fractal dimensions and also calculated the normal interfacial stiffness and constriction resistance of two elastic bodies with randomly rough surfaces and varying fractal dimensions using the boundary element method. Pohrt et al. [74] compared exact calculations of contact stiffness between elastic bodies with fractal rough surfaces (carried out by means of the boundary element method) with results of the corresponding one-dimensional model. Sahoo and Chatterjee [75] studied the effect of material properties such as yield strength and modulus of elasticity on contact area, normal displacement and mean contact pressure in both perfect slip and full stick contact of fractal surfaces utilizing ANSYS and found that that with the varying elastic properties of the material but with same E/Y ratio, loading in fractal surfaces yields identical contact parameters. Miao and Huang [76] studied the total load, area and stiffness of a fractal rough surface and found that the contact area is dependent linearly on the contact load and the share of plastic contact area decreases as the contact load increases. Sahoo and Chatterjee [77] presented a finite element simulation which described the influence of varying elastic modulus in a non-adhesive frictionless bulk deformation contact between isotropic self-affine fractal surface and a rigid flat covering elastic, elastic-plastic and the plastic region. Buczkowski et al. [78] used the fractal theory based on a single variable Weierstrass–Mandelbrot function to obtain the normal contact stiffness if rough and smooth isotropic surfaces pressed against each other taking the actual deformation of asperities and a correction due to asperity interaction into account.

1.2.3. Literatures on Contact Vibration

Nayak [79] presented the first significant work on contact vibration. He developed some of the theoretical groundwork necessary for detailed physical explanations of experimentally observed phenomena in vibratory point contact for three cases: undamped free vibrations, forced damped vibrations with a sinusoidal input, and vibrations with a broadband random input. Three problems of interest in rolling and/or sliding contact were considered in detail: loss of contact, plastic deformation, and the formation of corrugations. Hess and Soom [80, 81] studied nonlinear vibrations at a Hertzian contact excited by the dynamic component of an externally applied normal load by method of multiple scales [82] and solutions were obtained for both the average and instantaneous contact deflections. The average normal contact deflection during oscillations is found to be smaller than the static deflection under the same average load which can result in a reduction of the average area of contact. They also performed the same analysis for the contact region formed between rough surfaces and it was found that the contact region behaves as a nonlinear spring in parallel with a viscous damper, supporting a rigid mass. Perret-Liaudet [83,84] investigated a sphere-plane (Hertzian) contact problem for sub-harmonic and super-harmonic resonance of order two using MMS expanding the nonlinearity by third order Taylor series. The condition for contact loss was taken into consideration for the first time in this work. Sabot et al. [85] studied the non-linear vibrations of a sphere–plane contact excited by a normal load equal to the sum of a static load and a harmonic load and predicted the contact natural frequency, frequency contents and softening behavior using numerical and analytical methods. Perret-Liaudet and Sabot [86] studied a single-degree-of-freedom non-linear oscillator induced by an external harmonic normal force on a loaded sphere-plane Hertzian contact and also investigated non-linear resonances which lead to vibro-impact responses. Rigaud and Perret-Liaudet [87, 88] investigated experimental dynamic behaviour of a preloaded double sphere–plane Hertzian contact under sinusoidal excitation for several input levels including vibro-impact responses. In the second part the previous analysis was extended to the case of vibroimpact response of a preloaded and non-sliding dry Hertzian contact under Gaussian white random normal excitation. They also analyzed the dynamic response of an impacting Hertzian contact subjected to an order-2 subharmonic excitation and an order-2 superharmonic excitation [89, 90]. Ma et al. [91] studied the same sphere-plane contact model with possible contact loss experimentally and analytically using a multi-term harmonic balancing method taking contact loss into consideration. Tian and Xie [92] investigated the dynamic contact stiffness at the interface between a vibrating rigid sphere and a semi-infinite transversely isotropic viscoelastic solid with an oscillating force superimposed onto a static compressive force in the vertical direction exciting the vibration of the sphere. Xiao et al. [93] used exact method, method of multiple scales and harmonic balance method to determine the natural frequency of a mass interacting with a nonlinear contact stiffness. The maximum initial displacement leading to loss of contact and the corresponding natural frequency for the system was determined to be only functions of the non-linearity coefficient. Zili, et al. [94] employed fractal contact model in conjunction with thin layer elements to capture the effects of lightly clamped joint interfaces on the dynamics of assembled structures taking the effects of surface topography, preload, and material properties into account. Xiao et al. [95] studied the force-deflection characteristic and the nonlinear vibration of a rough surface which was constructed using a modified two-variable Weierstrass-Mandelbrot fractal function interacting with a rigid flat surface. The natural frequency was determined both exactly and approximately from the numerical calculation of the natural period. It was found that the degree of nonlinearity and the variation of natural frequency with amplitude increase with a rougher surface topography, and the maximum positive initial displacement leading to contact loss decreases accordingly.

1.3. Summary

In the present section, a gist about the research works on static and dynamic analysis of contact of rough surfaces is provided to outline the scope of further studies. This offers justification for the choice of the problems to be taken up in the thesis work. There exists a number of studies on the single asperity contact analysis as well as multi asperity contact analysis. Analysis of various parameters influencing the contact parameters like contact load, real contact area, contact pressure etc. has also been done by many researchers so far. Literature is abundant with studies on modelling of rough surfaces to explain the contact behaviours of rough surfaces in elastic, elastic-plastic and fully plastic regime which has become much easier with the introduction of commercial finite element softwares. Substantial amount of research works has dealt with contact analysis of fractal surfaces. Numerous research work also exist on contact behaviour on repeated loading-unloading cycle.

When dynamic analysis of contacting surface is considered there are much less emphasis in this area in comparison with the static analysis. From the literature it can be seen that there exists a few single asperity and sphere plane dynamic analysis considering damped and undamped nonlinear vibration with sinusoidal or random. But research work in the area of dynamic analysis of multi-asperity rough surface is found to be very rare. Hence there is a large scope of research work in the area of dynamic analysis of contacting rough surfaces for single and/or multi asperity level.

1.4. Present Work

In the present work, the dynamic properties of deformable rough surface is analyzed. Rough surface is modelled by Weierstrass-Mandelbrot fractal function. The static force-displacement relationship for the deformable rough surface which comes in contact with a rigid flat surface is determined by Finite Element Analysis (FEA) using the commercial software ANSYS 14.5. Using the static force-displacement relationship, the dynamic characteristics are analyzed for free-undamped as well as for forced-damped condition. The physical system of contact interface between the rough deformable surface and the rigid flat is assumed to be represented by a single degree of freedom (SDOF) spring-mass-damper model. Depending upon the nature of the application of the external excitation, there are two basic variations of the model. First, harmonic excitation force is applied on the mass of the SDOF spring-mass-damper system, while, in the second case harmonic excitation is applied as displacement on the base of the model.

1.5. Present Thesis

The present thesis contains five chapters. The first chapter provides a general introduction to contact vibration of rough surfaces. It also includes a literature review of relevant research work to set the backdrop of the present analysis. The second chapter describes finite element modelling and static force-displacement analysis in ANSYS environment. Dynamic analysis of rough deformable surface for free and forced-damped vibration are presented in third chapter and fourth chapter on the basis of two different models, respectively. The fifth chapter contains the conclusions and future scope of work

Chapter 2

Finite Element Modelling and Analysis

The chapter provides information about modelling of rough fractal surface in MATLAB and later in ANSYS. This chapter also depicts the method and results of the finite element analysis to obtain the force-displacement characteristics of rough fractal surface.

2.1 Introduction

For the analysis of rough surfaces, modelling of realistic rough surface is necessary, which is never a simple procedure. In very preliminary contact surface modelling approaches, the asperities of rough surfaces were assumed to be in geometrical shape like spherical, cylindrical etc. [1, 2, 23, 33, 97]. But in reality rough surfaces are hardly found in such geometrical shape, but found in random shape and size. For that purpose, some statistical modelling [4, 17, 68] was proposed. It has been observed that surface topography is a non-stationary random process, which means the variance of the height distribution is related to the sampling length and hence is not unique for a particular surface. After B. B. Mandelbrot proposed the theory of fractal geometry, it was found that it can be used to model various natural phenomena, such as precipitation, turbulence, and surface topography. Rough surfaces exhibit the feature of self-similarity and self-affinity i.e. similar appearances of the surface can be seen under the various degree of magnification. The measurement parameters of surface roughness depend strongly on the resolution of the roughness-measuring instrument or some other form of filter. Hence same surface can exhibit different measurements for different measuring instruments and scaling parameters.

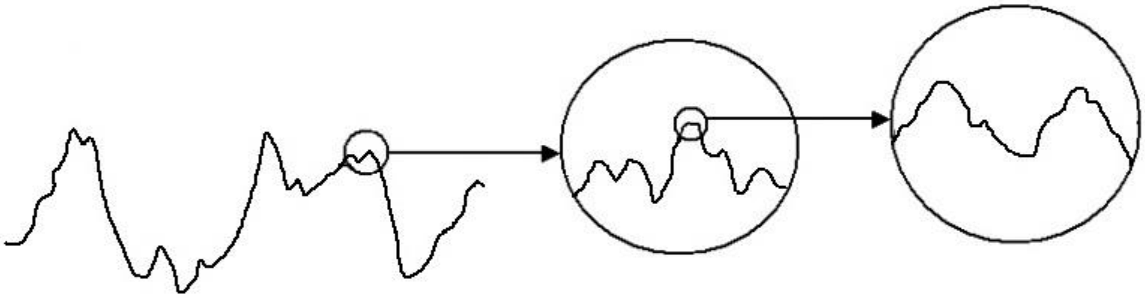

Figure 2.1. Self-affine property of a rough surface profile.

Thus it is necessary to characterize rough surfaces by intrinsic parameters, which are independent of all scales of roughness. This suggests that fractal geometry can be a very efficient tool to model rough surface, since the parameter fractal dimension is an intrinsic property which is invariant with length scales and takes care of the nature of self-similarity.

2.2. Fractal Surface Characterization

The profile of an engineering surface, obtained from stylus measurements, is assumed to be continuous even at the smallest scales. Since repeated magnifications reveal the finer levels of detail, the tangent at any point cannot be defined. Thus the surface profile is continuous everywhere but non-differentiable at all points. These properties are satisfied by the Weierstrass–Mandelbrot (W-M) function given by Berry and Lewis [55]

$$w(x) = \sum_{f=-\infty}^{\infty} \gamma^{(D-2)f} \left(1 - e^{i\gamma^{f} x}\right) e^{i\phi} \tag{2.1}$$

where w is a complex function of real variable x. A fractal profile can be obtained as the real part of $w(x)$.

$$\begin{aligned} z(x) &= \mathrm{Re}\left[w(x)\right] \\ &= \sum_{f=-\infty}^{\infty} \gamma^{(D-2)f} \left[\cos\,(\phi) - \cos\,\left(\gamma^{f} x + \phi\right)\right] \end{aligned} \tag{2.2}$$

Here, D and f are the fractal dimension of the profile and frequency index respectively. ϕ is a random phase and γ $(\gamma > 0)$ is a parameter that determines the density of frequencies in the profile.

Ausloos and Berman [56] modified the W-M function by introducing multiple variables to account for higher-dimensionally stochastic processes. The height function of a 3D fractal surface exhibiting randomness in all planar directions is the real part of the Ausloos–Berman function.

$$z(\rho,\theta) = \left(\frac{\ln\gamma}{M}\right)^{1/2} \sum_{\mu=1}^{M} A_{\mu} \sum_{f=-\infty}^{\infty} \left(k\gamma^{f}\right)^{(D-3)} \left\{ \cos\phi - \cos\left[k\gamma^{f} \rho \cos\left(\theta - \alpha_{\mu}\right) + \phi\right]\right\} \tag{2.3}$$

M and γ are the number of superimposed ridges to construct the surface and frequency density respectively. The anisotropy of the surface geometry is controlled by the magnitude of A_{μ}. The angle α_{μ} is used to offset the ridges in the azimuthal direction. In the present study, the ridges are equally offset, hence, $\alpha_{\mu} = \frac{\pi\mu}{M}$. The parameter k is a wave number related to the sample size

$\left(k = \dfrac{2\pi}{L}\right)$. ρ and θ are the planar polar coordinates of a surface point with height *z*, and are related to the planar Cartesian coordinates, *x* and *y*, by $\rho = \left(x^2 + y^2\right)^2$ and $\theta = \tan^{-1}\left(\dfrac{y}{x}\right)$.

Yan and Komvopoulos [62] modified the equation (2.3) to obtain the final equation

$$z(x,y) = L\left(\frac{G}{L}\right)^{D-2}\left(\frac{\ln\gamma}{M}\right)^{1/2}\sum_{\mu=0}^{M}\sum_{f=0}^{f_{\max}}\gamma^{(D-3)f} \times \left\{\cos(\phi) - \cos\left[\frac{2\pi\gamma^{f}\left(x^2+y^2\right)^{1/2}}{L_0} \times \cos\left(\tan^{-1}\left(\frac{y}{x}\right) - \frac{\pi\mu}{M}\right) + \phi\right]\right]\right\}$$

(2.4)

L is the sample length, and G is a height scaling parameter independent of frequency within the scale range, wherein fractal power law behavior exists. Frequency index is represented by f . Frequency index has a lower limit at zero for a truncated series of the height function and the upper limit is given by,

$$f_{\max} = \operatorname{int}\left[\frac{\log\left(L/L_s\right)}{\log\gamma}\right] \tag{2.5}$$

Where, $\operatorname{int}[.]$ represents the maximum integer value of the number within the bracket and L_s is the cut off length, which is in the order of about six lattice distances. For physical rough surfaces the value of fractal dimension is found to be between 2 and 3 $(2 < D < 3)$.

2.3. Fractal Surface Generation

The height (z coordinate) of the fractal surface for the corresponding (*x*, *y*) points are obtained using the modified Weierstrass– Mandelbrot equation [equation (2.4)] in MATLAB. The values of sample length (L) and cut-off length (L_s) is set to be 1×10^{-6} m and 1.5×10^{-7} m respectively. The parameters M and γ has values of 1 and 1.5, respectively. The 3D surface is plotted using the (x, y, z) coordinate points in MATLAB, which represent a 3D isotropic fractal surface.

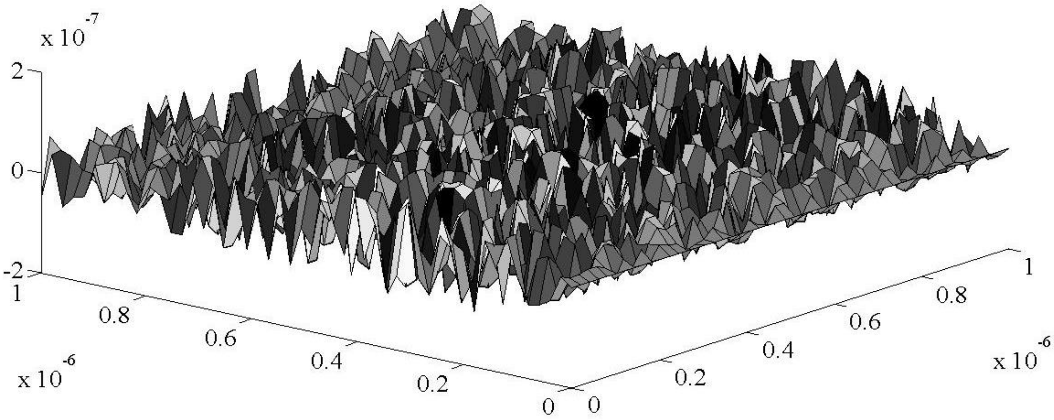

Figure 2.2. MATLAB generated fractal surface with $D = 2.3$, $G = 1.36\times10^{-11}$ m in 50×50 grid.

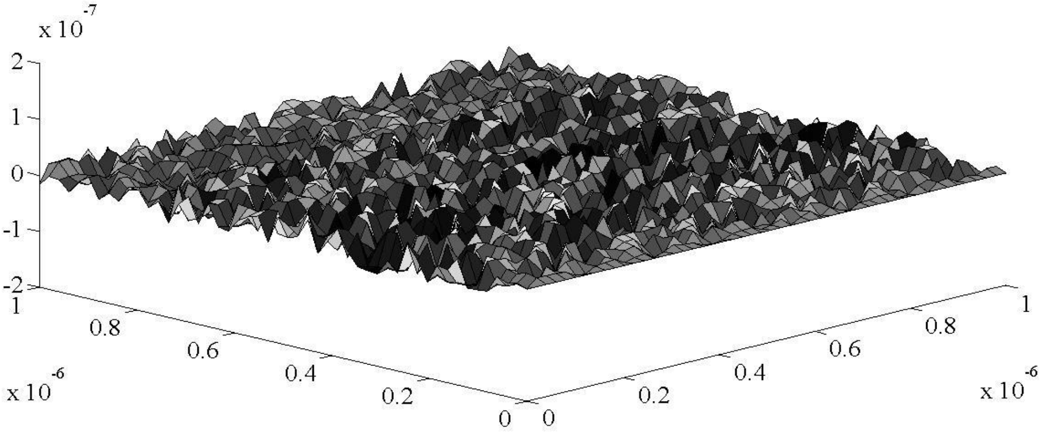

Figure 2.3. MATLAB generated fractal surface with $D = 2.4$, $G = 1.36\times10^{-11}$ m in 50×50 grid.

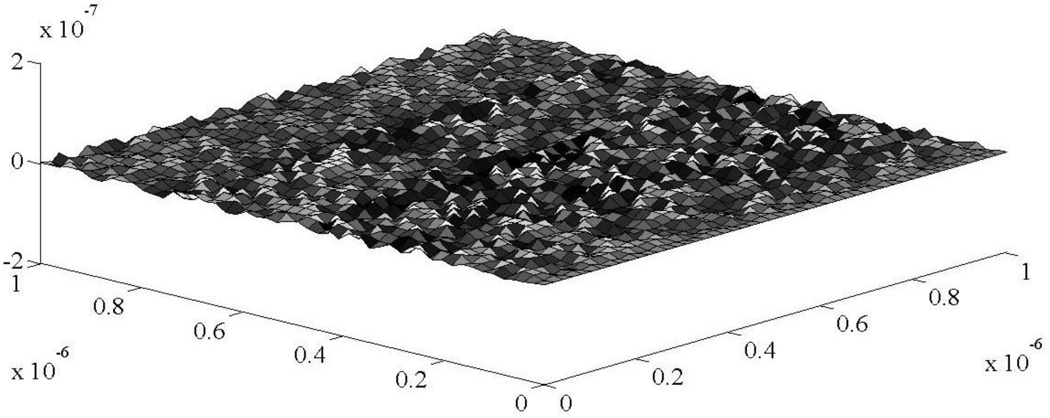

Figure 2.4. MATLAB generated fractal surface with $D = 2.5$, $G = 1.36\times10^{-11}$ m in 50×50 grid.

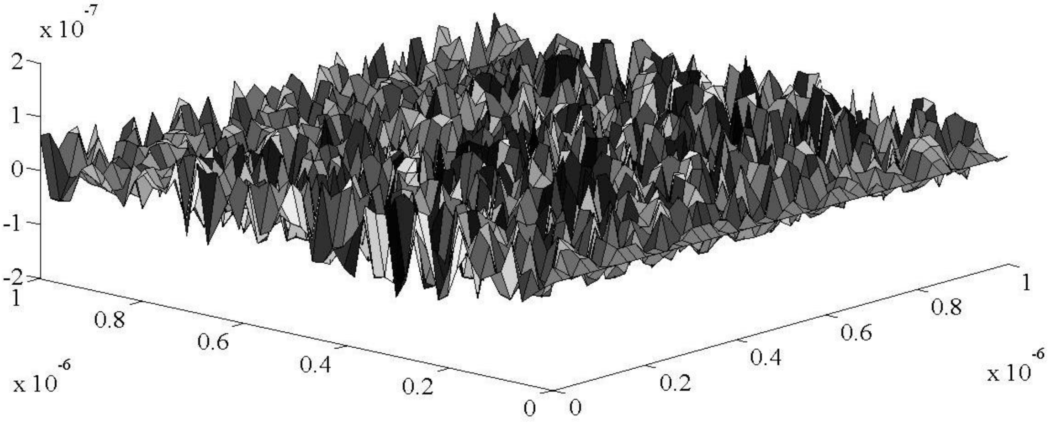

Figure 2.5. MATLAB generated fractal surface with $D = 2.4$, $G = 1.36\times10^{-10}$ m in 50×50 grid.

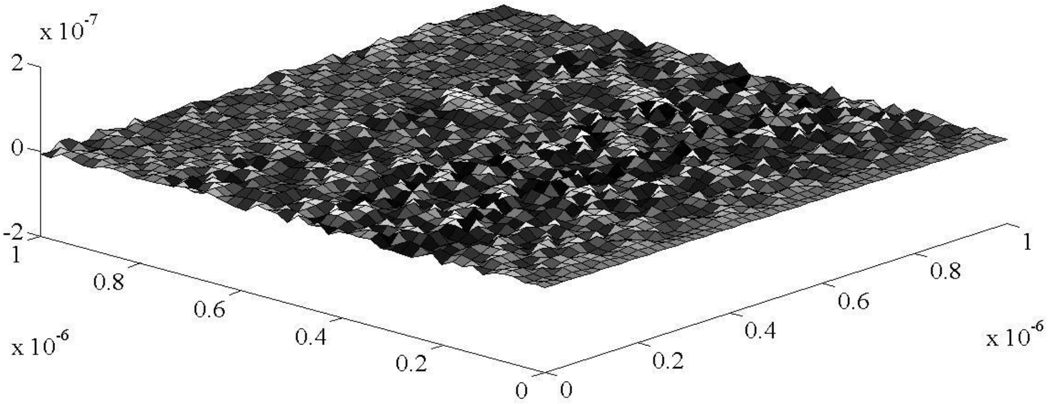

Figure 2.6. MATLAB generated fractal surface with D = 2.4, G = 1.36×10^{-12} m in 50×50 grid.

From the figures given above, it can be clearly seen that lower D value and higher G value corresponds to rougher and less dense surface topography and vice-versa. The magnitude of the fractal dimension D describes the contribution of high and low frequency components in the surface function. Thus, high values of D indicate that high-frequency components are more dominant than low-frequency components in the surface topography profile. Hence the topography is denser for this case. For higher G value, the difference between the amplitude of high and low frequency increases causing a rougher topography. As mentioned earlier, the surface height function provided by the equation (2.4) is continuous, non-differentiable, scale-invariant (within the range determined by the upper and lower wavelengths used in the truncated series) and self-affine asymptotically. Hence if the surface is repeatedly magnified, more and more surface features appear and the magnified image shows a close resemblance to that of the original surface obtained at different scale.

2.4. Finite Element Modelling

Finite element modeling is used for obtaining numerical solution of contact problems involving the variations of different contact parameters like contact load, real contact area, mean contact pressure etc. Commercial finite element software ANSYS 14.5 is used to analyze rough surface contact involving both geometric and material nonlinearity. Solving a contact problem in ANSYS involves the following steps.

- ***Preprocessing:*** Input data describing geometry, discretization of the geometric model by dividing it into a mesh (particular arrangement of elements) of a suitable finite element, and the material properties, loads and boundary conditions are provided by the user. For parametric study, numerous material properties subjected to varying loads are presented in the following chapters.
- ***Solution:*** Elements are connected at points called nodes. Numerically, a finite element mesh is represented by a system of algebraic equations to be solved for unknowns at nodes. Identification of the nature of the problem, for example time independence, non-linearity, large static deformation etc. determine the solution method.
- ***Postprocessing:*** The finite element solution and quantities derived from it are listed or graphically displayed.

2.4.1. Generation of Rough Surface in ANSYS

The generated co-ordinate points of the fractal surface are imported to ANSYS as keypoints by defining array parameter. To construct a cubic block on which the rough surface is to lay, additional keypoints are generated, keypoints are joined to construct lines and areas are created with the lines using ‘*do’ loop. And finally a cubic solid block of dimension 1µm×1µm×1µm is generated with the top surface rough.

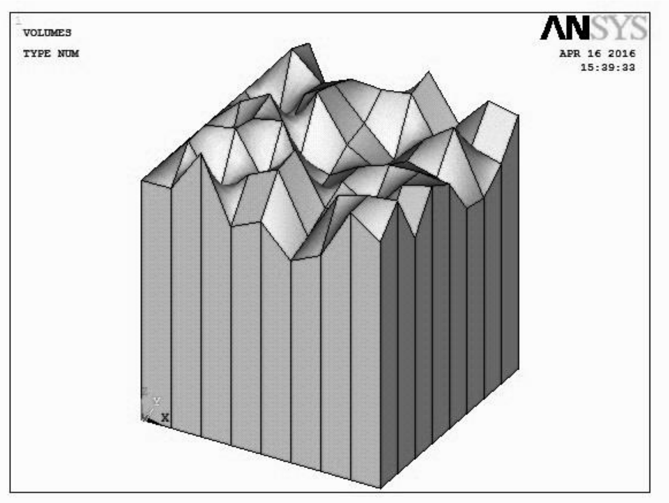

Figure 2.7. Fractal surface with $D = 2.3$, $G = 1.36\times10^{-10}$ m modelled in ANSYS.

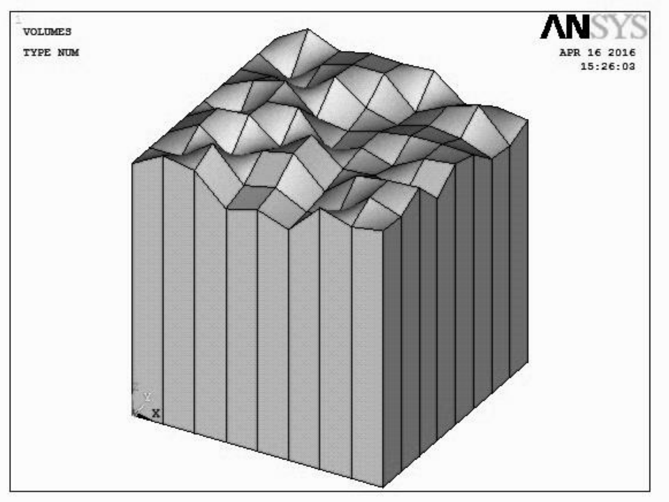

Figure 2.8. Fractal surface with $D = 2.3$, $G = 1.36\times10^{-11}$ m modelled in ANSYS.

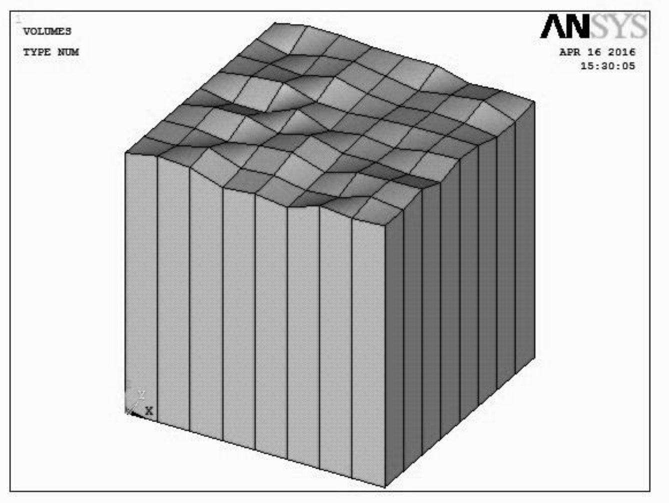

Figure 2.9. Fractal surface with $D = 2.4$, $G = 1.36\times10^{-11}$ m modelled in ANSYS.

2.4.2. Modelling and Meshing

Before the analysis is done, it is necessary to set the material properties and mesh the model with appropriate elements. The model is meshed such way that the contact elements overlay the solid elements. Hence the solid cube is meshed with SOLID element and the rough surface on the top is meshed with CONTA elements. The top-most node (with the highest *z* coordinate value) of the rough surface is identified and a rectangular 2D flat surface is generated on that node. Hence the flat surface just touches the top-most point of the rough surface and any downward motion of the flat would cause deformation of the rough surface.

During the force-displacement analysis of the deformable rough surface, the CONTA elements comes in contact with 2D rigid target element. The functional properties of the elements used can be set through key options of the elements. The elements used in present analysis [97] are given bellow.

2.4.2.1. SOLID187

SOLID187 element is a higher order 3D, 10-node structural solid element of tetrahedral shape. It has a quadratic displacement behavior. The element is defined by 10 nodes having three degrees of freedom at each node i.e. translations in the nodal *x*, *y*, and *z* directions. The element has plasticity, hyper elasticity, creep, stress stiffening, large deflection, and large strain capabilities. It also has mixed formulation capability for simulating deformations of nearly incompressible elastoplastic materials, and fully incompressible hyper elastic materials. SOLID187 is well suited to model irregular meshes. The geometry, node locations and the element co-ordinate system for this element are shown in Figure 2.10.

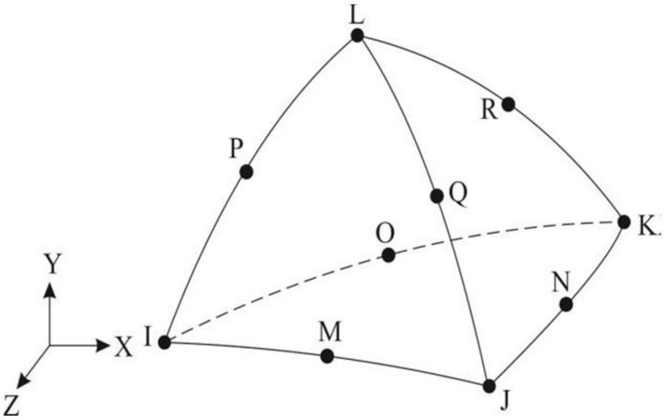

Figure 2.10. Geometry of structural solid element SOLID187.

2.4.2.2. SOLID185

SOLID185 is used for the three-dimensional modelling of solid structures. The element is defined by eight nodes having three degrees of freedom at each node: translations in the nodal x, y and z directions. The element has plasticity, stress stiffening, large deflection, and large strain capabilities. It also has mixed formulation capability for simulating deformations of nearly incompressible elastoplastic materials, and fully incompressible hyper-elastic materials similar as SOLID187. SOLID185 Structural Solid is suitable for modelling general 3-D solid structures. It allows for prism and tetrahedral degenerations when used in irregular regions. The geometry, node locations and the element co-ordinate system for this element are shown in Figure 2.11.

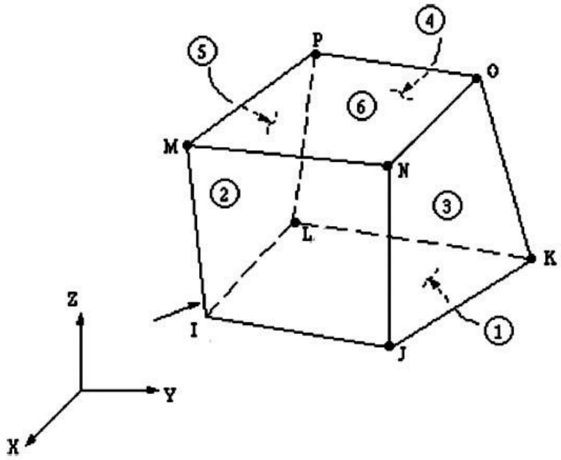

Figure 2.11. Geometry of structural solid element SOLID185.

2.4.2.3. CONTA174

CONTA174 is an 8-node contact element used to represent contact and sliding between 3D target surfaces and a deformable surface. The element is applicable to 3D structural and coupled field contact analyses for surface to surface contact. The element is located on the surfaces of 3D solid or shell elements with nodes at the midpoints of its sides. It has the same geometric characteristics as the solid or shell element face with which it is connected. Contact occurs when the element surface penetrates one of the target segment elements on a specified target surface. Coulomb friction, shear stress friction, and user-defined friction are allowed for this element. The element also allows separation of bonded contact to simulate interface delamination.

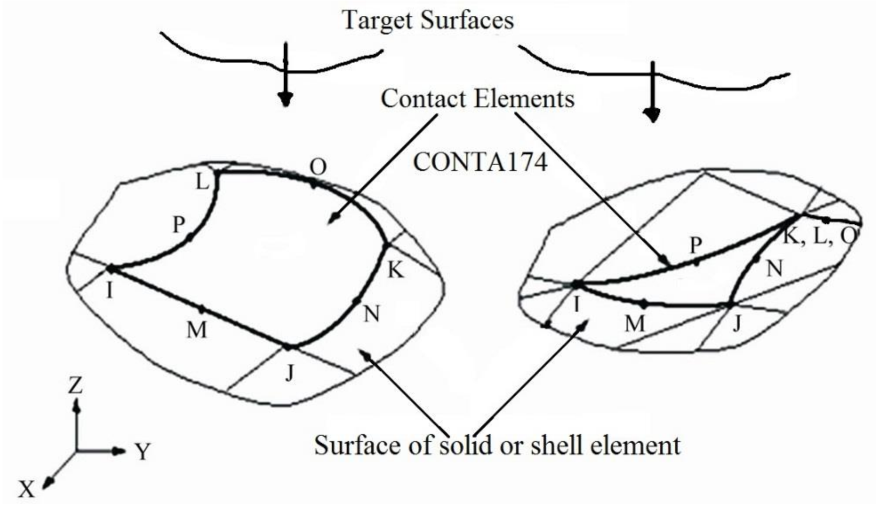

Figure 2.12. Geometry of CONTA174 and interaction with target surface.

2.4.2.4. TARGE170

TARGE170 is used to represent various 3D target surfaces for the associated contact elements. The contact elements overlay the solid elements describing the boundary of a deformable body and are potentially in contact with the target surface, defined by TARGE170. This target surface is discretized by a set of target segment elements and is paired with its associated contact surface via a shared real constant set. Any translational or rotational displacement or forces and moments can be imposed on the target segment element. For rigid target surfaces, complex target shapes can be easily modelled with these elements. For flexible targets, these elements overlays the solid elements describing the boundary of the deformable target body.

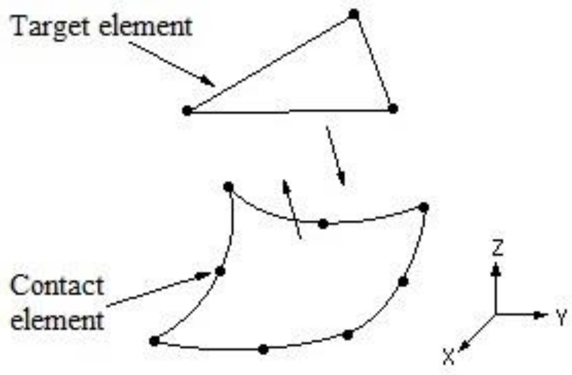

Figure 2.13. Geometry of TARGE170 and interaction with contact element.

Hence, the TARGET surface is meshed with TARGE170 element which comes in contact with the CONTA174 elements overlaying the SOLID187 or SOLID185 elements. For example, the resulting mesh for the surface having the values $D = 2.3$ and $G = 1.36\times10^{-11}$ m consists of 22375 SOLID187 elements, 3448 CONTA174 elements and 10 TARGE170 elements and for the surface with $D = 2.4$ and $G = 1.36\times10^{-11}$ m the resulting mesh consists of 26188 SOLID187 elements, 3672 CONTA174 elements and 10 TARGE170 elements.

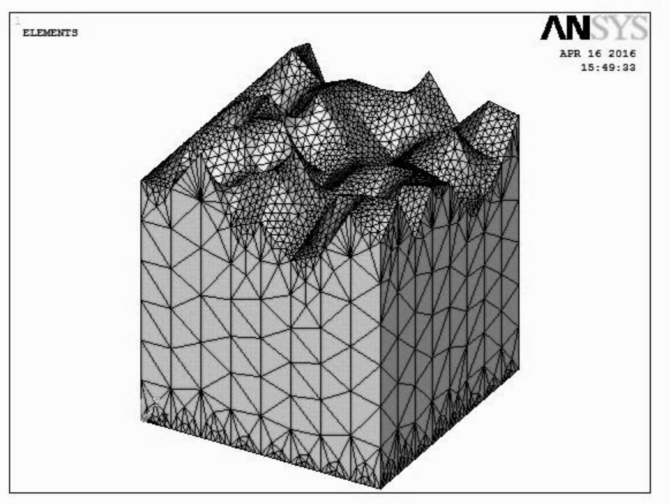

Figure 2.14. Fractal surface with $D = 2.3$, $G = 1.36\times10^{-10}$ m after meshing.

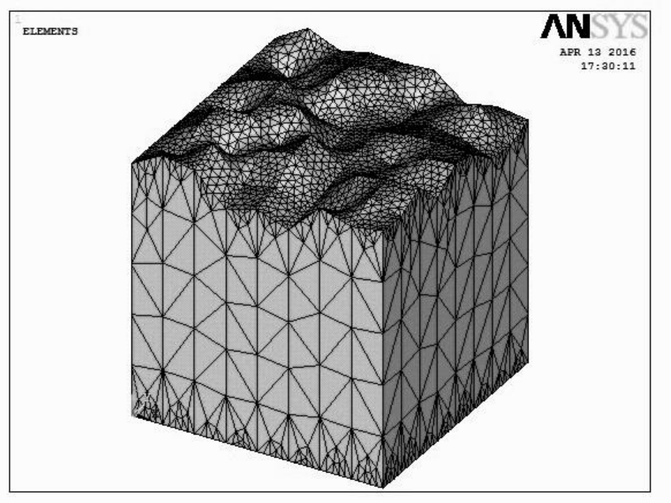

Figure 2.15. Fractal surface with $D = 2.3$, $G = 1.36\times10^{-11}$ m after meshing.

A pilot node is chosen at the centre of the rigid target surface where external load/displacement is to be applied. The rigid flat is constrained to move in all directions except in z direction. And all the nodes at the bottom of the solid elements i.e. all the nodes at $z = 0$ are constrained to move in all the directions. The contact with the rigid plane is realized using surface-to-surface contact elements that use the augmented Lagrangian method for solving. [95]

2.5. Finite Element Analysis and Solution

For the current analysis the solid element is meshed with 10-node structural solid element SOLID187 and the contact and the target elements are meshed with CONTA174 and CONTA170 respectively. The rigid surface just touches the top-most node of the rough surface.

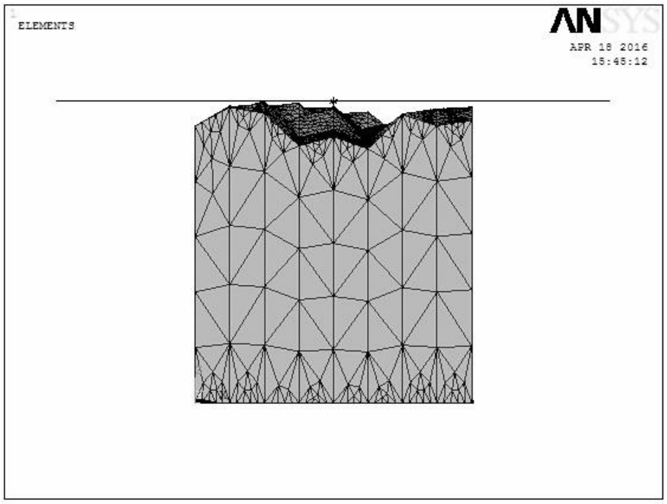

Figure 2.16. Meshed model of rough surface in contact with rigid flat surface. (The point with * sign indicates the pilot node).

A downward displacement is imparted on the rigid surface incrementally with 100 sub-steps to come in contact and deform the deformable rough surface. After the solution is obtained, the reaction force at the contact surface is recorded.

2.5.1. Solution procedure in Finite Element Analysis

In present study, the Finite Element Analysis solution is obtained by the utilization of the augmented Lagrangian method. The rough surface contact problem and the material property make the analysis highly nonlinear and difficult to converge. An iterative scheme is necessary to get the solution in reasonable time. Loads are applied in number of steps to enhance solution convergence. Higher is the load step, higher is the chance of getting converged solution as well as higher is the solution time. Initially, a small interference is set of the total interference and then it is incremented after the load step converges. Each load step consists of 10 to 100 substeps. If the load is not applied in sufficient number of substeps, the elements gets distorted and converged solution cannot be obtained. As a solution, ANSYS internally controls the load stepping to obtain a converged solution by using the bisection method. The augmented Lagrangian method is an iterative series of penalty methods, where a contact ‘spring’ is used to establish a relationship between two contact surfaces. In this method the resultant contact forces are applied as external forces and the system is solved again for contact with the penalty method. The procedure continues until the gap reduces to a reasonable value. It is a combination of penalty method and Lagrangian multiplier method to utilize the advantage of both. In this method, the normal force for the contact spring (i.e. normal pressure between the contacting surfaces) is taken as.

$$F_{normal} = k_{normal} x_{penetration} + \lambda \tag{2.6}$$

where, F , k and x are the contact force, stiffness and displacement respective and λ is the penalty term. The contact tractions (pressure and frictional stresses) are augmented during equilibrium iterations so that the final penetration is smaller than the allowable tolerance Compared to the penalty method, the augmented Lagrangian method usually leads to better conditioning and is less sensitive to the magnitude of the contact stiffness. To enhance convergence for augmented Lagrangian method, the program automatically adjusts the stiffness based on the current mean stress of the underlying elements and allowable penetration. However, in some analyses, the augmented Lagrangian method may require additional iterations, especially if the deformed mesh becomes too distorted.

2.5.2. Validation Study

Buzio et al. [96] studied the load deflection behavior between atomic force microscope (AFM) probes and self-affine fractal carbon films. They presented the experimental results for multiple asperity contact between nanostructured carbon and AFM probe. The AFM imaging provides fractal dimension $D = 2.3$ and fractal roughness $G = 1.55\times10^{-10}$ m along with the nominal contact area $A_0 = 4.8\times10^{-12}$ m^2. The material properties for the system were taken as, equivalent composite elastic modulus $\left(E'=\dfrac{E}{1-\nu^2}\right)$ 0.88 GPa, tangent modulus (E_t) zero, Poisson's ratio (ν) 0.3 and yield strength (Y) 16.07 MPa. Keeping the material and fractal properties same, the force-displacement analysis is carried out in ANSYS. SOLID185, TARGE170 and CONTA174 elements are used to construct the solid, target and contact elements respectively during the finite element analysis. Downward force (towards negative z direction) is applied on the pilot node causing downward displacement of the rigid flat as well as the deformable rough surface due to deformation. The displacement is recorded from the analysis. The result is in favorable agreement with the experimental result by Buzio et al. as well as with the result furnished by Chatterjee and Sahoo [77]. Non-dimensional displacement $\left(\delta^* = \dfrac{\delta}{L}\right)$ is plotted against non-dimensional load $\left(P^* = \dfrac{P}{A_0 E'}\right)$. P is the applied load, δ is the displacement and L is the sample length. E' and A_0 are equivalent composite elastic modulus and nominal contact area respectively.

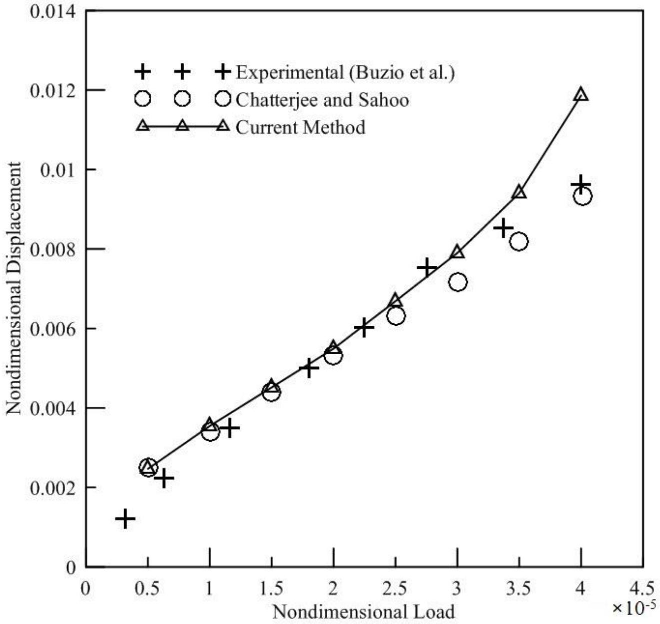

Figure 2.17. Comparison with the results of Chatterjee and Sahoo [77] and Buzio et al. [96].

2.5.3. Results of Finite Element Analysis

Non-dimensional load $\left(P^* = \frac{P}{A_0 E'}\right)$ is plotted against non-dimensional displacement $\left(\delta^* = \frac{\delta}{L}\right)$ and the force-displacement curves are fitted in a power law relationship in the form

$$P^* = k\left(\delta^*\right)^n \tag{2.7}$$

where k is the non-linear stiffness of the rough surface which is a constant parameter with positive value and the parameter n is the measure of nonlinearity of the contact interaction. The parameter 'n' could be termed as nonlinearity exponent. First, force-deflection relation of the deformable rough surface in contact with a rigid flat is analyzed varying the surface properties. The fractal dimension D is varied from 2.3 to 2.6 and fractal roughness parameter keeping the fractal roughness G constant at 1.36×10^{-10} m. Then the value of fractal roughness is varied from 1.36×10^{-10} m to 1.36×10^{-13} m keeping the value of fractal dimension constant at 2.4. The material is taken as infinitely linear elastic i.e. no yielding occurs up to infinite stress. The elastic modulus and the Poisson's ratio of the material is taken as 200 GPa and 0.3 respectively.

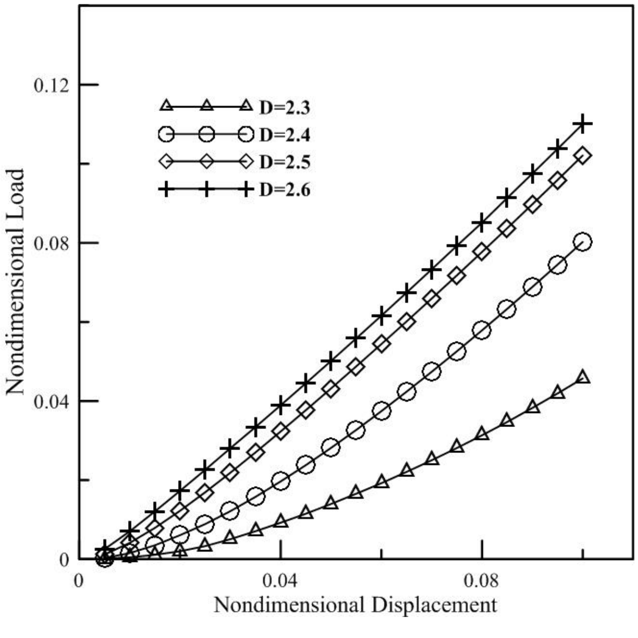

Figure 2.18. Plots of non-dimensional force versus non-dimensional displacement of rough surfaces for varying fractal dimension (D).

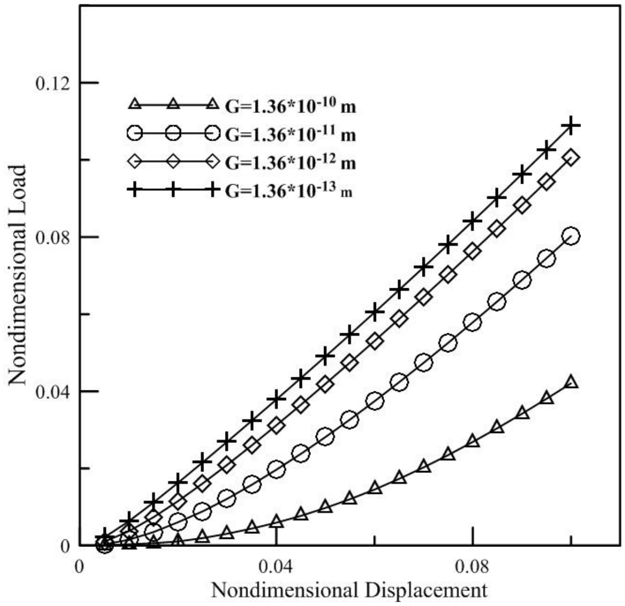

Figure 2.19. Plots of non-dimensional force versus non-dimensional displacement of rough surfaces for varying fractal roughness parameter (G).

The curves are fitted in a power law relationship in the form of equation (2.7) to obtain the values of the nonlinear stiffness (k) and the nonlinearity exponent (n). The values for different fractal dimension and fractal roughness parameters values are shown in table 2.1.

Table 2.1. Values of nonlinear stiffness (k) and nonlinearity exponent (n) for different fractal dimension (D) and fractal roughness (G) values.

Fractal Roughness (G)	**Fractal Dimension** (D)	**Nonlinear stiffness** (k)	**Nonlinearity exponent** (n)
1.36×10^{-11} m	2.3	2.5751	1.74723
1.36×10^{-11} m	2.4	2.7927	1.5372
1.36×10^{-11} m	2.5	1.9254	1.2719
1.36×10^{-11} m	2.6	1.5275	1.1421
1.36×10^{-10} m	2.4	5.4703	2.1092
1.36×10^{-12} m	2.4	1.9939	1.2934
1.36×10^{-13} m	2.4	1.5909	1.1638

Since the *n* value is a measure of nonlinearity, it can be seen that nonlinearity increases for rougher surface topography i.e. higher fractal roughness parameter (G) and lower fractal dimension (D) and vice versa.

The previous plots are presented under the assumption of infinite linear elasticity, which is not practical. To investigate the dynamic contact behaviour in post elastic domain, it is required to define the yield strength along with tangent modulus. Now, keeping the surface properties fixed at $D = 2.4$ and $G = 1.36\times10^{-11}$ m, force-displacement relationship is analyzed for the variation of material property of the rough deformable surface. The material is considered to yield and behave according to a bilinear model after yielding. Yield strength (Y) is considered to be fixed at 250 MPa and the value of the tangent modulus (E_t) is varied as 100 GPa, 60 GPa and 10 GPa. The elastic modulus and Poisson's ratio is set fixed at the previously mentioned value. Finite element analysis is applied to obtain the force-displacement relationship of the rough surface for different tangent modulus values.

Non-dimensional load versus non-dimensional displacement curve for the variation of tangent modulus is presented in Figure 2.20.

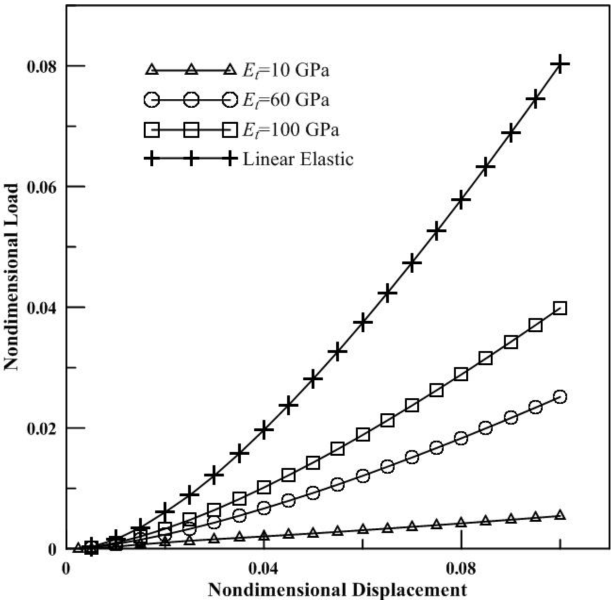

Figure 2.20. Plots of non-dimensional force versus non-dimensional displacement of rough surface for varying tangent modulus (E_t).

The load-deflection behaviour under varying yield strength with constant tangent modulus has also been studied. The elastic modulus, Poisson's ratio and the tangent modulus is set fixed at 200 GPa, 0.3 and 10 GPa respectively and yield strength is varied as 250 MPa, 560.8 MPa, 911.5 MPa, 1265.3 MPa and 1619 MPa. These yield strength values cover a range of steels used in engineering applications [33, 75]. The non-dimensional force-displacement curves obtained from the finite element analysis are showed in Figure 2.21.

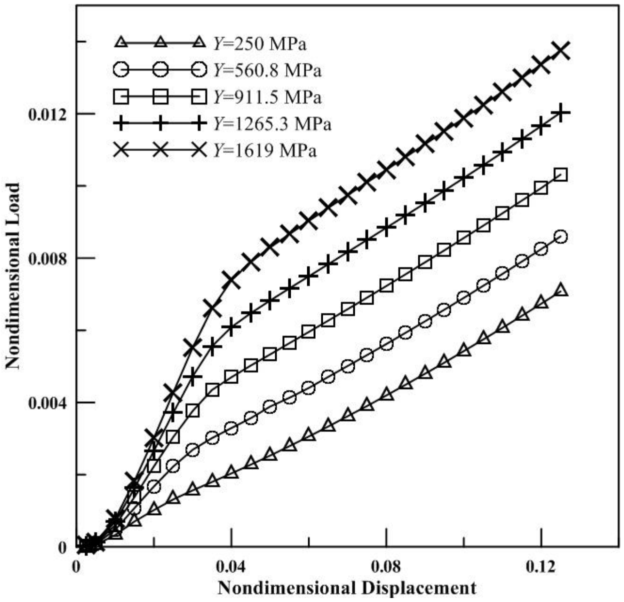

Figure 2.21. Plots of non-dimensional force versus non-dimensional displacement of rough surface for varying yield strength (Y).

The curves for the variation of tangent modulus and yield strength of the deformable surface are fitted in a power law relationship in the form of equation (2.7) to obtain the values of the nonlinear stiffness (k) and the nonlinearity exponent (n).

Table 2.2. Values of nonlinear stiffness (k) and nonlinearity exponent (n) for different tangent modulus (E_t) and yield strength (Y) values.

Yield Strength (MPa)	**Tangent Modulus** (GPa)	**Nonlinear stiffness** (k)	**Nonlinearity exponent** (n)
N/A	Linear Elastic	2.7927	1.5372
250	100	1.2666	1.4989
250	60	0.71652	1.453
250	10	0.06957	1.1057
560.8	10	0.05301	0.8816
911.5	10	0.05112	0.7709
1265.3	10	0.05416	0.7174
1619	10	0.05944	0.6914

It can be observed that for higher tangent modulus value, the surface exhibits higher nonlinearity. The nonlinearity exponent (n) is found to decrease with the increase of yield stress value. For the yield strength values 560.8 MPa, 911.5 MPa, 1265.3 MPa, and 1619 MPa, the n value is found to be less than 1.

2.6. Summary

In the present chapter, coordinate points constructing fractal surface are generated from the modified Weierstrass-Mandelbrot function in MATLAB and are imported to ANSYS as keypoints by defining array parameters. Additional keypoints are created and used to construct a cubic solid block of dimension 1μm × 1μm × 1μm on which the rough deformable surface is to lay. The deformable surface comes in contact with a 2D rigid flat. Any downward motion of the rigid flat surface results deformation of the rough surface. Finite element analysis is applied to obtain the force-displacement relationship of the rough surface. The obtained force-displacement curve from finite element analysis is fitted in a power law curve to obtain nonlinear contact bulk stiffness and a parameter called ‘nonlinearity exponent’ which provides the measure of nonlinearity of the contact system. The values of these two parameters are determined for the variation of surface roughness and material property of the deformable surface. It has been observed that, the nonlinearity of the system increases with the increase of surface roughness, tangent modulus and with the decrease of yield strength.

Chapter 3

Dynamic Analysis of Rough Fractal Surface: Model I

The chapter provides an analysis on free undamped and forced damped vibration of deformable rough fractal surface in contact with a solid flat surface and also the effect of surface roughness and material properties on it.

3.1. Introduction

It is well known that if an elastic body is given a small disturbance from its stable equilibrium position, it starts vibrating about the equilibrium position. For the case of rough contacting surfaces the same phenomenon takes place. Under the influence of any type of external disturbance and excitation, vibration/oscillation takes place at the contact interface. In engineering components like gears, belt drives, cam-followers etc. vibration at contact surfaces is a very common and influential phenomenon. The amplitude of the vibration at the contact surface are often found to be very low and hence it is not an easy task to measure the vibration parameters of the contact surfaces. But a theoretical study can be presented to obtain characteristics of the dynamic behaviour of such systems.

3.2. Dynamic Model

The present dynamic system consists a deformable body of mass *m* with a rough surface at the top and a rigid flat surface capable of vertical motion. While in motion, the rigid flat comes in contact with the rough surface causing deflection at its multiple asperities as shown in Figure 3.1. However, the rough surface is considered to be deflected with a bulk stiffness *k* for the entire surface. The dynamic behaviour of the contacting system is dependent on the force-displacement relationship of the surface which is analysed in chapter 2.

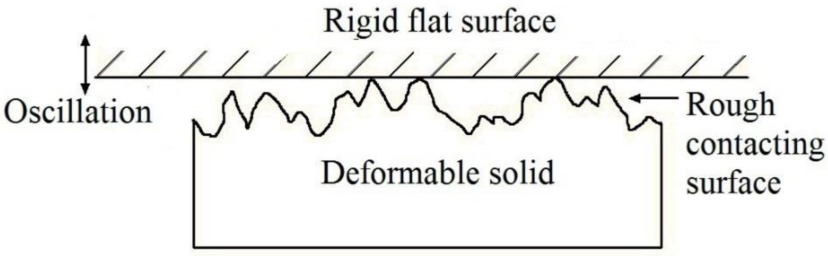

Figure 3.1. Model of the deformable surface coming in contact with rigid flat surface.

For the sake of dynamic analysis, the dynamic contact system is equivalently modelled as a single degree of freedom spring-mass-damper system (Figure 3.2.) which is considered to be valid for low frequency behaviour only [64]. The mass of the block (*m*) is equal to the mass of the deformable body whereas the spring stiffness is taken as the bulk stiffness of the surface. The mass rests on a vertical spring and a viscous damper. It should be pointed out that the spring is non-linear in nature. On the other hand, damping model is considered to be linear and viscous, with linear damping co-efficient *c*.

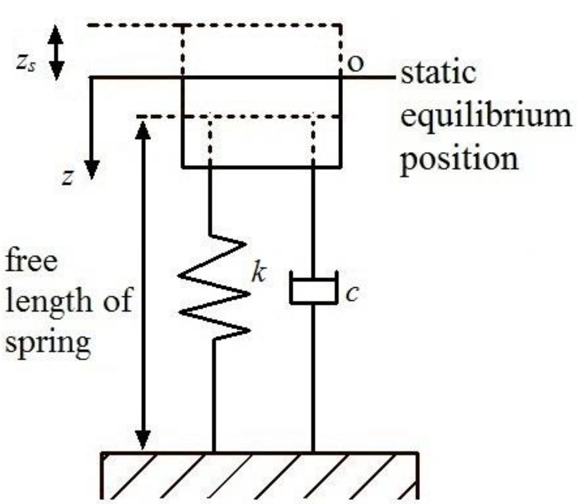

Figure 3.2. SDOF model representation of the dynamic contact model.

The vertical displacement of the system is denoted by *z*. The spring undergoes a deflection of z_s due to the weight of the block and the static equilibrium position of the system is denoted by 'o' as shown in Figure 3.2. Under any form of excitation the mass vibrates vertically about the static equilibrium position. Once the mass is disturbed from its static equilibrium and is in motion, the restoring force is supplied by the nonlinear spring, which models the load-displacement characteristic at the contact interface. Hence, the force-displacement behaviour at the contact between deformable rough surface and rigid flat, studied through a finite element analysis in the previous chapter (chapter 2), is imposed on the spring as its nonlinear force-displacement behaviour. So, the spring force is expressed as a nonlinear function of spring displacement as follows

$$F_s = k\left(z + z_s\right)^n \tag{3.1}$$

where F_s is the restoring force, *k* is the nonlinear stiffness of the spring and *n* is the nonlinearity exponent. It should be mentioned here that, different *k* and *n* values are obtained as the output of the FE analysis performed in chapter 2, corresponding to various combination of fractal surface profile parameters and material properties. These *k* and *n* values are the input parameters for the present dynamic analysis.

Considering damping and weight of the block, the equation of motion of the system at any time instant ‘t’ can be written as

$$m\ddot{z} + c\dot{z} + k(z + z_s)^n - mg = F\cos(\omega t) \tag{3.2}$$

where *F* denotes the amplitude of the harmonic excitation force, while ω is the forcing frequency. From the force-displacement relationship we obtain the static deflection of the spring is obtained as

$$z_s = (mg / k)^{1/n} \tag{3.3}$$

This equation of motion is only valid when the rough surface is in contact with the rigid flat surface, i.e. $z \geq -z_s$. Beyond this limit contact loss occurs and the rough surfaces does not remain in contact with the rigid flat.

To generalize the equation of motion for different domain of parameters it is required to normalize the equation. For this purpose certain non-dimensional parameters are introduced.

$u = \frac{z}{z_s}$, $\Omega = \frac{\omega}{\omega_s}$, $\tau = \omega_s t$,and $\zeta = \frac{c}{2m\omega_s}$

Natural frequency at the static equilibrium position, $\omega_s = \sqrt{\frac{nkz_s^{n-1}}{m}}$ is utilized to normalize the external forcing frequency, time and damping coefficient. *u*, Ω, τ and ζ are normalized displacement, frequency, time and damping ratio respectively. After normalizing, the equation motion can be written in the following form,

$$u'' + 2\zeta u' + \frac{1}{n}\left[(n+1)^n - 1\right] = \frac{1}{n}\hat{F}\cos(\Omega\tau) \tag{3.4}$$

where, the non-dimensional excitation force is represented as $\hat{F} = F / mg$ and $'$ denotes differentiation w.r.t. non-dimensional time. The expression $(u+1)^n$ is expanded into a third order Taylor series expansion and hence equation (3.4) becomes

$$u'' + 2\zeta u' + u + \alpha_2 u^2 + \alpha_3 u^3 = \frac{1}{n}\hat{F}\cos(\Omega\tau) \tag{3.5}$$

where, $\alpha_2 = \frac{(n-1)}{2}$ and $\alpha_3 = \frac{(n-1)(n-2)}{6}$

The governing differential equation describes linearly damped forced vibration of the contact interface under external harmonic excitation force. As the equation contains both quadratic and cubic nonlinearity terms, it can be classified as a Duffing-Helmholtz type equation with natural frequency value (ω_n) of unity. Primarily it can be noted that level of nonlinearity of the dynamic system increases with the increase of the coefficient of the quadratic and cubic term of the equation, i.e. α_2 and α_3, which are dependent on the value of nonlinearity exponent (*n*).

3.3. Numerical Solution methods

In the present work, ordinary differential equations and integrations are computed numerically in MATLAB environment using numerical ODE solver *'ode45*' and numerical integration subroutine '*quad*' which are based on Runge-Kutta method and adaptive Simpson's quadrature method respectively.

3.3.1. Runge-Kutta Method

Runge-Kutta Method is an efficient iterative method used in temporal discretization for the approximate solutions of ordinary differential equations[100,101]. In the Runge-Kutta method of first order (or Euler's method) the approximate numerical solution of the ordinary differential equation of the following form is obtained

$$y' = f(x, y) \tag{3.6}$$

with the initial value, $y(x_0) = y_0$ (3.7)

The interval between the initial and the final point is divided into small subdivisions of length h. Then, using the initial condition as our starting point, rest of the solution is generated by using the iterative formulas

$$x_{n+1} = x_n + h \tag{3.8}$$

$$y_{n+1} = y_n + h.f(x_n, y_n) \tag{3.9}$$

But this method is not accurate. So, to increase the accuracy of the solution a trial step is taken at the midpoint of the interval. Then use the value of both *x* and *y* at that midpoint is used to compute the real step across the whole interval.

$$k_1 = h.f(x_n, y_n) \tag{3.10}$$

$$k_2 = h.f\left(x_n + \frac{h}{2}, y_n + \frac{k_1}{2}\right) \tag{3.11}$$

$$y_{n+1} = y_n + k_2 + O\left(h^3\right) \tag{3.12}$$

The above mentioned technique is known as the second-order Runge-Kutta or midpoint method. However the most popular and often utilized method is the classical fourth-order Runge-Kutta formula which can be obtained by extending the above procedure in a similar way.

$$k_1 = h.f(x_n, y_n) \tag{3.13}$$

$$k_2 = h.f\left(x_n + \frac{h}{2}, y_n + \frac{k_1}{2}\right) \tag{3.14}$$

$$k_3 = h.f\left(x_n + \frac{h}{2}, y_n + \frac{k_2}{2}\right) \tag{3.15}$$

$$k_4 = h.f(x_n + h, y_n + k_3) \tag{3.16}$$

$$y_{n+1} = y_n + \frac{k_1}{6} + \frac{k_2}{3} + \frac{k_3}{3} + \frac{k_4}{6} + O\left(h^5\right) \tag{3.17}$$

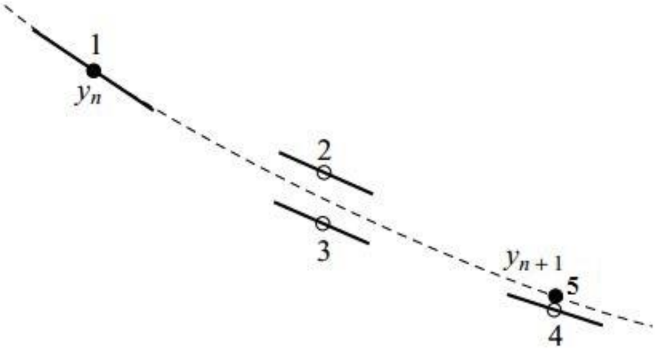

Figure 3.3. Initial solution point (Point 1), trial midpoints (Point 2 and 3), trial endpoint (Point 4) and final endpoint (Point 5) for fourth order Runge-Kutta method [100].

In the present analysis, the non-linear ordinary differential equation, derived in the previous section is solved using MATLAB ODE solver ‘*ode45*’ of MATLAB which utilizes Dormand-Prince method for to obtain the solution. Dormand-Prince method is an adaptive Runge-Kutta method based on Runge-Kutta method of order 4. The one step calculation in the Dormand-Prince method is done as shown through the following expressions.

$$k_1 = h.f\left(x_n, y_n\right) \tag{3.18}$$

$$k_2 = h.f\left(x_n + \frac{h}{5}, y_n + \frac{k_1}{5}\right) \tag{3.19}$$

$$k_3 = h.f\left(x_n + \frac{3h}{10}, y_n + \frac{3k_1}{40} + \frac{9k_2}{40}\right) \tag{3.20}$$

$$k_4 = h.f\left(x_n + \frac{4h}{5}, y_n + \frac{44k_1}{45} - \frac{56k_2}{15} + \frac{32k_3}{9}\right) \tag{3.21}$$

$$k_5 = h.f\left(x_n + \frac{8h}{9}, y_n + \frac{19372k_1}{6561} - \frac{25360k_2}{2187} + \frac{64448k_3}{96561} - \frac{212k_4}{729}\right) \tag{3.22}$$

$$k_6 = h.f\left(x_n + h, y_n + \frac{9017k_1}{3168} - \frac{355k_2}{33} - \frac{46732k_3}{5247} + \frac{49k_4}{176} - \frac{5103k_5}{18656}\right) \tag{3.23}$$

$$k_7 = h.f\left(x_n + h, y_n + \frac{35k_1}{384} + \frac{500k_3}{1113} + \frac{125k_4}{192} - \frac{2187k_5}{6784} + \frac{11k_6}{84}\right) \tag{3.24}$$

The next step value y_{n+1} is calculated as

$$y_{n+1} = y_n + \frac{35k_1}{384} + \frac{500\,k_3}{1113} + \frac{125\,k_4}{192} - \frac{2187\,k_5}{6784} + \frac{11k_6}{84} \tag{3.25}$$

The ordinary differential equations encountered in the present analysis are solved by using numerical codes developed in MATLAB with the help of ‘ode45’ solver.

3.3.2. Adaptive Simpson’s Method

Adaptive Simpson’s method is a numerical integration method proposed by G.F. Kuncir in 1962. This method uses an estimate of the error obtained from calculating a definite integral using Simpson's rule. In this method the Simpson’s rule is used where the error is estimated and used to obtain precise solution. [102,103]

Using Simpson's rule over the sub-interval $[a,b]$ the value of the integral by Simpson's method

$$S_1[a,b] = \frac{b-a}{6}\left[f(a) + 4f\left(\frac{a+b}{2}\right) + f(b) \right] \tag{3.26}$$

Where, $f(x)$ is a real-valued function of a real variable, defined on a finite interval $a \le x \le b$

Error of the integral is given by $E_1 = -\frac{1}{90} h^5 f^4(\xi)$ (3.27)

where, $\xi \in (a,b)$ and $h = \frac{b-a}{2}$

Incorporating the error value, the modified value of the integral

$$I(f)[a,b] = S_1[a,b] + E_1[a,b] \tag{3.28}$$

A point c is taken as the midpoint of the interval $[a,b]$, i.e. $c = \frac{a+b}{2}$.

$$\begin{aligned} I(f)[a,b] &= I(f)[a,c] + I(f)[c,b] \\ &= S_1[a,c] + E_1[a,c] + S_1[c,b] + E_1[c,b] \\ &= S_2[a,b] + E_2[a,b] \end{aligned} \tag{3.29}$$

where, $S_2[a,b] = S_1[a,c] + S_1[c,b]$

and $E_2[a,b] = E_1[a,c] + E_1[c,b]$

$$= -\frac{1}{90}\left(\frac{h}{2}\right)^5 \left[f^4(\xi_1) + f^4(\xi_2) \right]$$

Since the sub-intervals $[a,c]$ $[c,b]$ are very small, ξ_1 and ξ_2 are very close. Hence $E_1[a,c] \approx E_1[c,b]$.

$$\begin{aligned} E_2[a,b] &= E_1[a,c] + E_1[c,b] \\ &\approx 2E_1[a,c] \\ &= \frac{1}{2}\frac{1}{2^5} E_1[a,b] \\ &= \frac{1}{16} E_1[a,b] \end{aligned} \tag{3.30}$$

Hence, $E_1[a,b] = 16E_2[a,b]$ (3.31)

Value of the integral $I(f) = S_1 + E_1 = S_2 + E_2$ (3.32)

From equation (3.31) and (3.32) we obtain,

$$S_2[a,b] - S_2[a,b] = E_1[a,b] - E_2[a,b]$$

$$=16E_2[a,b]-E_2[a,b]$$

$$=15E_2[a,b]` \tag{3.33}$$

Hence, $E_2[a,b]=\frac{S_2[a,b]-S_1[a,b]}{15}$ (3.34)

The result of the integral can be improved by using

$$I(f)=S_2+\frac{S_2-S_1}{15}. \tag{3.35}$$

If the error tolerance is ε,

The condition of the solution to be sufficiently accurate is

$|E_2|<\varepsilon$, i.e. $\frac{S_2-S_1}{15}<\varepsilon$

If the condition is not satisfied the interval is halved and the same procedure is repeated.

3.4. Undamped Free Vibration

The dynamic characteristics of the rough surface without any damping effect and excitation are analyzed first. The equation of motion can be obtained by setting the damping factor and the forcing amplitude to zero. Substituting $\zeta=0$ and $\hat{F}=0$ in equation (3.4) the following expression is obtained.

$$u''+\frac{1}{n}\left[(n+1)^n-1\right]=0 \tag{3.36}$$

Integrating equation (8) w.r.t non-dimensional time (τ)

$$\frac{n}{2}u'^2+\frac{1}{n+1}(u+1)^{n+1}-u=C_0 \tag{3.37}$$

where, C_0 is the constant of integration which can be calculated from the initial conditions. For the present analysis the initial conditions used are $u(\tau=0)=u_0$, $u'(\tau=0)=0$

The value of C_0 obtained from the above condition is

$$C_0=\frac{1}{n+1}(u_0+1)^{n+1}-u_0 \tag{3.38}$$

Putting the value of C_0 in equation (3.37),

$$u'=\sqrt{\frac{2}{n(n+1)}\left\{(u_0+1)^{n+1}-(u+1)^{n+1}+(u-u_0)(n+1)\right\}} \tag{3.39}$$

The natural time period τ_0 can be obtained by carrying out the integration

$$\tau_0 = 2\int_{u(\min)}^{u(\max)} \frac{du}{|u'|} \tag{3.40}$$

$$= 2\sqrt{\frac{n(n+1)}{2}} \int_{u(\min)}^{u(\max)} \frac{du}{\sqrt{(u_0+1)^{n+1} - (u+1)^{n+1} + (u-u_0)(n+1)}} \tag{3.41}$$

The normalized natural frequency is obtained as. $\Omega_0 = 2\pi / \tau_0$

As mentioned earlier, contact loss between the rough surface and the rigid flat occurs when $u < -1$. Hence, the minimum value of the initial displacement, $u(\min)$ is -1. Setting the value of u′ in equation (3.39) equal to zero, the maximum value of the initial displacement before contact loss is obtained as,

$$u(\max) = (n+1)^{1/n} - 1 \tag{3.42}$$

The evaluation of the integration shown in equation (3.41) is carried out numerically in MATLAB using adaptive Simpson quadrature method and the normalized natural frequency is obtained. From the equation (3.42) the values of the maximum initial displacement before contact loss $[n(\max)]$ for different combinations of fractal parameters (*D* and *G*) can be obtained, which are furnished with the corresponding nonlinearity exponent (*n*) values in the table 3.1.

Table 3.1. Values of maximum initial displacement before contact loss and corresponding nonlinearity exponent (*n*) for different combinations of fractal dimension (*D*) and fractal roughness (*G*) values.

Fractal Roughness (*G*)	**Fractal Dimension** (*D*)	**Nonlinearity exponent** (*n*)	**Maximum displacement for contact loss** [*u*(max)]
1.36×10^{-11} m	2.3	1.74723	0.7832
1.36×10^{-11} m	2.4	1.5372	0.8325
1.36×10^{-11} m	2.5	1.2719	0.9063
1.36×10^{-11} m	2.6	1.1421	0.9484
1.36×10^{-10} m	2.4	2.1092	0.7123
1.36×10^{-12} m	2.4	1.2934	0.8998
1.36×10^{-13} m	2.4	1.1638	0.9410

From table 3.1 it can be observed that, with increase of the roughness of the surface i.e. with surfaces having higher value of nonlinearity exponent (*n*), the maximum displacement value for which the contact loss occurs, decreases. Which means the tendency of contact loss of rough surface increases with increase in nonlinearity.

The variation of the non-dimensional natural frequency for the corresponding non-dimensional initial displacement ranging from the minimum to the maximum values for the variation of fractal dimension (*D*) and fractal roughness parameter (*G*) values are shown in Figure 3.4 and Figure 3.5 respectively.

As the magnitude of the initial displacement increases from the static equilibrium position *u* = 0, the value of natural frequency decreases. It can be observed that with higher nonlinearity, the rate of variation of natural frequency w.r.t initial amplitude becomes higher.

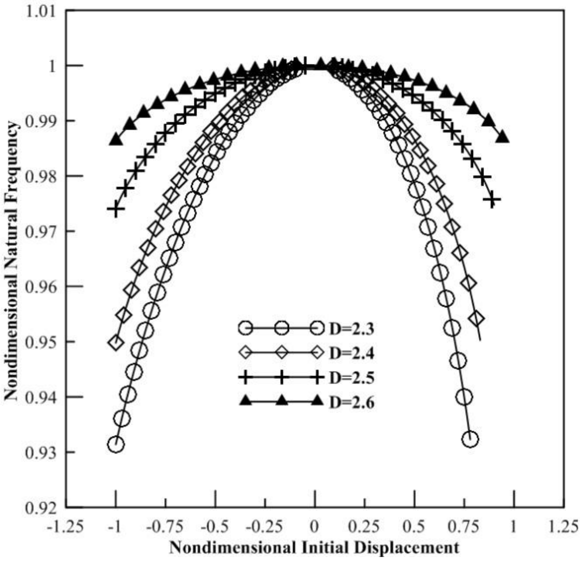

Figure 3.4. Plots of non-dimensional natural frequency vs. non-dimensional initial displacement of rough surfaces for varying fractal dimension (*D*).

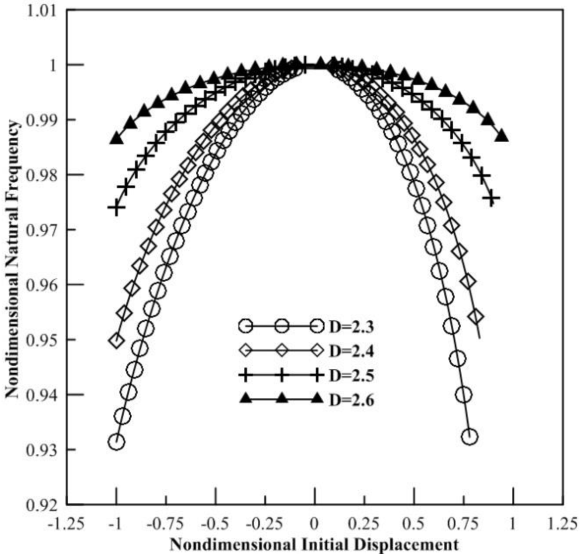

Figure 3.5. Plots of non-dimensional natural frequency vs. non-dimensional initial displacement of rough surfaces for varying fractal roughness (*G*).

For figure 3.4 the value of G is kept constant at 1.36×10^{-11} m and D is varied from 2.3 to 2.6 and for figure 3.5 the value of D is kept constant at 2.4 and G is varied from 1.36×10^{-13} m to 1.36×10^{-11} m. Now keeping the surface properties same (D=2.4, G=1.36×10^{-11} m), tangent modulus and yield strength of the surface are varied and the same analysis is repeated. Plots of non-dimensional natural frequency vs. initial displacement for variation of tangent modulus are put forward in Figure 3.6 and the results for the variation of yield strength are shown in Figure 3.7.

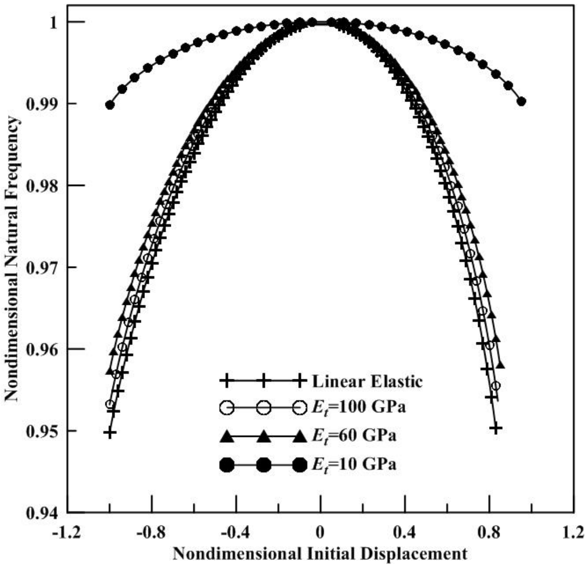

Figure 3.6. Plots of non-dimensional natural frequency vs. non-dimensional initial displacement of rough surfaces for varying tangent modulus (E_t).

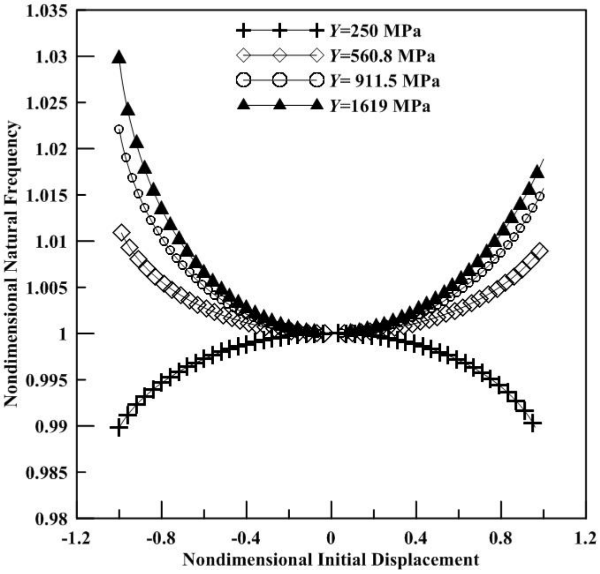

Figure 3.7. Plots of non-dimensional natural frequency vs. non-dimensional initial displacement of rough surfaces for varying yield strength (Y).

A significant change in the nature of the natural frequency-initial displacement curve is observed for the yield strength values 560.8 MPa, 911.5 MPa, and 1619 MPa. Here, the value of the nonlinearity exponent is found to be less than unity (the corresponding values are given in table 2.2 in previous chapter) and the nature of the initial displacement-natural frequency curves are vertically reversed as compared to the curves for nonlinearity exponent $n > 1$. Which means at the static equilibrium position of $u = 0$ non-dimensional natural frequency reaches its minimum value of $\Omega_0 = 1$ and increases with any change.

It has been mentioned previously that when nonlinearity exponent value is greater than unity, with higher nonlinearity, the rate of variation of natural frequency w.r.t initial amplitude becomes higher. The same condition is applicable when nonlinearity exponent value is less than unity.

From Figure 3.7, it can be inferred that the condition $n = 1$, serves as a limiting case, on two side of which the initial displacement-natural frequency behaviour is evidently different. For $n > 1$, the natural frequency decreases with increase in magnitude of initial displacement, whereas for $n < 1$, natural frequency increase with increase in magnitude of initial displacement. It is clear that the system natural frequency is dependent on the initial displacement, which is a typical nonlinear characteristic. Here it need to be mentioned that $n = 1$ corresponds to linear system behaviour (also confirmed by equation 3.1). For the sake of completeness, the system is also analyzed for $n = 1$ following the same procedure. The normalized natural frequency vs. initial displacement plot is shown in Figure 3.8 and quite clearly, the normalized natural frequency remains constant at $\Omega_0 = 1$ for all values of initial displacement.

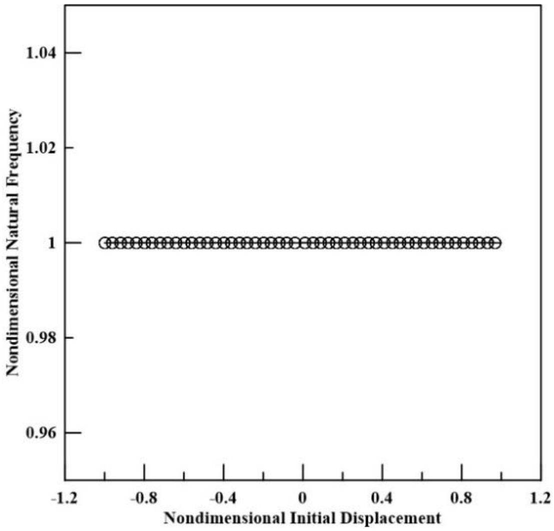

Figure 3.8. Non-dimensional natural frequency vs. non-dimensional initial displacement plot for linearly behaving contact system.

This behaviour is also in agreement with well-established knowledge of linear systems, where natural frequency is independent of initial condition.

3.5. Forced Damped Vibration

The vibration behaviour of the contacting surface under harmonic excitation has also been analyzed. Equation (3.5) is the equation of motion of the contacting surface under viscous damping and harmonic external excitation. The equation is solved numerically in MATLAB using numerical ordinary differential equation solver (ode45). The force damped dynamic characteristics of the system is represented by the normalized excitation frequency versus harmonic response amplitude plots i.e. frequency response curves. To visualize the effect of surface roughness on dynamic behaviour of rough surface, comparison of frequency response curves for different fractal dimension and fractal roughness are presented. The frequency response curves for the surfaces having fractal dimension D = 2.3 to 2.6 are presented in Figure 3.9 to 3.12. The value of fractal roughness (G) in these cases is kept fixed at 1.36×10^{-11} m. This is followed by frequency response curves for surfaces having fractal roughness (G) 1.36×10^{-13} m to 1.36×10^{-10} m. The corresponding fractal dimension is considered to be fixed at 2.4.

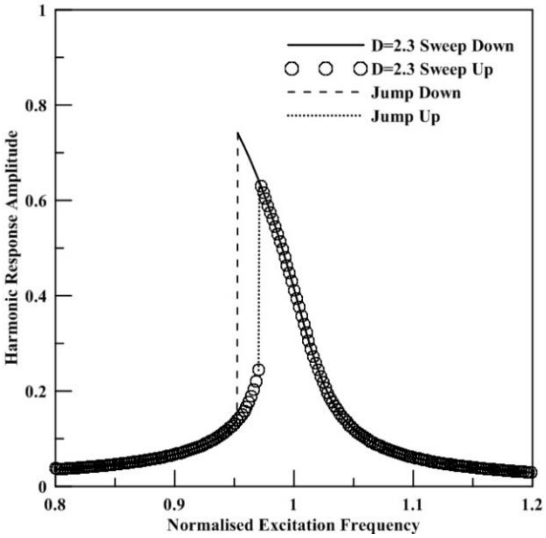

Figure 3.9. Frequency response curve for rough fractal surface with D = 2.3, G = 1.36×10^{-11} m.

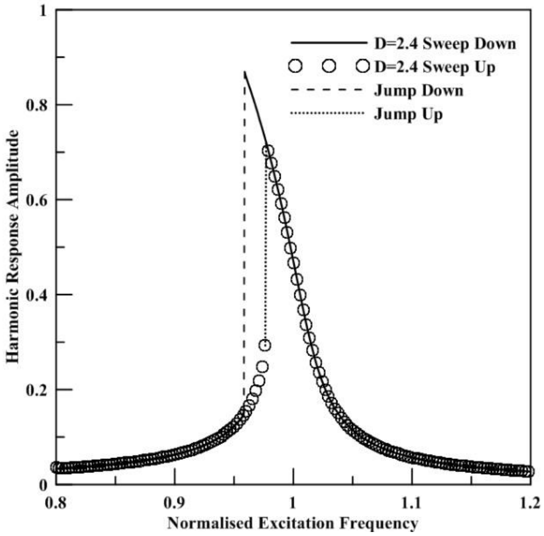

Figure 3.10. Frequency response curve for rough fractal surface with *D* = 2.4, *G* = 1.36×10^{-11} m.

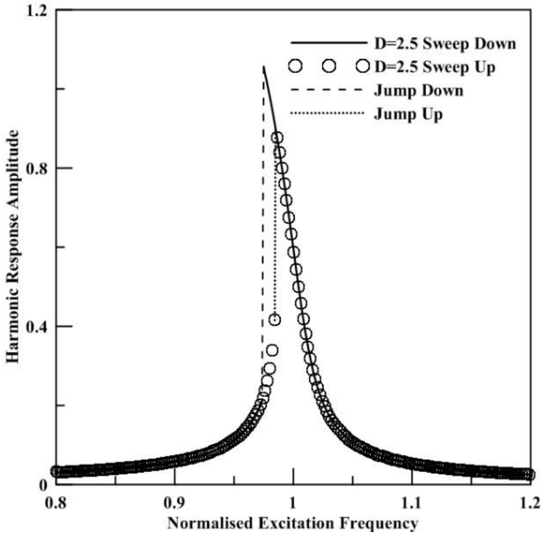

Figure 3.11. Frequency response curve for rough fractal surface with *D* = 2.5, *G* = 1.36×10^{-11} m.

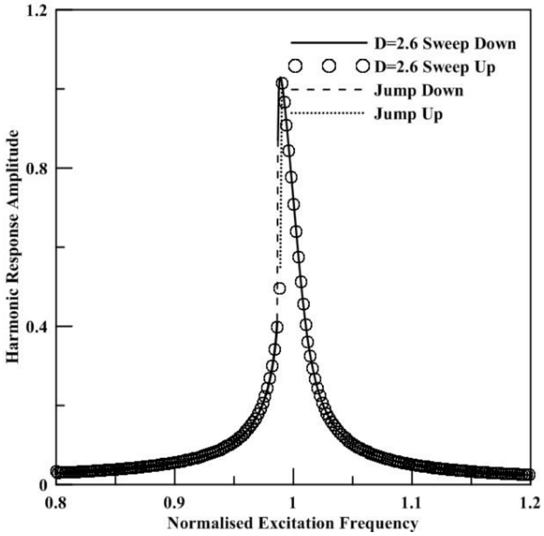

Figure 3.12. Frequency response curves for rough fractal surface with *D* = 2.6, *G* = 1.36×10^{-11}m.

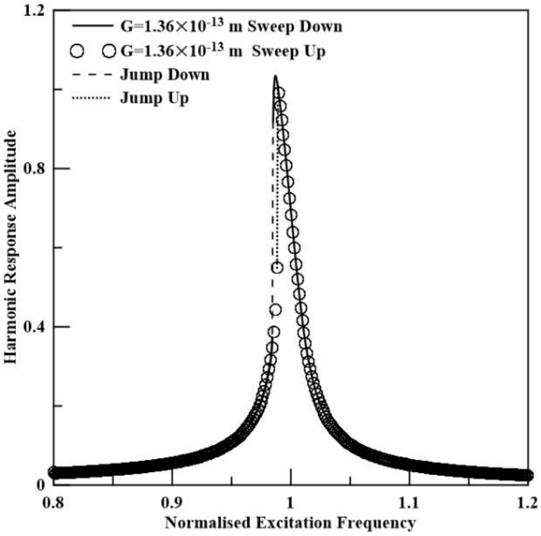

Figure 3.13. Frequency response curve for rough fractal surface with *D* = 2.4, *G* = 1.36×10^{-13} m.

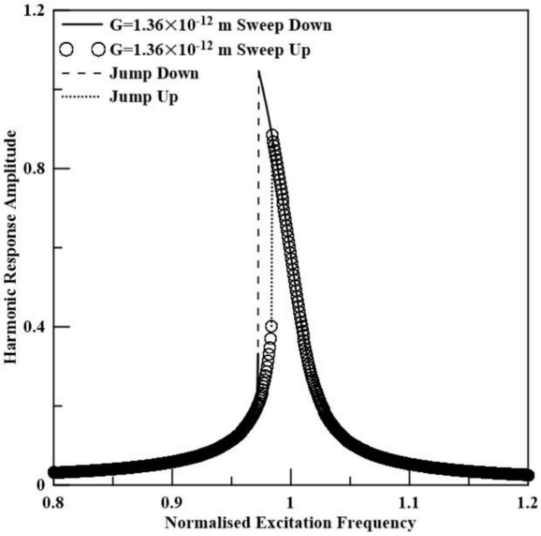

Figure 3.14. Frequency response curve for rough fractal surface with *D* = 2.4, *G* = 1.36×10^{-12} m.

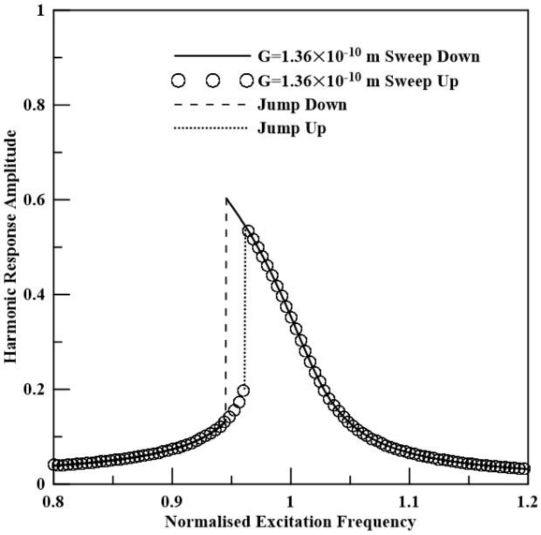

Figure 3.15. Frequency response curve for rough fractal surface with *D* = 2.4, *G* = 1.36×10^{-10} m.

It can be observed that for linearly elastic surface, the system exhibits softening nature, evident from tilting of the response curve towards the left of the vertical. This is also This is also consistent with the free vibration results, as softening nonlinearity s associated with decrease of natural frequency for increasing displacement. Rougher is the surface topography (indicated by lower values of *D* and higher values of *G*), higher is the nonlinearity exponent (*n*) and higher is the softening nature of the system.

To generate the frequency response curve, frequency sweep up and sweep down are performed. Sweep up involves starting with a small excitation frequency value and continuously increasing the excitation frequency in each step. On the other hand in sweep down, the excitation frequency is decreased from a finite value. While performing sweep up, jump up phenomenon has been observed (for softening type frequency response curve). Here, for a small increment of excitation frequency the response amplitude shows a substantial increase, hence, jumping to a higher value. Similarly for frequency sweep down, jump down phenomenon has been observed. In all the figures the location of jump up and jump down has been indicated by a dotted and dashed line respectively. These figures also demonstrates multi-response zone i.e. for a single excitation frequency value, two response amplitudes are obtained. However, theoretically a nonlinear system has three steady state solutions (of which two are stable and one unstable) for response amplitude at a given external excitation frequency. The present numerical method obtains the two stable solutions in forward and backward sweep but unable to capture the unstable solution.

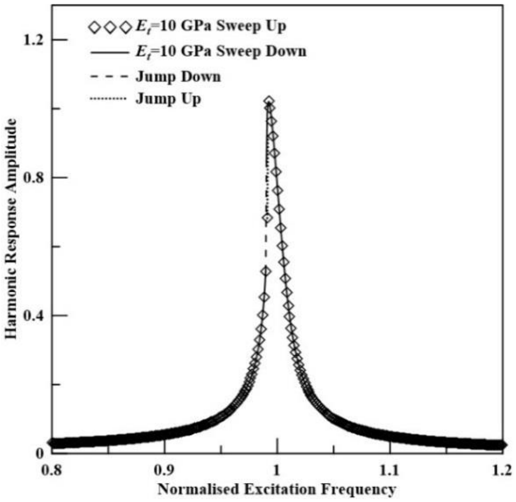

Figure 3.16. Frequency response curve for rough surface material with yield stress 250 MPa and tangent modulus 10 GPa.

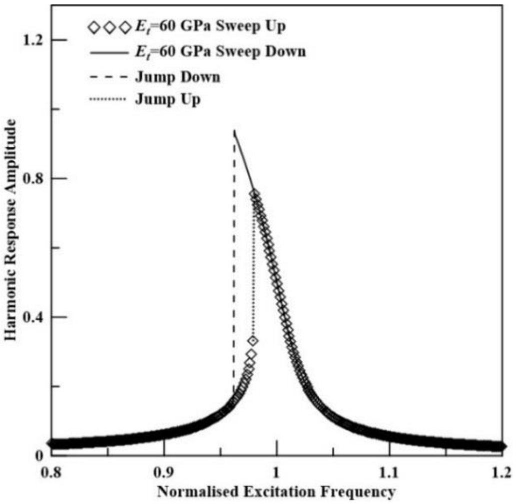

Figure 3.17. Frequency response curve for rough surface material with yield stress 250 MPa and tangent modulus 60 GPa.

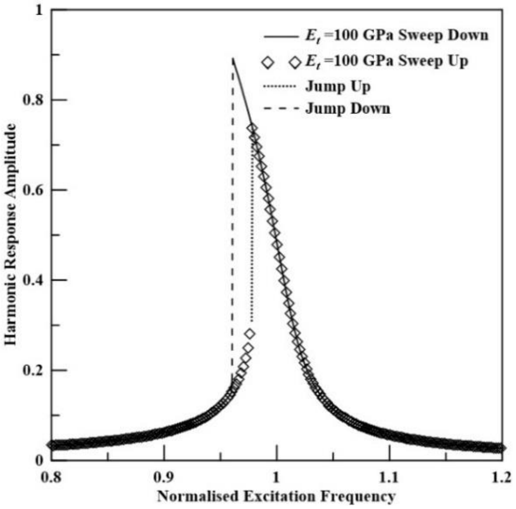

Figure 3.18. Frequency response curve for rough surface material with yield stress 250 MPa and tangent modulus 100 GPa.

The frequency response curves for the deformable surfaces having yield strength 250 MPa and varying tangent modulus values as 10 GPa, 60 GPa and 100 GPa are presented in Figure 3.16 to Figure 3.18. It can be observed that for higher tangent modulus, nonlinearity increases and the vibrating system tends to be more softening in nature.

Now, keeping the tangent modulus fixed at 10 GPa, the yield strength is varied. For the yield strength values of 560.8 MPa, 911.5 MPa, 1265.3 MPa and 1619 MPa the frequency response curves are shown in Figure 3.19 to Figure 3.22.

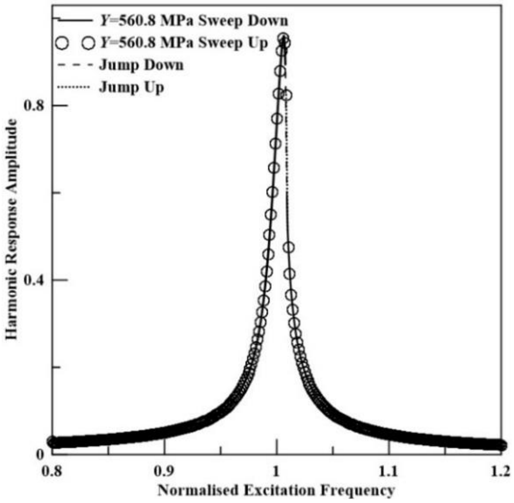

Figure 3.19. Frequency response curve for rough surface material with tangent modulus 10 GPa and yield stress 560.8 MPa.

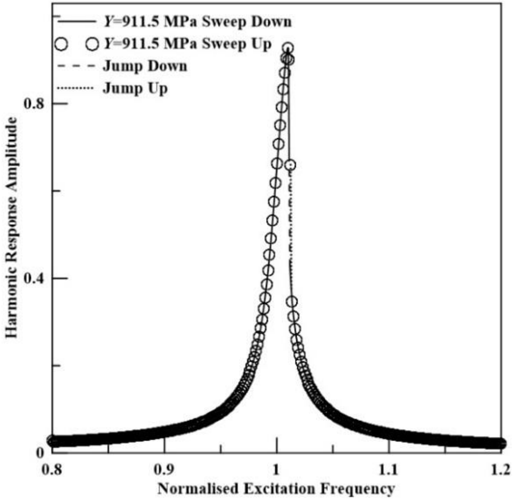

Figure 3.20. Frequency response curve for rough surface material with tangent modulus 10 GPa and yield stress 911.5 MPa.

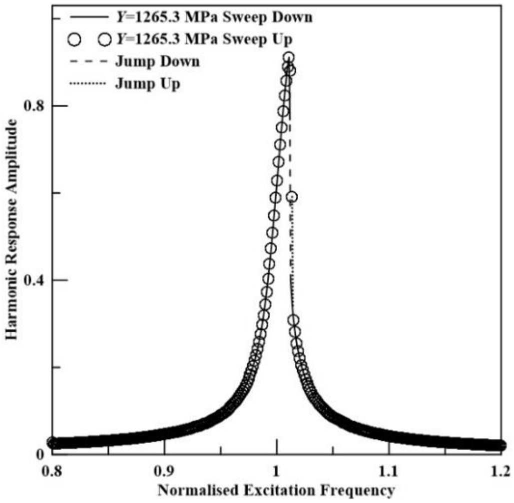

Figure 3.21. Frequency response curve for rough surface material with tangent modulus 10 GPa and yield stress 1265.3 MPa.

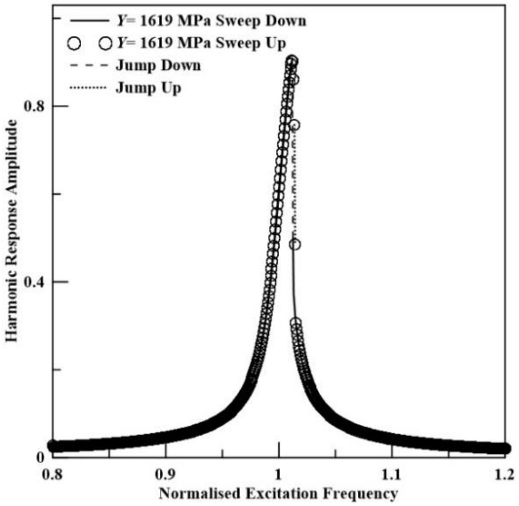

Figure 3.22. Frequency response curve for rough surface material with tangent modulus 10 GPa and yield stress 1619 MPa.

From the figures above it can be observed that for the yield strength values 560.8 MPa, 911.5 MPa, 1265.3 MPa and 1619 MPa, the frequency response are hardening in nature since the nonlinearity exponent values are less than unity. For the hardening type of frequency response curves, jump down phenomenon has been observed while performing sweep up, and while frequency sweep down, jump up phenomenon has been observed. For higher yield strength value, the hardening nature of the system increases with higher nonlinearity.

3.5.1. Superharmonic Response

A nonlinear system is capable of showing response at excitation frequency different from the system's linear natural frequency. A superharmonic response exists when the excitation frequency is a fraction of the linear natural frequency. From the normalized equation of motion of the forced damped system [equation (3.5)] it was noted that the value of the normalized natural frequency is unity. The current system exhibits superharmonic response at normalized excitation frequency value $0.5\,(\omega_n / 2)$. Figure 3.23 shows the frequency response curve of the system with n = 2.0. It can be seen that there exists a small response at normalized excitation frequency of 0.5. A magnified view of the same response is also shown in the figure.

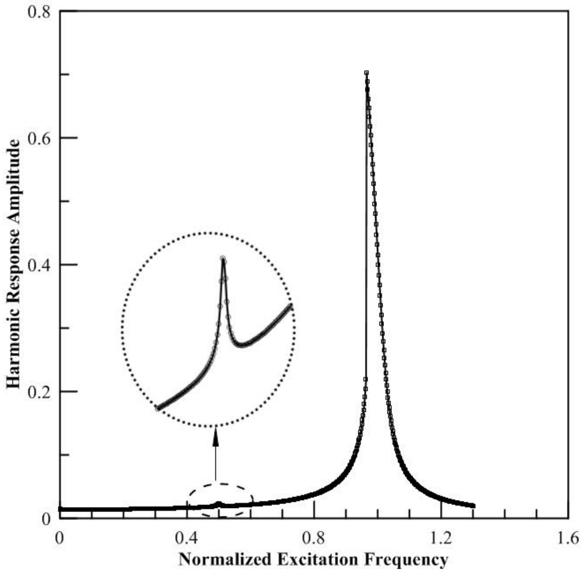

Figure 3.23. Superharmonic response for the system corresponding to n = 2.0.

3.5.2. Phase and Time-Displacement Plot Analysis

Keeping the normalized initial displacement at 0.5, phase plots and time-displacement plots are obtained from the numerical solution of equation (3.5). The plots (in non-dimensional plane) for varying nonlinearity exponent (n) from 0.6 to 2.0 are presented from Figure 3.24 to Figure 3.27 to obtain a qualitative relationship of displacement and velocity of the dynamic contact system with the nonlinearity exponent (n).

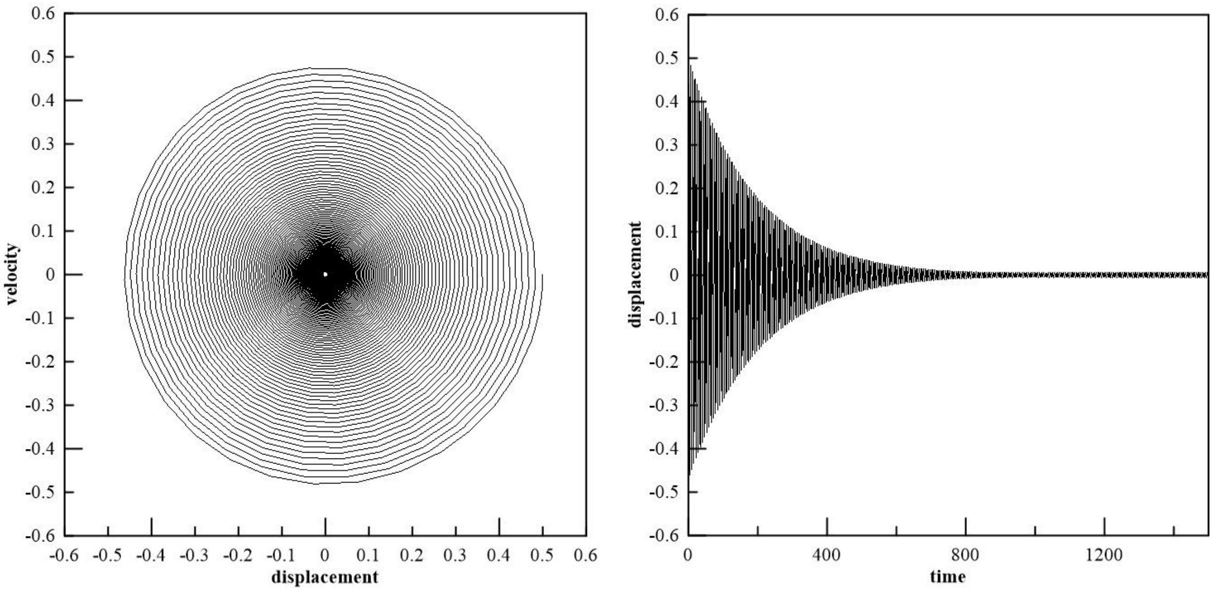

(a) (b)

Figure 3.24. (a) Phase plot and (b) time-displacement plot of vibrating rough surface with n = 0.6 for normalized initial displacement as 0.5.

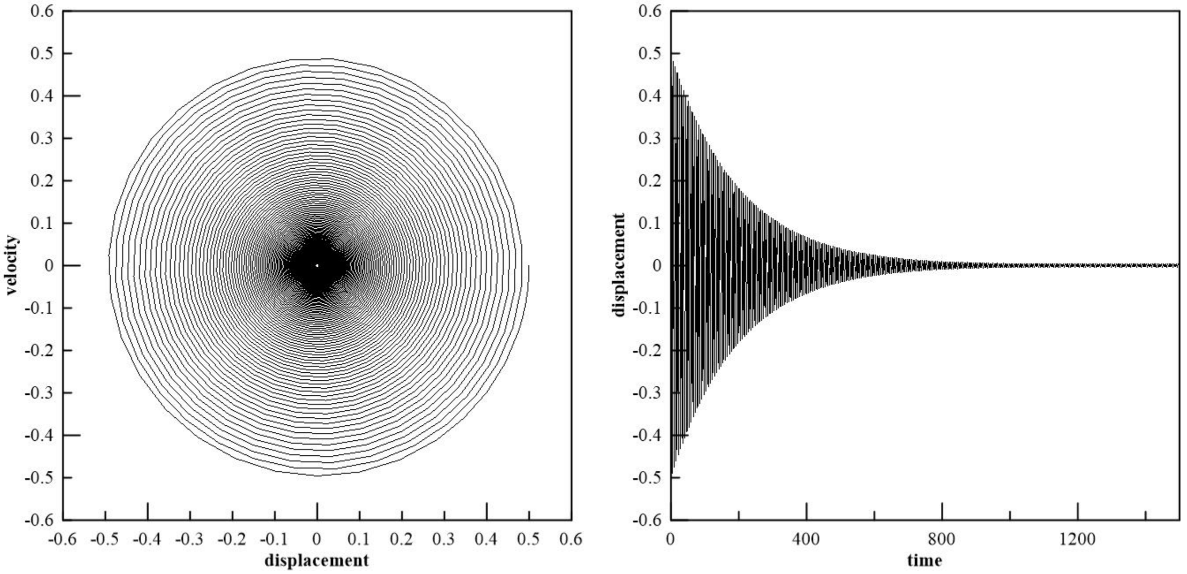

(a) (b)

Figure 3.25. (a) Phase plot and (b) time-displacement plot of vibrating rough surface with n = 1.0 for normalized initial displacement as 0.5.

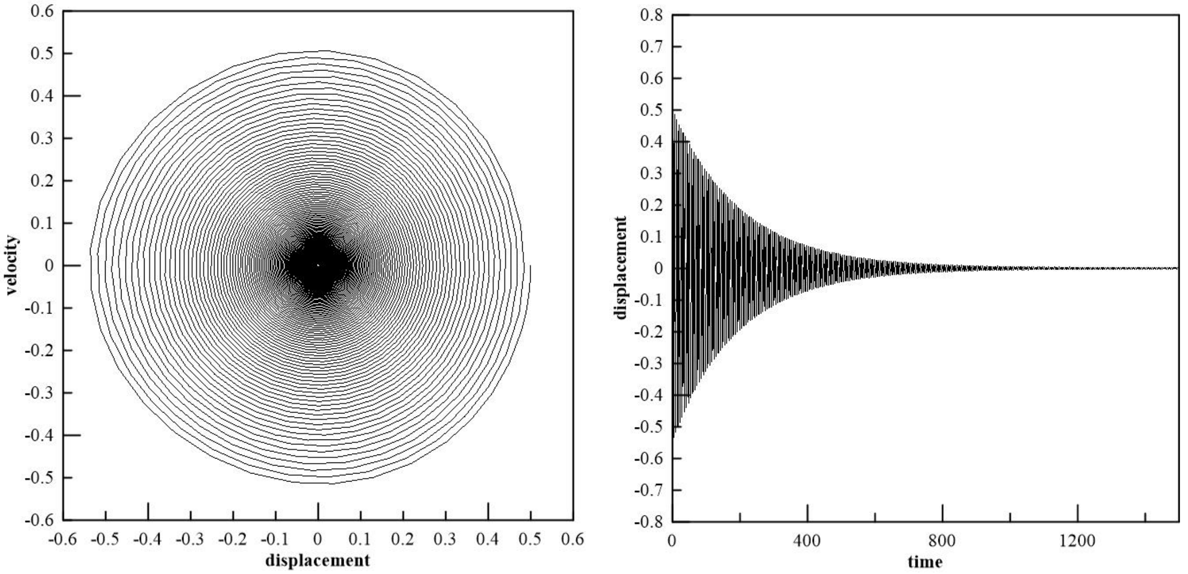

(a) (b)

Figure 3.26. (a) Phase plot and (b) time-displacement plot of vibrating rough surface with n = 1.5 for normalized initial displacement as 0.5.

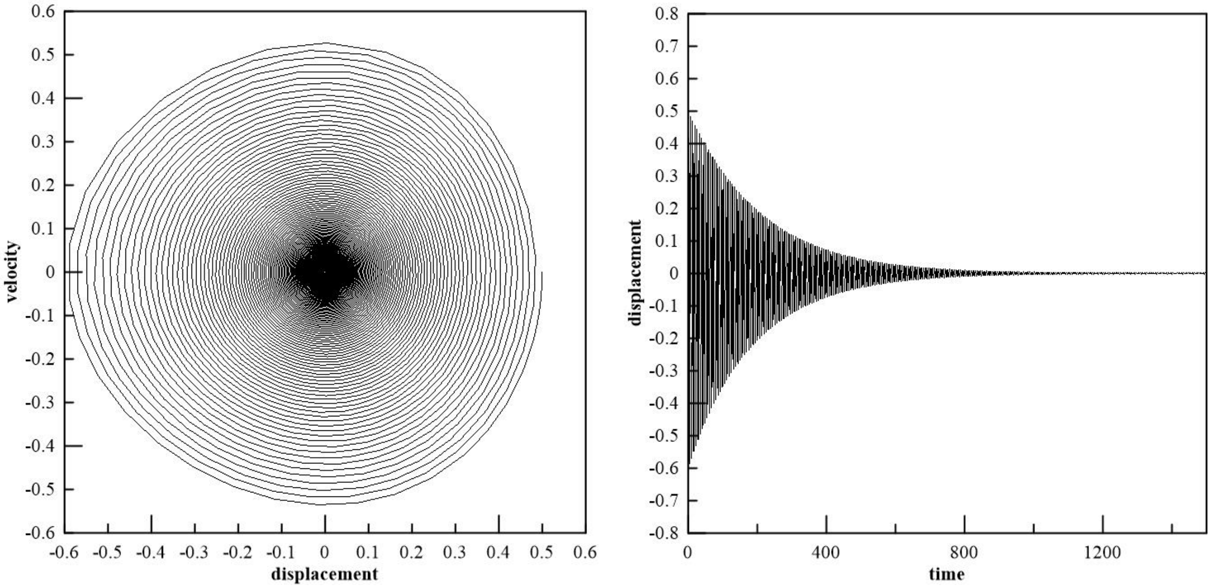

(a) (b)

Figure 3.27. (a) Phase plot and (b) time-displacement plot of vibrating rough surface with *n* = 2.0 for normalized initial displacement as 0.5.

Detailed discussion on the phase plot and time-displacement plot are provided in the next chapter (chapter 4) in which the nature is found to be similar with the present model.

3.6. Summary

In the current chapter, vibration of a rough deformable surface in contact with a rigid flat is modelled by the dynamics of a single degree of freedom spring-mass-damper system. Static force-displacement relationship of the rough surface is used to determine the dynamic characteristics of the surface for free as well as for forced damped vibration. For free undamped vibration analysis contact loss is taken into account and the variation of normalized natural frequency w.r.t. initial displacement is presented for different surface and material properties. In case of forced damped vibration, the dynamic characteristics are presented in the form of frequency response curves. It is found out that for linearly elastic surface, the system is found to be softening in nature and the softening nature increases with the increase of roughness of the surface. Similarly, the softening nature increases with increase in tangent modulus for elastic-plastic contact. While analyzing the effect of yield strength value of the rough surface material, it is found that above a certain value of yield strength the nature of the frequency response curve changes from softening to hardening in nature. Superharmonic response is also observed for the vibrating contact system.

Chapter 4

Dynamic Analysis of Rough Fractal Surface: Model II

The chapter provides an analysis on the dynamic properties of deformable rough fractal surface in contact with harmonically excited rigid flat surface and also the effect of surface roughness and material properties on it.

4.1. Introduction

The objective of the present thesis is to analyse the dynamic characteristics of contact between a rough deformable surface and a rigid flat. In the previous chapter a representative single degree of freedom (SDOF) model is devised where excitation in terms of a harmonic force is applied to the mass. The present chapter introduces a similar method, but here the excitation is imparted in the form of harmonic excitation to the base. It is assumed that with movement of the rigid flat, multiple asperities of the rough surface are pressed and deformed and as a result the rough surface vibrates under the influence of the rigid flat. A figure representing the physical system has been shown is Figure 3.1 and replicated in Figure 4.1(a) for ready reference. It is presumed that the suggested model would successfully capture the dynamic behaviour of the system.

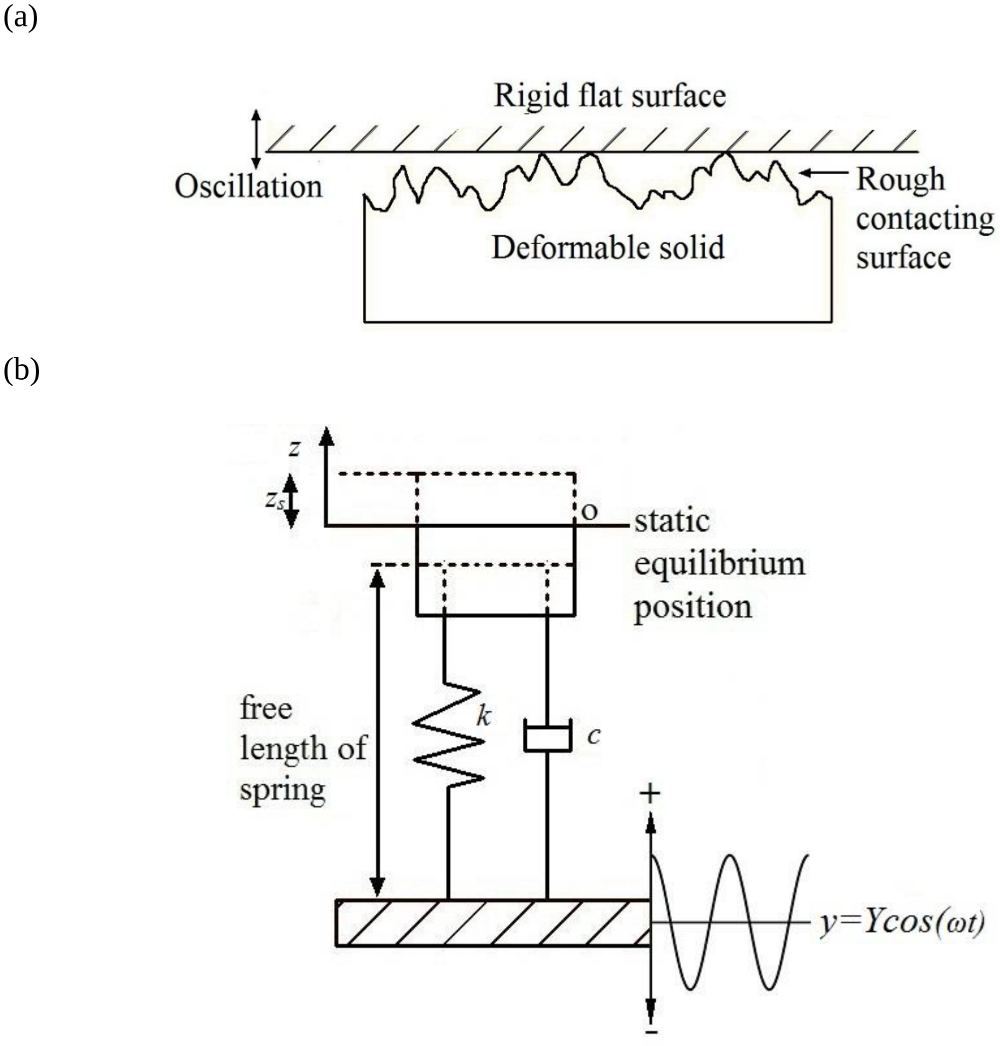

Figure 4.1. (a) Deformable rough surface in contact with rigid flat surface and (b) SDOF dynamic model representation

4.2. Dynamic Model

The dynamic contact system is modelled as a vertical single degree of freedom (SDOF) spring-mass-damper system in which the harmonic excitation is imparted in form of external displacement function on the base the spring-mass-damper is resting on. Hence the dynamics of the system is dependent on the relative motion of the block and the movable base.

Similar to the previous model, the mass block is considered to be equivalent to the deformable body in terms of mass, i.e., the block has the same mass as that of the rough solid (*m*). The spring stiffness is taken as the bulk stiffness of the surface (*k*). The load-displacement behaviour of the contact interface as obtained from the FE analysis of chapter 2 is imposed on the spring as its response under loading. As the load-displacement characteristic is nonlinear in nature, the restoring force of the system becomes a nonlinear function of spring deformation. The damper is considered to be linear and viscous with linear damping co-efficient *c*, same as the previous model. Due to the weight of the block, the spring undergoes a deflection of z_s. The static deflection of the spring (z_s) is given by

$$z_s = (mg / k)^{1/n} \tag{4.1}$$

The deflected position of the block due to its weight is considered as the static equilibrium position around which the mass vibrates under the influence of the externally excited base and $z(t)$ indicates the displacement of the system with respect to the equilibrium. The force-displacement relationship of the spring is taken as

$$F_s = k(z + z_s)^n \tag{4.2}$$

Where F_s denotes the restoring force, *k* is the nonlinear stiffness of the spring and *n* is the nonlinearity exponent. The parameters *k* and *n* are obtained from the results of FE analysis from chapter 2. External harmonic excitation is applied as displacement on the base that the spring-mass-damper system is resting on. The mathematical form of the harmonic excitation is given as,

$$y = Y \cos(\omega t) \tag{4.3}$$

Hence $\dot{y} = Y\omega \sin(\omega t)$ (4.4)

where, $y(t)$ denotes the displacement of the base. Y and ω are the excitation amplitude and frequency respectively. Considering the relative motions between the mass and the base, the governing equation of the system can be written as,

$$m\ddot{z} + c(\dot{z} - \dot{y}) + k\,[(z + z_s)^n - y^n] - mg = 0 \tag{4.5}$$

Putting the values of y and $\dot{y}$ from equation (4.3) and (4.4), the final form of the equation of motion is obtained.

$$m\ddot{z} + c\dot{z} + k\left(z + z_z\right)^n - mg = k\left[Y\cos\ (\omega t)\right]^n + c\omega Y\sin\ (\omega t) \tag{4.6}$$

To generalize the equation of motion for multiple domains it is converted into a normalized equation of motion by introducing few non-dimensional parameters.

$$u = \frac{z}{z_s},\ \Omega = \frac{\omega}{\omega_s},\ \tau = \omega_s\, t,\ \zeta = \frac{c}{2m\omega_s} \text{ and } Z = \frac{Y}{z_s}$$

The parameter ω_s used for normalization is the natural frequency at the static equilibrium position $\left(\omega_s = \sqrt{\frac{nkz_s^{n-1}}{m}}\right)$. $u, \Omega,\ \tau, Z$ and ζ are normalized displacement, frequency, time, excitation amplitude and damping coefficient respectively. After normalization `the dimensionless equation of motion becomes

$$u'' + 2\zeta u' + \frac{1}{n}\left[(n+1)^n - 1\right] = \frac{1}{n} Z^n \cos^n(\Omega\tau) + 2\zeta Z\Omega\sin(\Omega\tau) \tag{4.7}$$

where, $'$ denotes differentiation w.r.t. non-dimensional time. The expression $(u+1)^n$ is expanded into a third order Taylor series expansion and hence the following equation is obtained.

$$u'' + 2\zeta u' + u + \alpha_2 u^2 + \alpha_3 u^3 = \frac{1}{n} Z^n \cos^n(\Omega\tau) + 2\zeta Z\Omega\sin(\Omega\tau) \tag{4.8}$$

where, $\alpha_2 = \frac{(n-1)}{2}$ and $\alpha_3 = \frac{(n-1)(n-2)}{6}$.

The governing differential equation describes linearly damped forced vibration of the rough surface in contact with a harmonically excited rigid flat surface. Since the restoring force part of the left hand side of equation (4.8) contains a quadratic and a cubic term in *u*, it can be classified as a Duffing-Helmholtz type equation with natural frequency (ω_n) value of unity. The above mentioned equation is solved numerically using ODE solver (ode45) of MATLAB to obtain dynamic characteristics of the vibrating rough surface.

If the harmonic excitation to the base is reduced to zero (i.e. $Z = 0$), the problem becomes a linearly damped nonlinear free vibration problem. In this scenario, the governing differential equation of the system is given by

$$u'' + 2\zeta u' + u + \alpha_2 u^2 + \alpha_3 u^3 = 0 \tag{4.9}$$

Here, in absence of base excitation the RHS is reduced to zero. Further simplification can be considered by neglecting damping and taking $\zeta = 0$. This scenario represents a nonlinear free vibration situation governed by the following equation. This situation was analysed in the section 3.3 in Chapter 3.

$$u'' + u + \alpha_2 u^2 + \alpha_3 u^3 = 0 \tag{4.10}$$

4.3. Dynamic Analysis and Results

Frequency response curve is an effective way to represent dynamic behaviour of a system. It plots the response amplitude for the variation of excitation frequency which depicts the nature of the vibration of the system, whether it is hardening or softening in nature. The comparison of the frequency response curves for the surfaces with $G = 1.36\times10^{-13}$ m and fractal dimension (D) varying from 2.3 to 2.6 are presented in Figure 4.2 and 4.3. In Figure 4.2, frequency response curves for D values 2.4, 2.5 and 2.6 (corresponding 'n' values 1.5372, 1.2719, 1.1421 respectively) are plotted for the level of excitation of $Z = 0.0198$, while in Figure 4.3 frequency response curves for D values 2.3 and 2.4 (corresponding 'n' values 1.74723, 1.5372 respectively) are presented for higher excitation amplitude $Z = 0.036$.

It can be observed from the figures that for same excitation amplitude, with increase of the nonlinearity exponent value (n), the level of response amplitude decreases drastically. In the previous model as well, the same nature of decrement of response amplitude was observed. But since the parameter 'n' appears as an exponent in the equation of motion of the present model [equation (4.8)], the effect of the parameter 'n' is much pronounced.

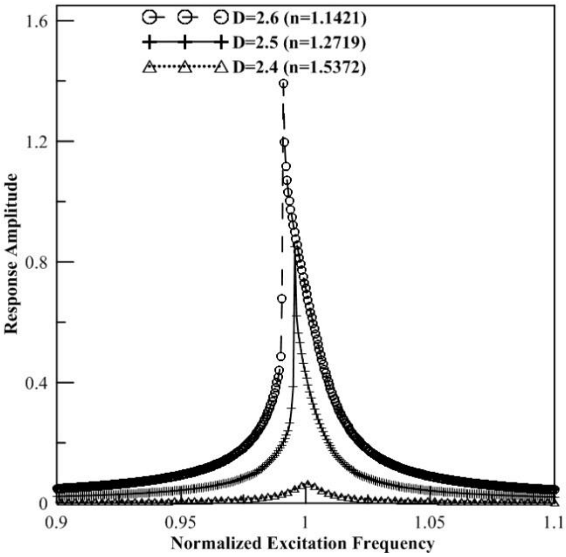

Figure 4.2. Comparison between frequency response curves for surfaces having D values 2.4, 2.5 and 2.6 for Z = 0.0198.

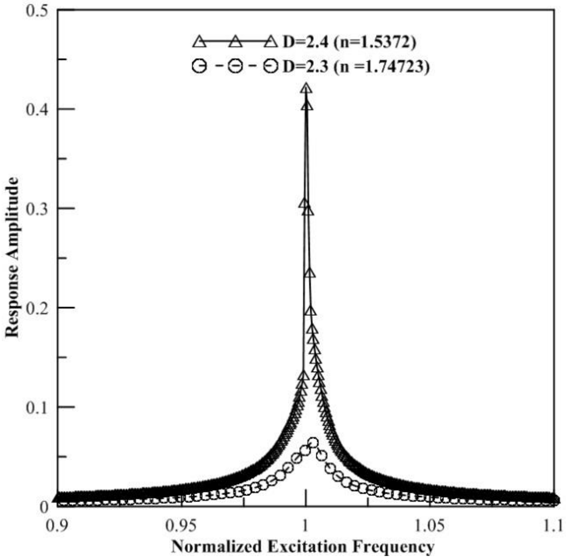

Figure 4.3. Comparison between frequency response curves for surfaces having D values 2.4 and 2.3 for *Z* = 0.036.

Similarly the comparison of the frequency response curves for the surfaces with $D = 2.4$ and *G* varying from 1.36×10^{-11} m to 1.36×10^{-13} m are presented in Figure 4.4. The amplitude of excitation is taken as *Z* = 0.0192.

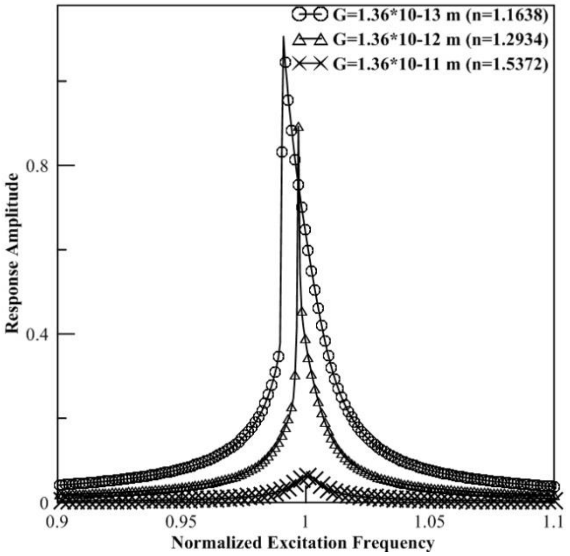

Figure 4.4. Comparison between frequency response curves for surfaces having *G* values varying from 1.36×10^{-11} m to 1.36×10^{-13} m for $Z = 0.0192$.

Here, it can be observed from the figures that with rougher surface topography (higher *G* and lower *D* value) the response amplitude of the contacting system decreases for same level of excitation.

Now, keeping the surface parameters constant at $G = 1.36\times10^{-11}$ m and $D = 2.4$ material properties (tangent modulus and yield strength) are varied. Frequency response curves for the deformable surfaces having yield strength 250 MPa with varying tangent modulus values as 10, 60 and 100 GPa are presented in Figure 4.5, whereas surfaces with tangent modulus fixed at 10 GPa with varying yield strength values as 560.8 MPa, 911.5 MPa, 1265.3 MPa and 1619 MPa are furnished in Figure 4.6.

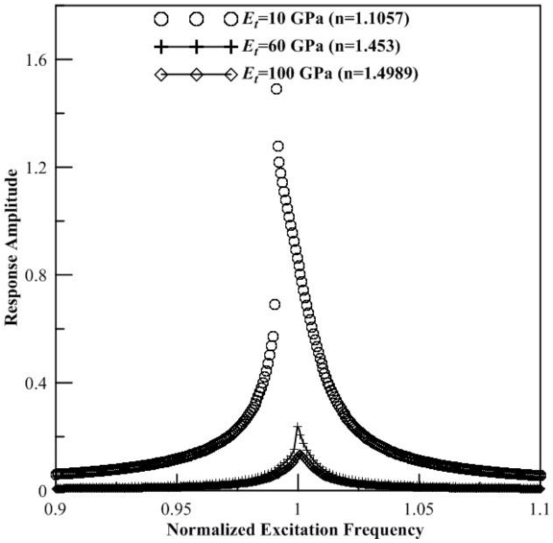

Figure 4.5. Frequency response curves for rough surface material with yield stress 250 MPa and varying tangent modulus 10, 60 and 100 GPa for $Z = 0.02$.

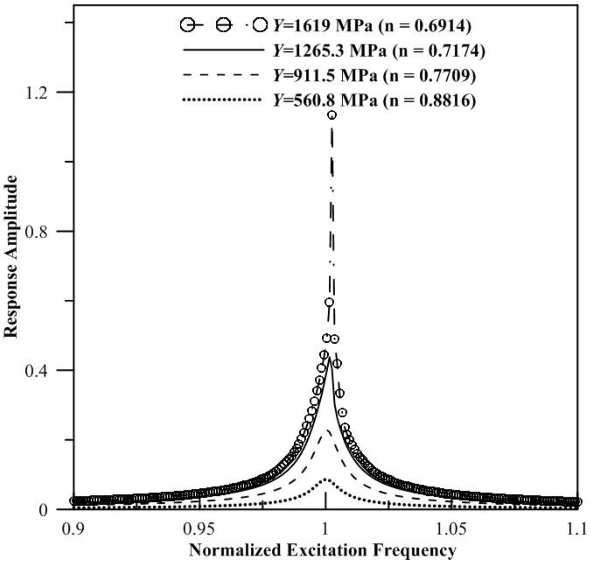

Figure 4.6. Frequency response curves for rough surface material with tangent modulus 10 GPa and varying yield strength 560.8 MPa, 911.5 MPa, 1265.3 MPa and 1619 MPa for $Z = 0.000295$.

It was observed from the figures 4.5 and 4.6 that for same excitation amplitude, lower tangent modulus (E_t) and higher yield strength (Y) value results in higher response amplitude.

When it comes to the nature of the frequency response i.e. whether the system is of softening or hardening type it can be observed that for the value of nonlinearity exponent (n) less than unity, the system is found to be hardening in nature and softening for nonlinearity exponent value greater than unity as indicated by Figure 4.7. For each case, jump up and jump down phenomenon has been shown in the plot.

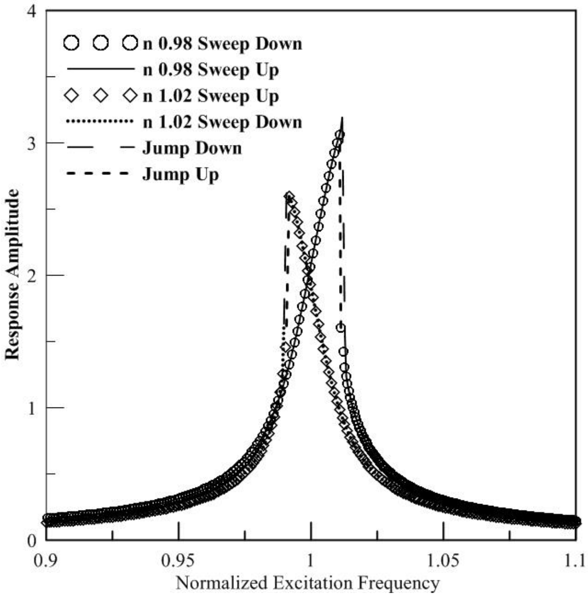

Figure 4.7. Comparison of frequency response curves with n values 0.98 and 1.02 for $Z = 0.028$.

4.3.1. Superharmonic Response

For the present system, amplitude peaks are observed at excitation frequency values $\omega_n/2$, $\omega_n/3$ etc. i.e. the system exhibits superharmonic responses. In Figure 4.8 to 4.13 superharmonic response is shown for the variation of the nonlinearity exponent (n) from 1.2 to 2.1 keeping the excitation amplitude fixed at $Z = 0.02$. It is seen that superharmonic response can be noted at normalized excitation frequency values of $0.5(\omega_n/2)$, $0.33(\omega_n/3)$, and $0.25(\omega_n/4)$. In Figure 4.14 the magnified view of the responses inside the rectangle of Figure 4.10 shows the superharmonic responses at frequencies $\omega_n/3$, $\omega_n/4$, $\omega_n/5$, $\omega_n/6$ and so on. For the increase of the nonlinearity exponent, as previously mentioned, the response amplitude decreases at natural frequency as well as at superharmonic frequencies. Interestingly, it is found that for each step of the increase of the n value, the decrement of response amplitude at the natural frequency (ω_n) is higher than the decrement at $\omega_n / 2$. Hence, at a certain point (*n* = 1.8) the amplitude at $(\omega_n / 2)$ is found to be higher than at the natural frequency value (ω_n) (Figure 4.11).

Beyond another certain value of *n*, another significant phenomenon is observed, where the amplitude at the natural frequency becomes fixed and does not change with increase of the nonlinearity exponent (Figure 4.11, 4.12 and 4.13) Also it has been observed that the value of the amplitude it gets fixed at, depends upon the excitation amplitude and increases when the later increases.

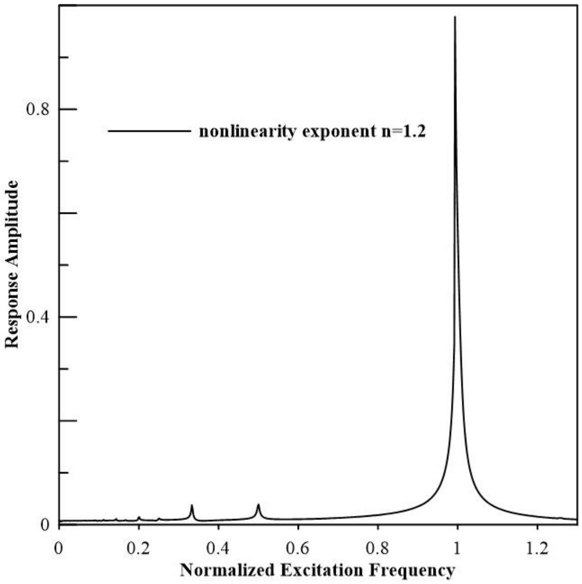

Figure 4.8. Superharmonic response for nonlinearity exponent value 1.2.

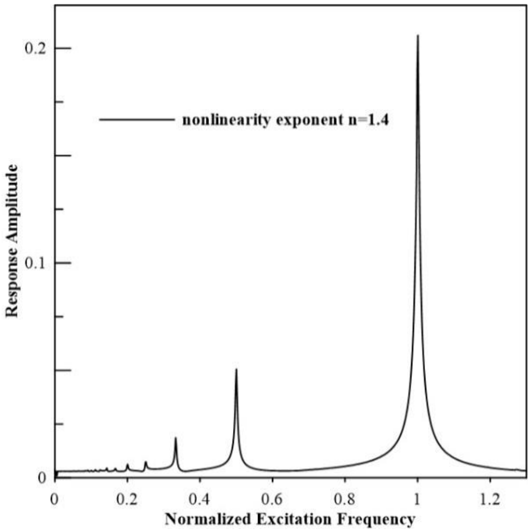

Figure 4.9. Superharmonic response for nonlinearity exponent value 1.4.

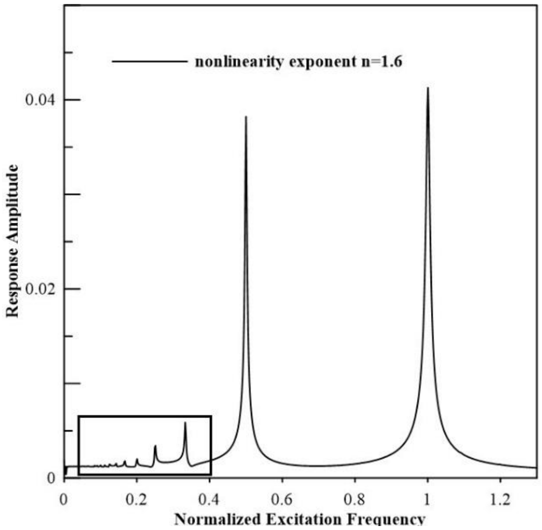

Figure 4.10. Superharmonic response for nonlinearity exponent value 1.6.

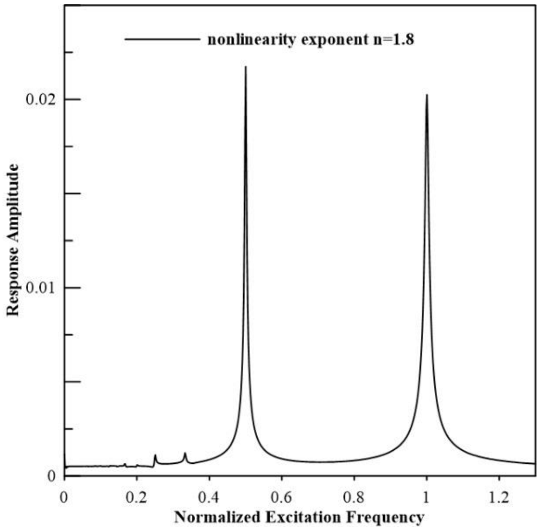

Figure 4.11. Superharmonic response for nonlinearity exponent value 1.8.

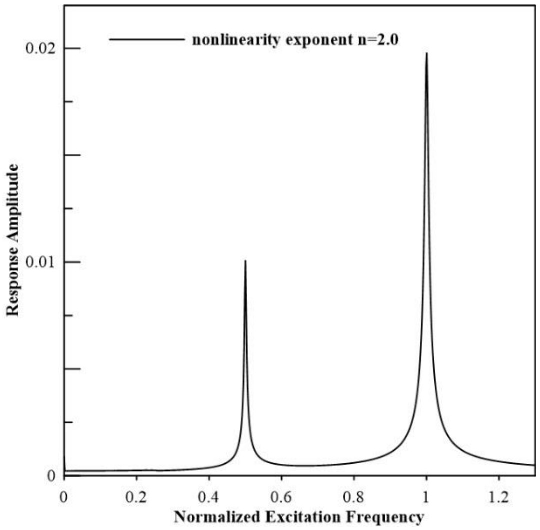

Figure 4.12. Superharmonic response for nonlinearity exponent value 2.0.

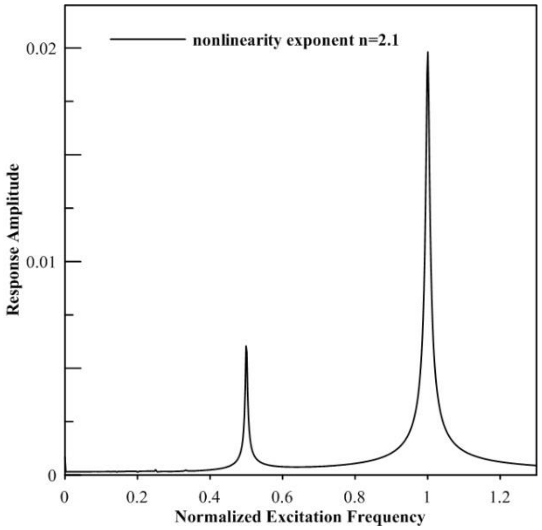

Figure 4.13. Superharmonic response for nonlinearity exponent value 2.1.

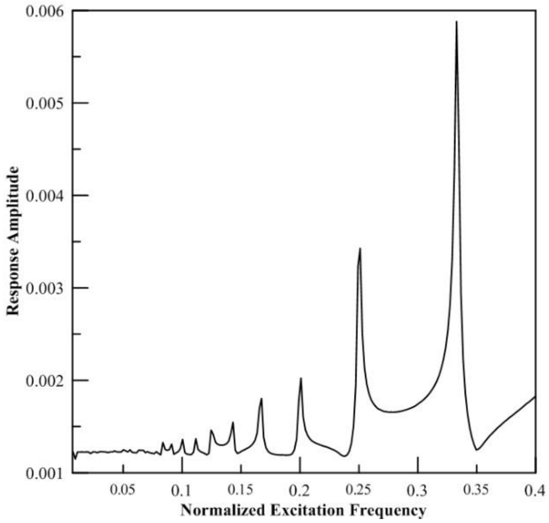

Figure 4.14. Magnified view of the superharmonic responses for nonlinearity exponent (*n*) 1.6.

4.3.2. Phase and Time-Displacement Plot Analysis

From the numerical solution of the equation of motion of the current contacting system [equation (4.8)] phase plots and time-displacement plots (in non-dimensional plane) are obtained. The normalized initial displacement is set as 0.5. The corresponding phase plot and the time-displacement plots for the systems with nonlinearity exponent (*n*) values 0.6, 1.0, 1.5 and 2.0 are presented in Figure 4.15 to 4.18. Now, setting the normalized initial displacement as -0.5, phase plot and time-displacement plots for the systems with nonlinearity exponent (*n*) values 0.6 and 2.0 are furnished in Figure 4.19 and 4.20.

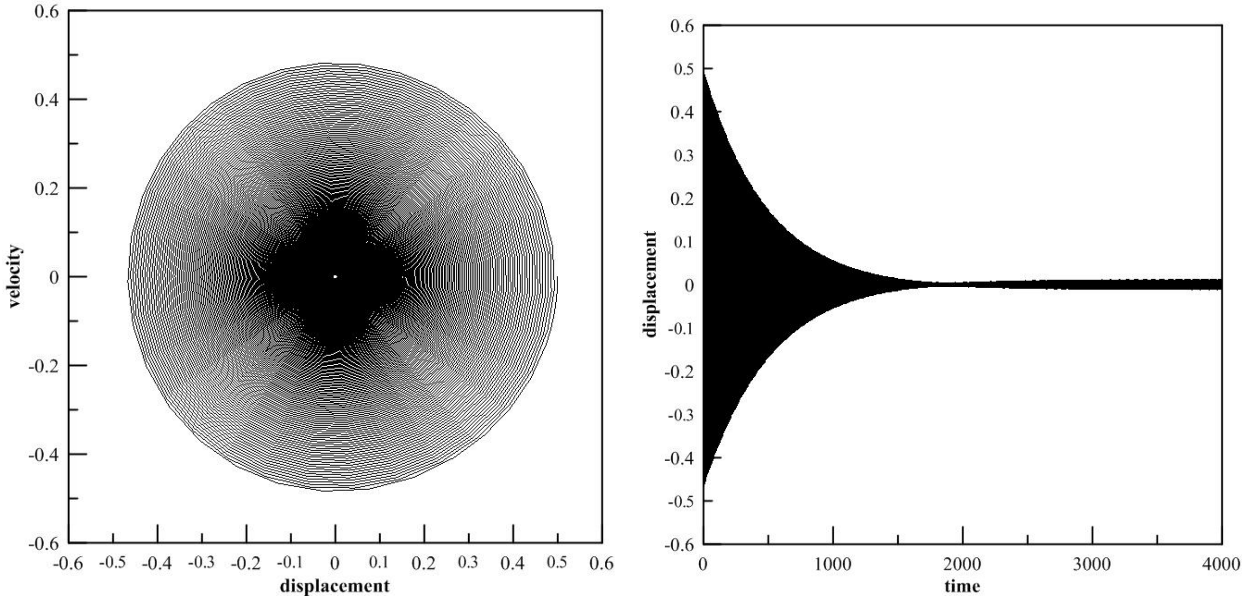

(a) (b)

Figure 4.15. (a) Phase plot and (b) time-displacement plot of vibrating rough surface with *n* = 0.6 for normalized initial displacement as 0.5.

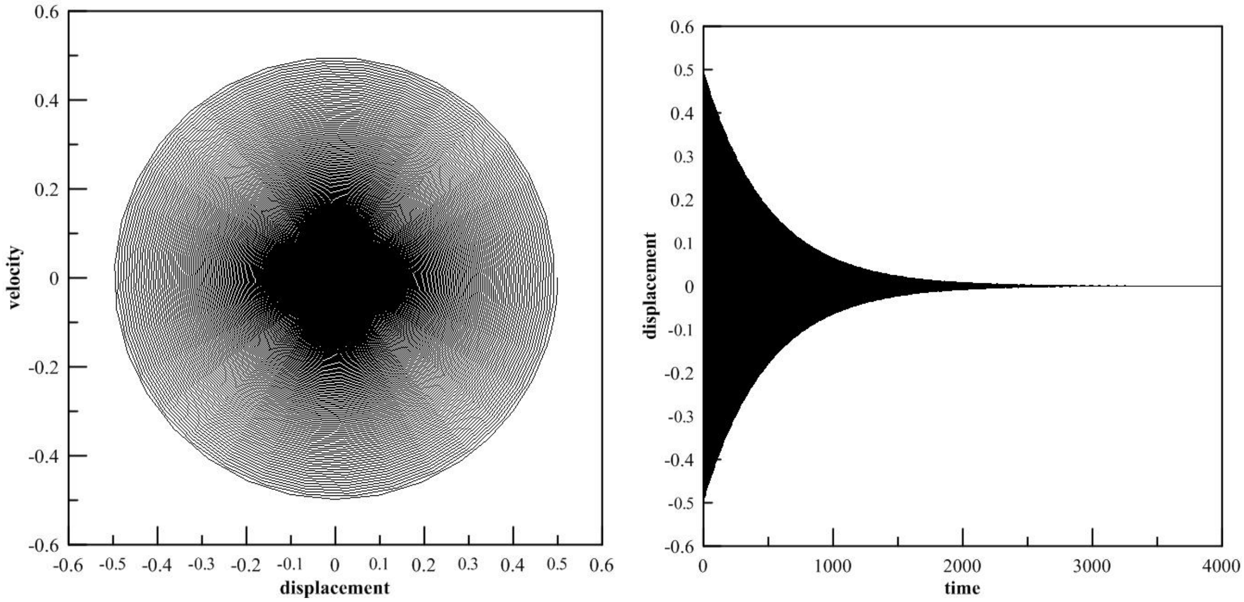

Figure 4.16. (a) Phase plot and (b) time-displacement plot of vibrating rough surface with *n* = 1.0 for normalized initial displacement as 0.5.

(a) (b)

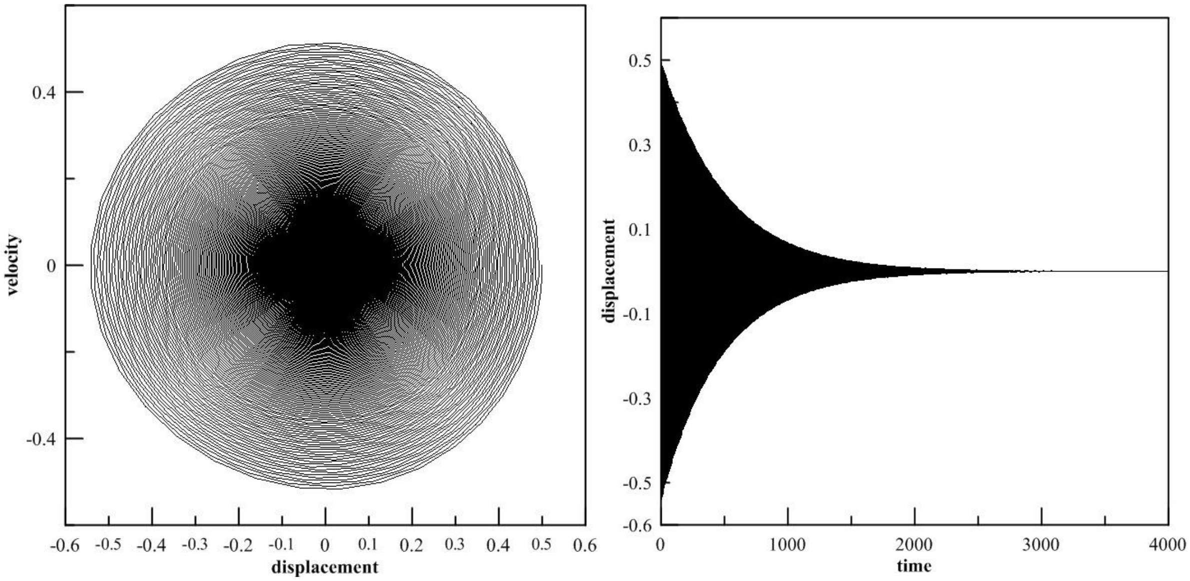

(a) (b)

Figure 4.17. (a) Phase plot and (b) time-displacement plot of vibrating rough surface with n = 1.5 for normalized initial displacement as 0.5.

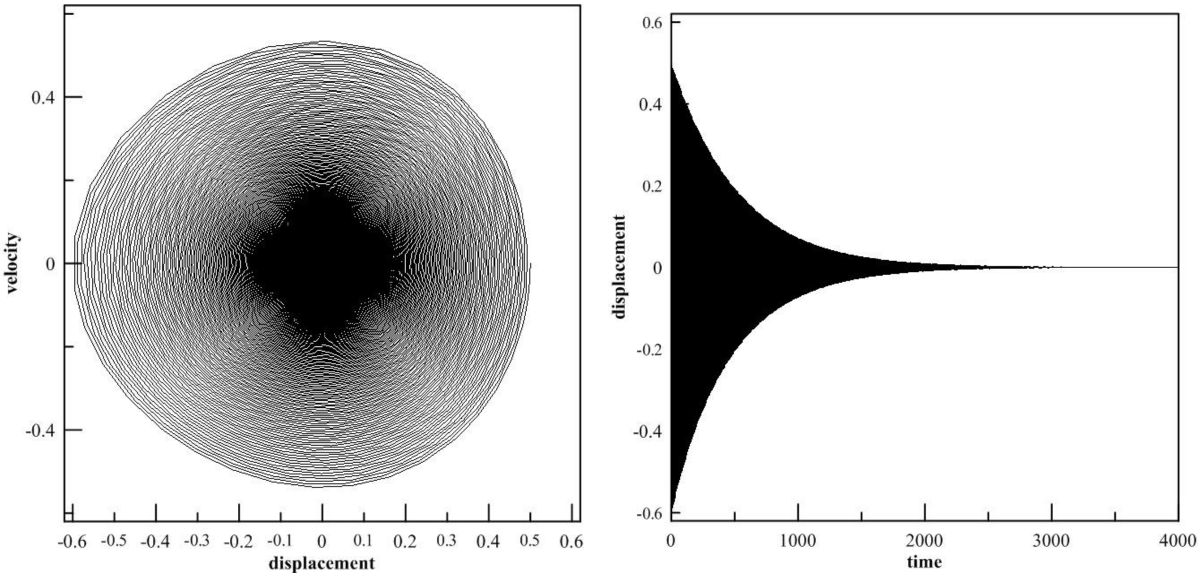

(a) (b)

Figure 4.18. (a) Phase plot and (b) time-displacement plot of vibrating rough surface with n = 2.0 for normalized initial displacement as 0.5.

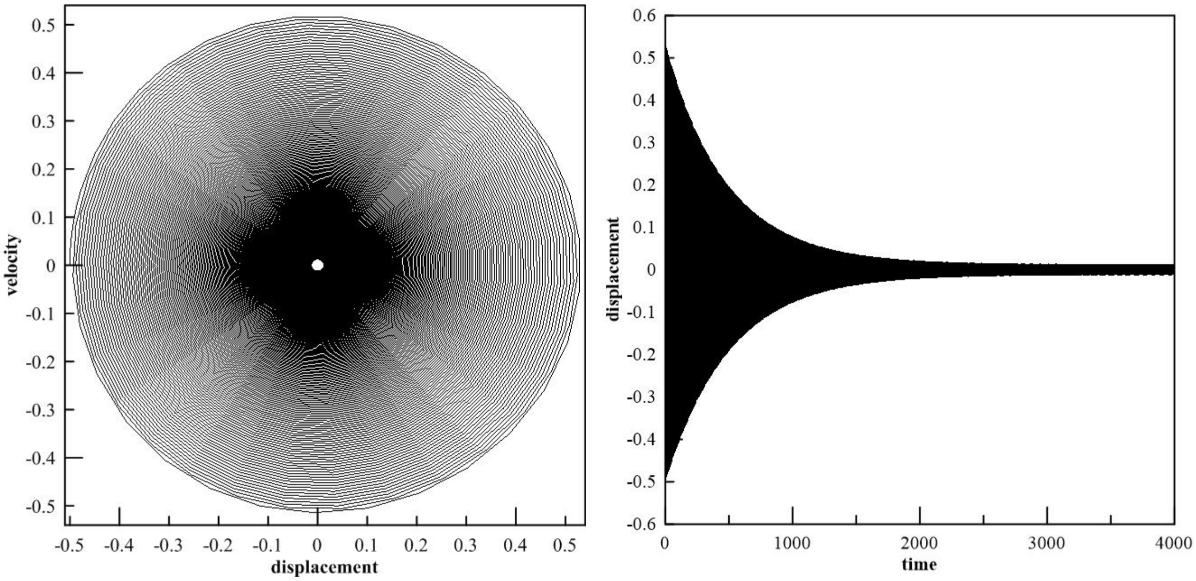

(a) (b)

Figure 4.19. (a) Phase plot and (b) time-displacement plot of vibrating rough surface with *n* = 0.6 for normalized initial displacement as -0.5.

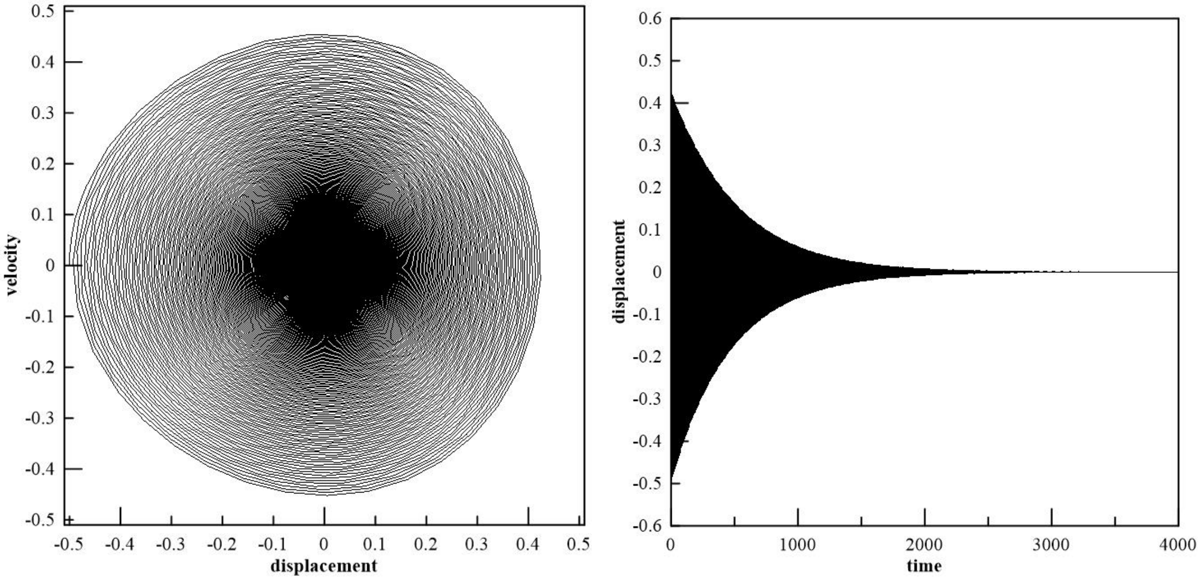

(a) (b)

Figure 4.20. (a) Phase plot and (b) time-displacement plot of vibrating rough surface with *n* = 2.0 for normalized initial displacement as -0.5.

Observing the phase plot and dime-displacement plots for a range of nonlinearity exponent values with both positive and negative initial displacement, it is seen that when nonlinearity increases (value of *n* shifts towards either sides of unity), the asymmetricity of the phase plot w.r.t the vertical axis $(u = 0)$ increases. As the value of the nonlinearity exponent (n) decreases from unity, the maximum displacement in the positive direction increases compared to the maximum displacement in the negative direction and the opposite happens when the value of the nonlinearity exponent increases from unity.

4.4. Summary

In the present chapter an analysis of the dynamic characteristics of rough deformable fractal surface influenced by a contacting harmonically excited rigid flat surface. The dynamic system is represented by a single degree of freedom spring-mass-damper system with harmonic excitation on the base the spring-mass-damper is resting on. The parameter nonlinearity exponent which is obtained from the force-displacement relationship of the deformable rough surface is used to determine the dynamic characteristics of the system. The effect of the variation of fractal parameters and the material properties are also analysed. It is observed that for higher nonlinearity the response amplitude decreases but above certain value of nonlinearity exponent the amplitude becomes constant. From phase plot and time-displacement plot it is noted that higher nonlinearity causes higher asymmetricity of the phase plot w.r.t. the vertical axis. As the value of the nonlinearity exponent decreases from unity, the maximum displacement in the positive direction increases compared to the maximum displacement in the negative direction and when the value of the nonlinearity exponent increases from unity, maximum negative displacement increases compared to the maximum positive displacement.

Chapter 5

Conclusions

This chapter provides the conclusion to the present thesis along with the future scope of work.

5.1. Conclusions

The main objective of the present research work is to analyze the dynamic characteristics of rough deformable fractal surface in contact with a rigid flat. In the present thesis, coordinate points constructing fractal surface are generated using the modified Weierstrass-Mandelbrot function in MATLAB. These points are imported to ANSYS as keypoints by defining array parameters to construct the finite element model of the rough fractal surface which comes in contact with a rigid flat surface. Downward motion of the rigid flat causes deformation of the rough surface. A Finite element analysis is implemented to obtain the force-displacement relationship. Fitting a power law curve through the obtained result points, nonlinear contact bulk stiffness and a parameter called 'nonlinearity exponent' (n) are found out which provides the measure of nonlinearity of the contact system. It has been observed that, the nonlinearity of the system increases with the increase of surface roughness, tangent modulus and with the decrease of yield strength.

In the present thesis, the physical dynamic contact system is modelled by single degree of freedom spring-mass-damper system. The external excitation on the dynamic system is imparted in two ways in the two models presented in the present thesis. The output parameters of the static force-displacement analysis are utilized as input parameters to the dynamic analysis of the surface for free-undamped as well as for forced-damped vibration. For free undamped vibration analysis, contact loss is taken into account and the variation of normalized natural frequency w.r.t. initial displacement is presented for different surface and material properties.

In case of forced damped vibration, the dynamic characteristics are presented in the form of frequency response curves. It is found out that for linearly elastic surface, the system is softening in nature and the softening nature increases with the increase of roughness of the surface. Similarly, the softening nature increases with increase in tangent modulus for elastic-plastic contact. While analyzing the effect of yield strength value of the rough surface material, it is found that above a certain value of yield strength the nature of the frequency response curve changes from softening to hardening in nature. In the second model, the contact system is represented by a spring-mass-damper system with base excitation. It is found that, for higher surface roughness, tangent modulus and lower yield strength value, the response amplitude decreases. For higher nonlinearity the response amplitude decreases but above certain value of nonlinearity exponent the peak amplitude becomes fixed. For both the models, forced vibration study reveals a few typical nonlinear characteristics with regards to the frequency response curves. Multiple response amplitudes corresponding to a single external excitation frequency has been observed for both hardening as well as softening nonlinearities. However, it should be mentioned that, the present method is unable to capture the unstable response. Jump up and jump down has also been observed while performing frequency sweeps. From phase plot and time-displacement plot it is noted that higher nonlinearity causes higher asymmetricity of the phase plot w.r.t. the vertical axis.

5.2 Future scope of work

In the present thesis, the dynamic analysis of contact between a rough deformable fractal surface and a rigid flat is carried out for the variation of surface roughness parameters and material properties. There are a number of avenues on which the research work could be extended, which are noted as bellow

- To incorporate adhesion as a factor influencing damping of the dynamic system and study the effect of adhesion on the overall dynamic characteristic of the system.
- Effect of the contact vibration parameters on wear and friction of the contacting surface.
- Dynamic analysis of contact surfaces constructed with layered materials.

Objective of a simulation study is to predict the system behaviour with accuracy on the basis of mathematical modelling. In the present scenario, the dynamic model is a basic SDOF spring-mass-damper system. So, there is a scope for inclusion of further complexities into the model. For example, in the present work linear damping model has been considered. But, in future nonlinear damping models can be incorporated for accurate prediction of output parameters.

References

1. Hertz, H., 1882. Über die Berührung fester elastischer Körper. *Journal für die reine und Angewandte Mathematik*, *92*, pp.156-171.

2. Hertz, H., 1882. Über die berührung fester elastische Körper und über die Harte. *Verhandlungen des Vereins zur Beförderung des Gewerbefleisses*.

3. Abbott, E. J. and Firestone, F. A., 1933. Specifying surface quality - a method based on accurate measurement and comparison, *Journal of Mechanical Engineering*, 55, pp. 569-572.

4. Greenwood, J.A. and Williamson, J.B.P., 1966, December. Contact of nominally flat surfaces. In *Proceedings of the Royal Society of London A: Mathematical, Physical and Engineering Sciences*, *295*(1442), pp. 300-319.

5. Greenwood, J.A. and Tripp, J.H., 1970. The contact of two nominally flat rough surfaces. *Proceedings of the Institution of Mechanical Engineers*, *185*(1), pp.625-633.

6. Akyuz, F.A. and Merwin, J.E., 1968. Solution of nonlinear problems of elastoplasticity by finite element method. *AIAA Journal*, *6*(10), pp.1825-1831.

7. Whitehouse, D.J. and Archard, J.F., 1970, March. The properties of random surfaces of significance in their contact. *Proceedings of the Royal Society of London A: Mathematical, Physical and Engineering Sciences*, *316* (1524), pp. 97-121.

8. Hardy, C.C.N.G.V., Baronet, C.N. and Tordion, G.V., 1971. The elasto-plastic indentation of a half-space by a rigid sphere. *International Journal for Numerical Methods in Engineering*, *3*(4), pp.451-462.

9. Dumas, G. and Baronet, C.N., 1971. Elastoplastic indentation of a half-space by an infinitely long rigid circular cylinder. *International Journal of Mechanical Sciences*, *13*(6), pp.519-530.

10. Lee, C.H., Masaki, S. and Kobayashi, S., 1972. Analysis of ball indentation. *International Journal of Mechanical Sciences*, *14*(7), pp.417-426.

11. Nayak, P.R., 1971. Random process model of rough surfaces. *Journal of Lubrication Technology*, *93*(3), pp.398-407.

12. Tallian, T.E., 1972. The theory of partial elastohydrodynamic contacts. *Wear*, *21*(1), pp.49-101.

13. Gupta, P.K. and Cook, N.H., 1972. Statistical analysis of mechanical interaction of rough surfaces. *Journal of Lubrication Technology*, *94*(1), pp.19-26.

14. Williamson, J.B.P. and Hunt, R.T., 1972, March. Asperity persistence and the real area of contact between rough surfaces. *Proceedings of the Royal Society of London A: Mathematical, Physical and Engineering Sciences*, *327*(1569), pp. 147-157.

15. Onions, R.A. and Archard, J.F., 1973. The contact of surfaces having a random structure. *Journal of Physics D: Applied Physics*, *6*(3), p.289.

16. Hisakado, T., 1974. Effect of surface roughness on contact between solid surfaces. *Wear*, *28*(2), pp.217-234.

17. Bush, A.W., Gibson, R.D. and Thomas, T.R., 1975. The elastic contact of a rough surface. *Wear*, *35*(1), pp.87-111.

18. O'Callaghan, M. and Cameron, M.A., 1976. Static contact under load between nominally flat surfaces in which deformation is purely elastic. *Wear*, *36*(1), pp.79-97.

19. Francis, B.A., 1977. The linear multivariable regulator problem. *SIAM Journal on Control and Optimization*, *15*(3), pp.486-505.

20. McCool, J.I., 1983. Limits of applicability of elastic contact models of rough surfaces. *Wear*, *86*(1), pp.105-118.

21. McCool, J.I., 1986. Comparison of models for the contact of rough surfaces. *Wear*, *107*(1), pp.37-60.

22. Greenwood, J.A., 1985. Formulas for moderately elliptical Hertzian contacts. *Journal of Tribology*, *107*(4), pp.501-504.

23. Johnson, K.L., 1987. *Contact Mechanics*. Cambridge University Press.

24. Boussinesq, J., 1885, *Application des Potentials á l'etude de l'équilibre et du mouvement des solides élastiques*, Gauthier-Villars, Paris.

25. Chang, W.R., Etsion, I. and Bogy, D.B., 1987. An elastic-plastic model for the contact of rough surfaces. *Journal of Tribology*, *109*(2), pp.257-263.

26. Kucharski, S., Klimczak, T., Polijaniuk, A. and Kaczmarek, J., 1994. Finite-elements model for the contact of rough surfaces. *Wear*, *177*(1), pp.1-13.

27. Ju, Y. and Farris, T.N., 1996. Spectral analysis of two-dimensional contact problems. *Journal of Tribology*, *118*(2), pp.320-328.

28. Zhao, Y., Maietta, D.M. and Chang, L., 2000. An asperity microcontact model incorporating the transition from elastic deformation to fully plastic flow. *Journal of Tribology*, *122*(1), pp.86-93.

29. Adams, G.G. and Nosonovsky, M., 2000. Contact modeling—forces. *Tribology International*, *33*(5), pp.431-442.

30. Zhao, Y. and Chang, L., 2001. A model of asperity interactions in elastic-plastic contact of rough surfaces. *Journal of Tribology*, *123*(4), pp.857-864.

31. Kogut, L. and Etsion, I., 2002. Elastic-plastic contact analysis of a sphere and a rigid flat. *Journal of Applied Mechanics*, *69*(5), pp.657-662.

32. Kogut, L. and Etsion, I., 2003. A finite element based elastic-plastic model for the contact of rough surfaces. *Tribology Transactions*, *46*(3), pp.383-390.

33. Jackson, R.L. and Green, I., 2005. A finite element study of elasto-plastic hemispherical contact against a rigid flat. *Journal of Tribology*, *127*(2), pp.343-354.

34. Bahrami, M., Yovanovich, M.M. and Culham, J.R., 2005. A compact model for spherical rough contacts. *Journal of Tribology*, *127*(4), pp.884-889.

35. Cai, S. and Bhushan, B., 2005. A numerical three-dimensional contact model for rough, multilayered elastic/plastic solid surfaces. *Wear*, *259*(7), pp.1408-1423.

36. Jackson, R.L. and Streator, J.L., 2006. A multi-scale model for contact between rough surfaces. *Wear*, *261*(11), pp.1337-1347.

37. Jamari, J. and Schipper, D.J., 2006. Experimental investigation of fully plastic contact of a sphere against a hard flat. *Journal of Tribology*, *128*(2), pp.230-235.

38. Kadin, Y., Kligerman, Y. and Etsion, I., 2006. Unloading an elastic–plastic contact of rough surfaces. *Journal of the Mechanics and Physics of Solids*, *54*(12), pp.2652-2674.

39. Greenwood, J.A., 2006. A simplified elliptic model of rough surface contact. *Wear*, *261*(2), pp.191-200.

40. Shankar, S. and Mayuram, M.M., 2008. A finite element based study on the elastic-plastic transition behavior in a hemisphere in contact with a rigid flat. *Journal of Tribology*, *130*(4), p.044502.

41. Ciavarella, M., Greenwood, J.A. and Paggi, M., 2008. Inclusion of “interaction” in the Greenwood and Williamson contact theory. *Wear, 265*(5), pp.729-734.

42. Sepehri, A. and Farhang, K., 2009. Closed-form equations for three dimensional elastic-plastic contact of nominally flat rough surfaces. *Journal of Tribology*, *131*(4), p.041402.

43. Sahoo, P., Chatterjee, B. and Adhikary, D., 2010. Finite element based Elastic-plastic contact behavior of a sphere against a rigid flat-Effect of Strain Hardening. *International Journal of Engineering and Technology*, *2*(1), pp.1-6.

44. Sahoo, P. and Chatterjee, B., 2010. A finite element study of elastic-plastic hemispherical contact behavior against a rigid flat under varying modulus of elasticity and sphere radius. *Engineering*, *2*(04), p.205.

45. Brake, M.R., 2012. An analytical elastic-perfectly plastic contact model. *International Journal of Solids and Structures*, *49*(22), pp.3129-3141.

46. Gandhi, V.C.S., Ramesh, S. and Kumaravelan, R., 2012. Analysis of Elastic-Plastic Contact Performance of Rigid Sphere Against a Deformable Flat-Effect of Strain Hardness. *American Journal of Applied Sciences*, *9*(2), p.240.

47. Peng, H., Liu, Z. and Zhang, G., 2013. A study of overall contact behavior of an elastic perfectly plastic hemisphere and a rigid plane. *Proceedings of the Institution of Mechanical Engineers, Part J: Journal of Engineering Tribology*, *227*(3), pp.259-274.

48. Peng, H., Liu, Z., Huang, F. and Ma, R., 2013. A study of elastic–plastic contact of statistical rough surfaces. *Proceedings of the Institution of Mechanical Engineers, Part J: Journal of Engineering Tribology*, *227*(10), pp.1076-1089.

49. Wang, L. and Xiang, Y., 2013. 3D Finite Element Analysis of a Single Asperity Tangential Elastic-plastic Deformation Characteristics. *Journal of Applied Sciences*, *13*, pp.4688-4694.

50. Megalingam, A. and Mayuram, M.M., 2014. Effect of surface parameters on finite element method based deterministic Gaussian rough surface contact model. *Proceedings of the Institution of Mechanical Engineers, Part J: Journal of Engineering Tribology*, *228*(12), pp.1358-1373.

51. Mandelbrot, B.B., 1967. How long is the coast of Britain. *Science, 156*(3775), pp.636-638.

52. Mandelbrot, B.B., 1975. Stochastic models for the Earth's relief, the shape and the fractal dimension of the coastlines, and the number-area rule for islands. *Proceedings of the National Academy of Sciences*, *72*(10), pp.3825-3828.

53. Mandelbrot, B.B., 1982. *The Fractal Geometry of Nature*, W.H. Freeman, New York.

54. Mandelbrot, B.B. and Blumen, A., 1989, May. Fractal Geometry: What is it, and What Does it do?[and Discussion]. *Proceedings of the Royal Society of London A: Mathematical, Physical and Engineering Sciences*, *423*(1864), pp. 3-16.

55. Berry, M.V. and Lewis, Z.V., 1980, April. On the Weierstrass-Mandelbrot fractal function. *Proceedings of the Royal Society of London A: Mathematical, Physical and Engineering Sciences*, *370*(1743), pp. 459-484.

56. Ausloos, M. and Berman, D.H., 1985, A multivariate Weierstrass-Mandelbrot function. *Proceedings of the Royal Society of London A: Mathematical, Physical and Engineering Sciences*, *400*(1819), pp. 331-350.

57. Ling, F.F., 1990. Fractals, engineering surfaces and tribology. *Wear*, *136*(1), pp.141-156.

58. Majumdar, A. and Tien, C.L., 1990. Fractal characterization and simulation of rough surfaces. *Wear*, *136*(2), pp.313-327.

59. Majumdar, A. and Bhushan, B., 1990. Role of fractal geometry in roughness characterization and contact mechanics of surfaces. *Journal of Tribology*, *112*(2), pp.205-216.

60. Majumdar, A. and Bhushan, B., 1991. Fractal model of elastic-plastic contact between rough surfaces. *Journal of Tribology*, *113*(1), pp.1-11.

61. Blackmore, D. and Zhou, J.G., 1998. Fractal analysis of height distributions of anisotropic rough surfaces. *Fractals*, *6*(1), pp.43-58.

62. Yan, W. and Komvopoulos, K., 1998. Contact analysis of elastic-plastic fractal surfaces. *Journal of Applied Physics*, *84*(7), pp.3617-3624.

63. Zahouani, H., Vargiolu, R. and Loubet, J.L., 1998. Fractal models of surface topography and contact mechanics. *Mathematical and Computer Modelling*, *28*(4), pp.517-534.

64. Komvopoulos, K. and Ye, N., 2001. Three-dimensional contact analysis of elastic-plastic layered media with fractal surface topographies. *Journal of Tribology*, *123*(3), pp.632-640.

65. Palasantzas, G. and De Hosson, J.T.M., 2003. Self-affine roughness effects on the contact area between elastic bodies. *Journal of Applied Physics*, *93*(2), pp.898-902.

66. Willner, K., 2004. Elasto-plastic normal contact of three-dimensional fractal surfaces using halfspace theory. *Journal of Tribology*, *126*(1), pp.28-33.

67. Chung, J.C. and Lin, J.F., 2006. Variation in fractal properties and non-Gaussian distributions of microcontact between elastic-plastic rough surfaces with mean surface separation. *Journal of Applied Mechanics*, *73*(1), pp.143-152.

68. Kogut, L. and Jackson, R.L., 2006. A comparison of contact modeling utilizing statistical and fractal approaches. *Journal of Tribology*, *128*(1), pp.213-217.

69. Liou, J.L. and Lin, J.F., 2006. A new method developed for fractal dimension and topothesy varying with the mean separation of two contact surfaces. *Journal of Tribology*, *128*(3), pp.515-524.

70. Sahoo, P. and Ghosh, N., 2007. Finite element contact analysis of fractal surfaces. *Journal of Physics D: Applied Physics*, *40*(14), p.4245.

71. Jiang, S., Zheng, Y. and Zhu, H., 2010. A contact stiffness model of machined plane joint based on fractal theory. *Journal of Tribology*, *132*(1), p.011401.

72. Pohrt, R. and Popov, V.L., 2012. Investigation of the dry normal contact between fractal rough surfaces using the reduction method, comparison to 3D simulations. *Physical Mesomechanics*, *15*(4), pp.31-35.

73. Pohrt, R. and Popov, V.L., 2012. Normal contact stiffness of elastic solids with fractal rough surfaces. *Physical Review Letters*, *108*(10), p.104301.

74. Pohrt, R., Popov, V.L. and Filippov, A.E., 2012. Normal contact stiffness of elastic solids with fractal rough surfaces for one-and three-dimensional systems. *Physical Review E*, *86*(2), p.026710.

75. Chatterjee, B. and Sahoo, P., 2013. Finite element based parametric study of elastic-plastic contact of fractal surfaces. *Procedia Engineering*, *64*, pp.552-561.

76. Miao, X. and Huang, X., 2014. A complete contact model of a fractal rough surface. *Wear*, *309*(1), pp.146-151.

77. Chatterjee, B. and Sahoo, P., 2014. Finite Element Based Contact Analysis of Fractal Surfaces–Effect of Varying Elastic Modulus. *Procedia Engineering*, *90*, pp.116-122.

78. Buczkowski, R., Kleiber, M. and Starzynski, G., 2014. Normal contact stiffness of fractal rough surfaces. *Archives of Mechanics*, *66*(6), pp.411-428.

79. Nayak, P.R., 1972. Contact vibrations. *Journal of Sound and Vibration, 22*(3), pp.297-322.

80. Hess, D.P. and Soom, A., 1991. Normal vibrations and friction under harmonic loads: part I—Hertzian contacts. *Journal of Tribology, 113*(1), pp.80-86.

81. Hess, D.P. and Soom, A., 1991. Normal vibrations and friction under harmonic loads: part II—rough planar contacts. *Journal of Tribology, 113*(1), pp.87-92.

82. Nayfeh, A.H. and Mook, D.T., 2008. *Nonlinear Oscillations*. John Wiley & Sons.

83. Perret-Liaudet, J., 1997. Subharmonic resonance of order 2 on a sphere-plane contact. *Comptes Rendus de l'Academie des Sciences Series IIB Mechanics Physics Chemistry Astronomy, 8*(325), pp.443-448.

84. Perret-Liaudet, J., 1998. Superharmonic resonance of order two on a sphere-plane contact. *Comptes Rendus de l'Academie des Sciences Series IIB Mechanics Physics Astronomy, 12*(326), pp.787-792.

85. Sabot, J., Krempf, P. and Janolin, C., 1998. Non-linear vibrations of a sphere–plane contact excited by a normal load. *Journal of Sound and Vibration*, *214*(2), pp.359-375.

86. Perret-Liaudet, J. and Sabot, J., 1999. Vibro-impacts induced by non-linear resonances in hertzian contacts. In *Dynamics of Vibro-impact Systems*, Springer Berlin Heidelberg pp.251-260.

87. Rigaud, E. and Perret-Liaudet, J., 2003. Experiments and numerical results on non-linear vibrations of an impacting Hertzian contact. Part 1: harmonic excitation. *Journal of Sound and Vibration, 265*(2), pp.289-307.

88. Perret-Liaudet, J. and Rigaud, E., 2003. Experiments and numerical results on non-linear vibrations of an impacting Hertzian contact. Part 2: random excitation. *Journal of Sound and Vibration, 265*(2), pp.309-327.

89. Perret-Liaudet, J. and Rigaud, E., 2006. Response of an impacting Hertzian contact to an order-2 subharmonic excitation: Theory and experiments. *Journal of Sound and Vibration*, *296*(1), pp.319-333.

90. Perret-Liaudet, J. and Rigaud, E., 2007. Superharmonic resonance of order 2 for an impacting Hertzian contact oscillator: Theory and experiments. *Journal of Computational and Nonlinear Dynamics, 2*(2), pp.190-196.

91. Ma, Q.L., Kahraman, A., Perret-Liaudet, J. and Rigaud, E., 2007. An investigation of steady-state dynamic response of a sphere-plane contact interface with contact loss. *Journal of Applied Mechanics*, *74*(2), pp.249-255.

92. Tian, J. and Xie, Z., 2008. Dynamic contact stiffness of vibrating rigid sphere contacting semi-infinite transversely isotropic viscoelastic solid. *Acta Mechanica Solida Sinica*, *21*(6), pp.580-588.

93. Xiao, H., Brennan, M.J. and Shao, Y., 2011. On the undamped free vibration of a mass interacting with a Hertzian contact stiffness. *Mechanics Research Communications*, *38*(8), pp.560-564.

94. Zili, Xu, Yang Yi, and Zhang Chunmei, 2013. Modeling Contact Interface Between Rough Surfaces Based On Fractal Contact Model And Thin Layer Elements. *International Congress of Sound and Vibration*.

95. Xiao, H., Shao, Y. and Brennan, M.J., 2015. On the contact stiffness and nonlinear vibration of an elastic body with a rough surface in contact with a rigid flat surface. *European Journal of Mechanics-A/Solids*, *49*, pp.321-328.

96. Zhong, Z.H., 1993. *Finite element procedures for contact-impact problems*. Oxford University Press.

97. Buzio, R., Boragno, C. and Valbusa, U., 2003. Contact mechanics and friction of fractal surfaces probed by atomic force microscopy. *Wear*, *254*(9), pp.917-923.

98. ANSYS 14.5 Help, Element Library.

99. Johnson, K. L., 1968, An Experimental Determination of the Contact Stresses Between Plastically Deformed Cylinders and Spheres, *Engineering Plasticity*, Cambridge University Press, Cambridge, pp. 341–361

100. W.H., Teukolsky, S.A., Vetterling, W.T. and Flannery, B.P., 1996.*Numerical recipes in C* (Vol. 2). Cambridge University Press, Cambridge.

101. Kimura, T., 2009. *On Dormand-Prince Method*.

102. Mathews, J.H. and Fink, K.D., 1999. *Numerical methods using MATLAB*, Upper Saddle River, NJ: Prentice Hall.

103. Gil, A., Segura, J. and Temme, N.M., 2007. *Numerical methods for special functions*. Siam.